<u>İSTANBUL TECHNICAL UNIVERSITY ★ INSTITUTE OF SCIENCE AND TECHNOLOGY</u>

MODELLING AND ANALYSIS OF ROTOR-BALL BEARING SYSTEMS

M. Sc. Thesis by
Onur ÇAKMAK

Department: Mechanical Engineering

Programme: Machine Dynamics, Vibration&Acoustics

JUNE 2010

<u>İSTANBUL TECHNICAL UNIVERSITY ★ INSTITUTE OF SCIENCE AND TECHNOLOGY</u>

MODELLING AND ANALYSIS OF ROTOR-BALL BEARING SYSTEMS

M. Sc. Thesis by

Onur ÇAKMAK

(503071409)

Date of submission : 07 May 2010

Date of defence examination: 09 June 2010

Supervisor (Chairman) : Prof. Dr. Kenan Yüce ŞANLITÜRK

Members of the Examining Committee : Prof. Dr. Vahit MERMERTAŞ

Prof. Dr. Zahit MECİTOĞLU

JUNE 2010

İSTANBUL TEKNİK ÜNİVERSİTESİ ★ FEN BİLİMLERİ ENSTİTÜSÜ

RULMANLI-ROTOR SİSTEMLERİNİN MODELLENMESİ VE ANALİZİ

YÜKSEK LİSANS TEZİ

Onur ÇAKMAK

(503071409)

Tezin Enstitüye Verildiği Tarih : 07 Mayıs 2010

Tezin Savunulduğu Tarih : 09 Haziran 2010

Tez Danışmanı : Prof. Dr. Kenan Yüce ŞANLITÜRK

Diğer Jüri Üyeleri: Prof. Dr. Vahit MERMERTAŞ

Prof. Dr. Zahit MECİTOĞLU

HAZİRAN 2010

FOREWORD

I would like to thank to dear Prof. Dr. Kenan Yuce Sanliturk, who is the supervisor of this project very much for his leading ideas, helpful advices and suggestions about the thesis.

I would like to thank to Mr. Metin Gül, Leader of vibrtation and acoustics technology family at R&D Department of ARÇELİK A.Ş., because of his helps about funding the project and Mr Ahmet Ali Uslu for his advices and helps and my work friends Mr. Mete Oğüç, Mr. Onur Yenigül, Mr. Cihan Orhan and Mr. Resul Şahin and Mr İsak Varol for their support during the project.

I would like to thank to my dear FAMILY my FRIENDS because of their infinite support during this project and my life.

May 2010

Onur ÇAKMAK

Mechanical Engineer

TABLE OF CONTENTS

ABBREVATIONS

AC **:** Alternative Current
BEAT **:** BEAring Toolbox
BPF **:** Ball Passing Frequency
BPFI **:** Ball Passing Frequency Inner ring
BPFO **:** Ball Passing Frequency Outer ring
BSFESS **:** Ball Spin Frequency
CMS **:** Component Mode Synthesis
DOF **:** Degree Of Freedom
EHD **:** ElastoHydroDynamic
FD **:** Frequency Dependent
FE **:** Finite Elements
FFT **:** Fast Fourier Transform
FRF **:** Frequency Response Function
MBS **:** MultiBody System
MIMO **:** Multi Input Multi Output
RKCK **:** Runge-Kutta Cash-Kord
SWAT : Soil and Water Assessment Tool
RPM **:** Revolution Per Minute
SIMO **:** Single Input Multi Output
STFT **:** Short Time Fourier Transform

LIST OF TABLES

LIST OF FIGURES

LIST OF SYMBOLS

D	: Outer diameter
d_i	: Bore diameter
d_m	: Pitch diameter
R_{in}	: Inner raceway radius
R_{out}	: Outer raceway radius
R_i	: Inner groove radius
R_o	: Outer groove radius
d	: Ball diameter
C_d	: Diametral clearance
R_{re}	: Ball radius
α	: Contact angle
k_e	: Ellipticity parameter
a_e	: Semi-minor axes of ellipse geometry
b_e	: Semi-major axes of ellipse geometry
R_d	: Curvature difference
ξ	: Elliptic integral of the first type
ζ	: Elliptic integral of the second type
Kc	: Contact stiffness
E	: Modulus of elasticity
υ	: Poisson ratio
Rr	: Race conformity
fi	: Inner ring osculation
fo	: Outer ring osculation

ω	: Angular velocity in terms of rad/s
n	: Angular velocity in terms of rpm
N_b	: Number of balls
F:	: Force
M	: Moment
y	: Deflection of the shaft
θ	: Slope of the shaft
kii:	: Stiffness of ith element in the matrix
ωn	: Natural frequency
I_p	: Polar moment of inertia
I_d	: Rotor moment of inertia about the axis perpendicular to rotation axis
ψ	: Total slope of the shaft
m	: Mass of the disc

MODELLING AND ANALYSIS OF ROTOR-BALL BEARING SYSTEMS

SUMMARY

Ball bearings are the one of the most common components in many mechanical engineering applications. Also, for the purposes of condition monitoring, fault diagnostics and system maintenance of a rotating machinery, vibration generation and transmission through rolling element, bearing is a very important and interesting subject to study. It is known that ball bearings have very significant role on the global vibrations of a rotating machinery. The aim of this study is improving a new rotor-ball bearing model in order to investigate the effects of rotor-ball bearing systems on the global vibrations of a machine espacially. The commercial softwares used during this study are Msc. ADAMS, I-DEAS, Matlab and ICATS in numerical and experimental procedures.

In this study there is a literature survey about modelling the ball-bearing systems and methods are investigated. The theoretical background of the study is introduced at the theory section in order to understand the analytical manner behind the numerical and experimental procedures. The steps of building a ball bearing model in Msc ADAMS is mentioned and the procedure of assembling it with the rotor part is also described. A test rig is designed in order to validate the numerical model. Experimental modal analyses and order tracking analyses are performed during the experimantal validation process. The model is validated for further analysis.

It is shown that the model developed in this study is capable of representing the dynamic characteristics of rotor-ball bearing systems in an acceptable frequency range. The resonance characteristics of the rotor-ball bearing system are well-suited with the experimental results and the change of modal characteristics of the system proportinal to running speed is modelled succesfully.

RULMANLI-ROTOR SİSTEMLERİNİN MODELLENMESİ VE ANALİZİ

ÖZET

Bilyalı rulmanlar birçok mekanik uygulamada kullanılan çok önemli parçalardandır. Ayrıca bilyalı rulmanlar tarafından üretilen ve aktarılan titreşimlerin incelenmesi özellikle kestirimci bakım ve hata tespiti gibi konular için de önemli olduğundan çalışmaya değer bir konudur. Dönen makinaların toplam titreşimleri üzerinde rulmanların önemli etkilerinin olduğu bilinmetedir. Bu çalışmanın amacı; yeni bir rulmanlı-rotor modeli oluşturmak ve bu sayede bu yapıların bir makinan toplam titreşimleri üzerine etkilerini incelemektir. Çalışma sırasında Msc. ADAMS, I-DEAS, Matlab ve ICATS ticari yazılımlarından sayısal ve deneysel aşamalarda faydalanılmıştır.

Bu çalışmada konu ile ilgili literatür araşturılmış ve kullanılan metotlar incelenmiştir.Teorik altyapı aktarılmış ve böylce sayısal ve deneysel analizlerin analitik altyapısı ortaya konulmuştur. Bilyalı rulman modelinin ADAMS ortamında nasıl oluşturulduğu adım adım anlatılmış ve rulmanlı-rotor yapısının nasıl oluşturulduğundan bahsedilmiştir. Kurulan modeli doğrulamak amacıyla test düzeneği tasarlanmıştır Deneysel modal analizler ve order tracking analizleri bu süreçte kullanılmıştır. Model ileriki çalışmaları ışık tutması amacıyla doğrulanmıştır.

Kurulan modelin rulmanlı-rotor sistemlerinin dinamik özelliklerini kritik olan bir frekans aralığı için yansıtabildiği gösterilmiştir. Değişik hızalra göre değişen rezonanas karakterleri de çalışmada başarıyla incelenmiştir.

1. INTRODUCTION

Increasing noise levels with industrialization has adverse effects on human healths. Structural vibrations are one of the main causes of the product noise. Vibrations of different products have come into question due to legal restrictions and comfort expectations of customers. The dynamics of rotor-bearing systems are being investigated for several years in order to understand the sources of rotating machinery vibrations and reduce them to acceptable levels.

Ball bearings are the most common components in many mechanical engineering applications. Also, for the purposes of condition monitoring, fault diagnostics and system maintenance of a rotating machinery, vibration generation and transmission through rolling element, bearing is a very important and interesting subject to study. It is known that ball bearings have very significant role on the global vibrations of a rotating machinery. The studies about ball bearing vibrations are generally focused on fault detection and predictive maintanance. However, when they are coupled with the rotor and shaft structures; bearings without any defect can also cause excessive vibrations due to the resonance characteristics. Parameters dependent on rotor (imbalance, shaft geometry), bearing geometry (internal clearance, preload) should be taken into account when the dynamics of a rotor-ball bearing system is to be studied.

1.1. Problem

Vibrations of washing machines cause these machines to generate unacceptable noise. There are models of washing machines that are created with ADAMS commercial software, however dynamics of the bearings that hold washing machine drum are not modelled and analyzed with computer aided engineering methods. The position of the ball bearings and other important parts are shown in Figure 1.1. Also the effects of them when they are combined with rotor structures are not modelled in the company that supported this study. This problem inhibits the further understanding of the washing machine vibrations. Also the constructive changes have to be prototyped in order to investigate their effects on global vibrations. This situation causes a significant increase in prototyping costs. Modelling and analysis of rotor-ball bearing systems is critical for these reasons.

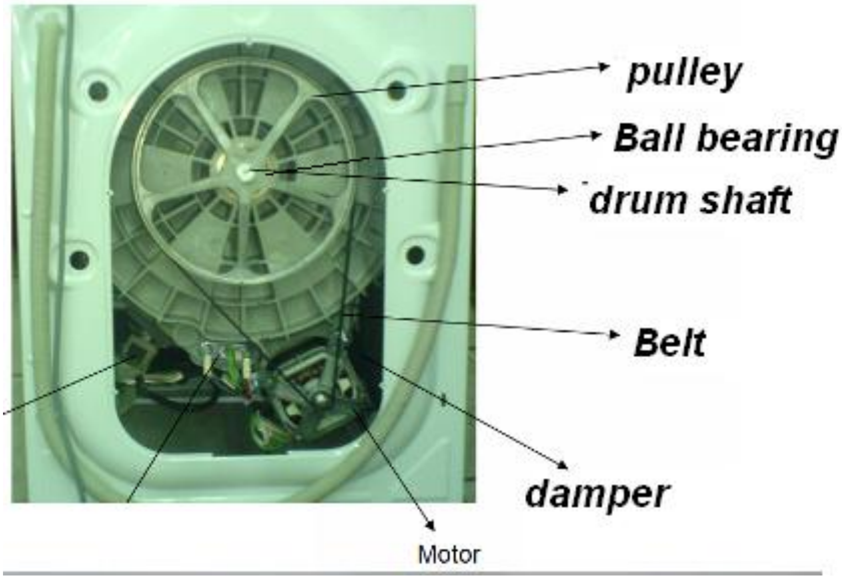

Figure 1.1 : The important parts of a washing machine

1.2. Purpose of the Thesis

In order to reduce the prototyping costs and analyze the vibrations of the rotor-ball bearing systems, validated models of them are necessary. The general purpose of this thesis is modelling and analyzing the dynamic characteristics of rotor-ball bearing systems. During this process, the ability of using commercial softwares while building this kind of numerical models will be improved.

During the thesis study for the numerical modelling processes, I-DEAS commercial software is used for building finite element models Msc. ADAMS software is used for building multibody system models and vibration analyses, also for dynamic simulations. MATLAB is used during the post-processing of the signals and plotting. Pulse platform is used during the measurements. And ICATS is used during the experimental modal analyses.

In the first chapter of the thesis a general introduction is made and purpose of the study is described. Second chapter is consisting of literature survey about the topic. The numerical, theoretical and experimental studies existing in the literature are summarized. The methods for analyzing the rotor-ball bearing vibrations are described. Also assumptions used in those studies are discussed.

In chapter 3, the theoretical background of the study is summarized. The dynamical properties of ball bearings and rotor-ball bearing systems are described briefly. Also the theory behind the experimental procedure is defined.

In chapter 4, the steps of numerical modelling process are described in details. The finite elements (FE) models of the ball bearing components and the results of numerical modal analyses of them are shown. Then the steps of building the ADAMS model of the ball bearing are described. Afterwards the model of the rotor part is introduced. Different types of rotor-bearing models with primitive joints are introduced and their comparison with the newly modelled ball bearing is shown. The assembled model of the rotor-ball bearing model is introduced finally with some deficiencies which will be completed after the experimental process.

In chapter 5, the designed test rig is introduced; the response of the test rig is shown in the light of experimental modal analyses. Also in order to improve the numerical model the stiffness properties of the flexible housings are investigated with experimental methods. Finally the dynamic behaviour of the test rig under different running conditions is investigated with experimental methods. Order tracking analyses are used during this process.

In chapter 6, the data obtained from the measurements are assessed and the numerical model is improved in the light of this experimental information. The validated model is subjected to modal analyses and the modal results obtained from both experimental and numerical models are compared in terms of natural frequencies and mode shapes. After the model is validated for the non-rotating case, the dynamic simulations are performed. The simulation results are processed with Short Time Fourier Transform (STFT) technique. Campbell diagrams obtained form both the numerical and the experimental models are compared for different unbalance and defect conditions.

In chapter 7, assessment of the study and suggestions for further studies are introduced.

2. LITERATURE SURVEY

2.1. Modeling of Rotor- Rolling Bearing Systems

In the literature, there are analytical, numerical and experimental studies about rolling bearing vibrations and their effects on rotor-bearing systems. Most of these studies are about various kinds of defects and their effects on vibration (Sassi, Tandon). The effects of the number of balls, preload, radial clearance are also discussed (Aktürk, Gupta). There are also studies including experimental validation of dynamic models of rotor-bearing systems built by Multi-Body System and Component Mode Synthesis approaches. (Wensing, Soppanen) The effects of rotor parameters (unbalance, etc.) on total vibration of the system are investigated by several authors. (Tiwari-Gupta). There are also books that summarize the assumption about rotor-bearing systems and their effects on the system's dynamic behaviour. (Goodwin)

2.1.1. Theoretical models for rotor-ball bearing systems

2.1.1.1. The Effects of Localized and Distributed Defects of Bearings

Bearing without any imperfection can generate vibration because of varying compliance or time-varying contact forces between components of the rolling bearing.

From condition monitoring point of view, the problem is generally about defects which are classified as distributed and localized. Surface roughness, waviness, misaligned races and off-size rolling elements are some examples of distributed defects. Cracks, pits and spalls due to fatigue on rolling surfaces are rated among the localized defects [1]. Tandon and Choudry [1], in 1997, studied on the vibration response of rolling element bearings due to a localized defect in an analytical manner. They assumed that the bearing rings are isolated continuous systems and then obtained the equations of motion by using Lagrange's equations. The localized defects are assumed as pulse generators and these pulses are mentioned as generalized forces in the equations of motion. The characteristic and the shape of the defect such as rectangle, triangle and half-sine are also taken into account. This mathematical model gives an opportunity to predict the frequencies and the vibration showed that the amplitude of vibration for the outer ring defect is higher than the inner ring and the rolling elements. The level of vibration amplitude is increasing in the case of higher load appliance. As a result, it is shown that, in the case of both axial and radial loads, defect on the outer race causes vibrations at the outer race defect frequency and its multiples. With the radial load consideration there are sidebands at defect frequencies, which means having peaks at the defect frequency and its harmonics with sidebands that are integer multiples of shaft frequency. On the other hand this model is not capable of predicting the peaks at the shaft rotational frequency and its harmonics when there is a defect on the inner race.

Sassi et al. [2] investigated the damaged bearing vibration phenomena in a numerical manner. Just like Tandon et al. they used the impact assumption for defect dynamics. In addition, the stiffness and damping of the lubricant fluid film has been taken into consideration (Figure 2.1). In this model developed, first the natural frequencies of the outer and inner rings are obtained by Finite Element Method (FEM) and the stiffness values of those components are determined by making use of the calculated natural frequencies and the known mass of the rings. The damping and stiffness of the lubricant film are also computed by using the Elasto-HydroDynamic EHD theory.

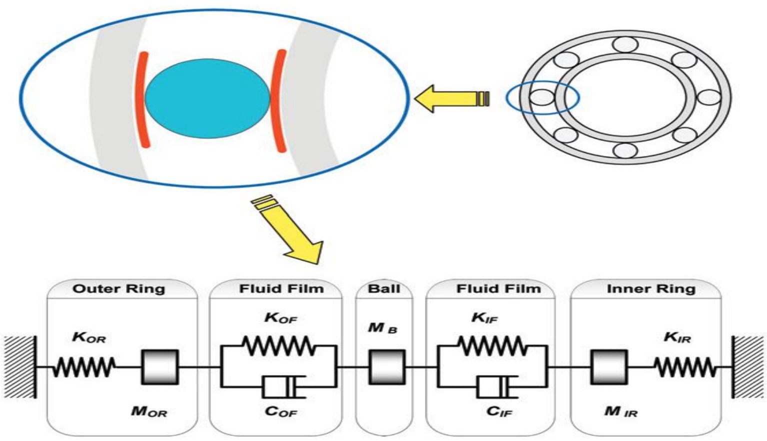

Figure 2.1 : Ball bearing contact model [2]

Tandon et al. [3] also studied the vibrations of ball bearings with distributed defects. First the vibration response of a bearing without any defect has been obtained. The amplitude of the vibration at cage frequency and its harmonics could then be determined by using a Fourier series expansion. The distributed defects investigated here are the sinusoidal defects of the bearing components (rings and rolling elements). Finally Tandon et al. compared the defected and ideal models. Their results show that for the model, outer and inner races have a response having a spectrum with peaks at characteristic defect frequencies for respective races. Those peaks have sidebands at shaft frequency and its multiples. It is claimed that the predicted amplitudes of the responses are not very close to the measurements on a mounted bearing. However, the predicted peak frequencies and the ratios among various spectral lines are in agreement with the measured behavior.

2.1.1.2. The effects of clearance, rotor unbalance, preload and ball size

Tiwari et al. [4] studied the effect of radial clearance on vibration response of a balanced rotor. They created a model based on several assumptions listed below:

The outer ring and the support, and the inner ring and the shaft are assumed to be connected to each other with fixed joints

The spaces between the balls are equal.

Balls are not slipping.

With these assumptions they found the varying compliance frequencies which are also named as Ball Passage Frequency in the literature. They used an SKF 6002 ball bearing for the simulation. The differential equations are obtained with an assumption of linearized stiffness [5]. The equation is solved using Cash-Kord Runge-Kutta (RKCK) method. For different shaft speeds the ball bearing characteristics change and according to Tiwari et al. [4]. Those regions that the ball bearing characteristics change can be named as regions with different regimes. Based on their theoretical simulations they concluded that:

Unstable and chaotic region becomes wider with the increase of radial clearance.

A shift down at peak frequencies is occurred due to the increase in clearance. This increase means a decrease in the dynamic stiffness.

Linear characteristics of the system increase significantly as the clearance decay and constant radial force increase. The subharmonics or chaos disappear, the unstable region gets smaller. Also due to the non-linear behavior of force deformation relationship, the load increment provides higher stiffness.

Subharmonic frequencies and the sum and difference combinations of rotational and varying compliance frequencies occur due to the non-linearity of the system,

By increasing damping vibration amplitudes and instability can be reduced.

In reference [6], Tiwari et al. improved the model at reference [4] for the case of unbalance. After performing similar simulations, it is shown that a response in chaos or instability region is occurred due to the unbalance force. Also the increase in clearance causes an increase in strength of superharmonics and backward whirl components.

Aktürk et al. [7] studied the effects of balls and preload on bearing vibrations. For a system with no defects, a theoretical investigation was made in order to determine whether the amount of preload and the change in number of balls can reduce the vibrations at the Ball Passing Frequency. The stiffness is determined via the Hertzian contact approach. The contact angle related to load is calculated from the geometric dimensions and deflections. The equations of motion are obtained under the following simplifying assumptions:

- There are three degrees of freedom including system radial translation in the *x* and *y*, axial translation in the *z* direction.
- Rolling elements are massless.
- Components are rigid and the contact stresses cause only local deformations.
- Hertzian Theory of elasticity is assumed for the determination of contact behaviour
- Damping generated from the elastohydrodynamic film, or from any friction at the various contacts, is neglected.
- The cage has constant angular velocity.
- There is no phase difference between the balls of bearings at both sides of the shaft.

The Runga-Kutta iterative method has been used again in order to obtain the solution. The model is applied to a system with an angular contact ball bearing. The results of this simulation are shown in Figure 2.2 To see the effect of number of balls, the preload is fixed to a very low value, so that the effect of the preload could be negligible. According to the further investigations they carried out, the Ball

Passage Vibrations are found to be significant and detectable when there is a discontinuity at the contact between the races.

In Figure 2.2 the most significant peaks are the natural frequencies coinciding with the frequency related to ball passing. This will be called Ball Passing Frequency (BPF) and it will be detaily identified in chapter 3. An increase in the ball number causes an increase in the natural frequency and BPF. On the other hand the increase of natural frequency is very small compared to the increase at BPF. This results in earlier coincidences of BPF and natural frequency during a run-up procedure. For example, the bearing with 5 balls, meets with the natural frequency (445 Hz) at 12700 Rpm shaft speed, whereas the one with 8 balls meet 510 Hz at 9700 Rpm. When there is further increase of ball number, the amplitudes of this peak decreases due to the stiffness rise. Also subharmonics of BPF have greater amplitudes contrary to superharmonics. Figure 2.2 b shows that due to the changing preload, contact angle changes and this causes a change in the BPF. For larger preloads the vibrations caused by BPF will be lower. In conclusion, number of balls and preload are critical parameters that affect BPF and should be considered when modeling a bearing and designing a machine.

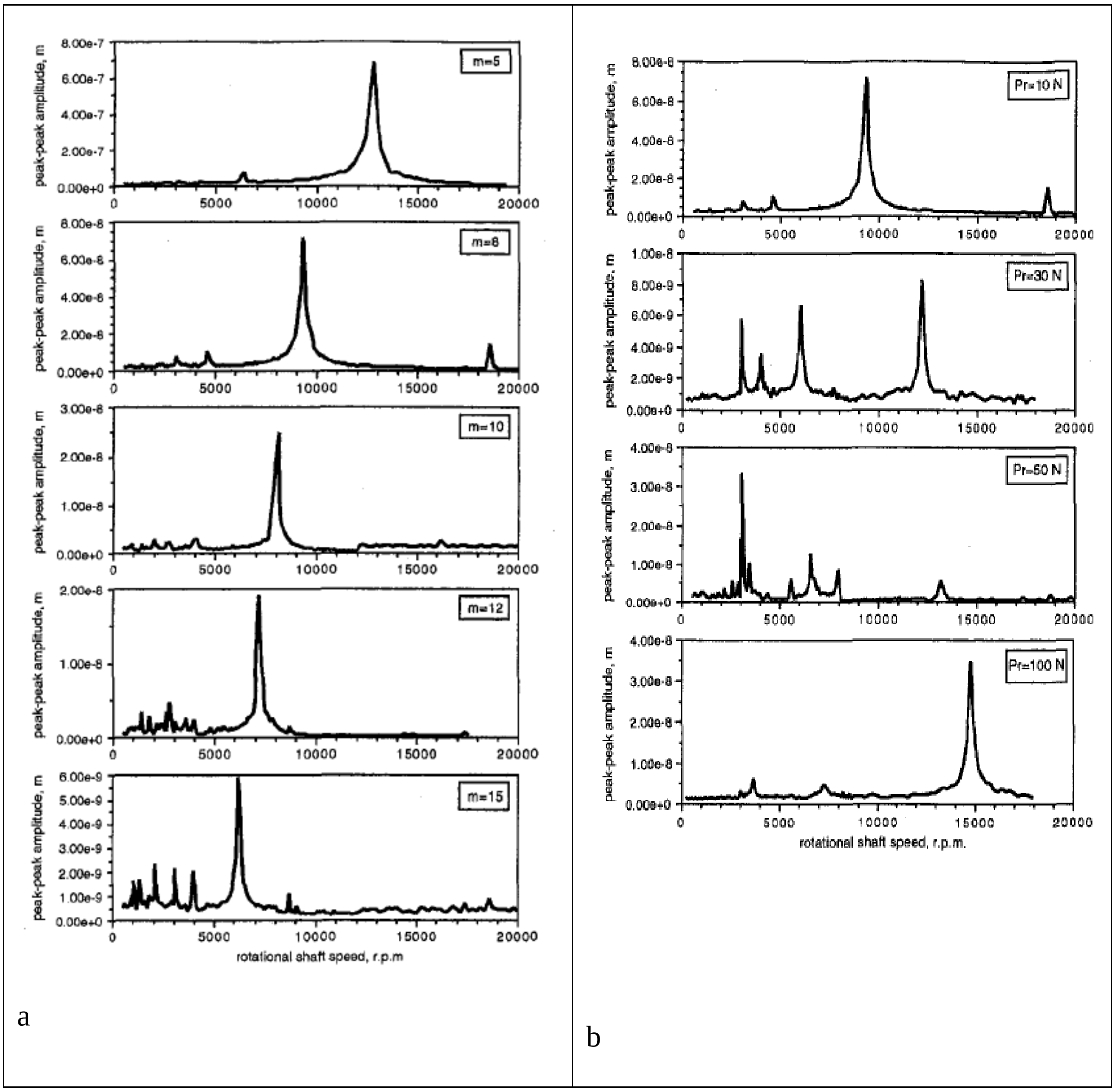

Figure 2.2 : Frequency response showing the effect of varying a) Number of balls (preload=10N) b) Preload (Number of balls=8)

2.1.2. Dynamic Models of Rotor-Bearing Systems With Computational Methods

In the literature, computer aided simulating is also used for developing bearing models. Some of the studies [2] are about toolboxes created on the environments of MATLAB or Mathematica. The BEAT toolbox [2] is generated for simulating the dynamics of defected bearings. On the other hand, Wensing [8] has built a ball bearing model by using Component Mode Synthesis (CMS) method. That study also contains the experimental validation of the model. Sopanen et al. [9, 10, 11] built a model with the help of Multi-Body System approach using MSC. ADAMS.

Wensing [8]; built a model in order to search for answers to the following questions:

- What is the ratio of the *vibrations generated inside the bearing due to geometrical imperfections* among the overall noise and vibration of the application?
- How is the dynamic behavior of an application effected from *bearing design*?
- What is the effect of *bearing mounting* on the application's vibration behavior?
- Does *standard vibration test* have a significant value, while predicting the vibration behavior of the application?

In this study, the effect of the lubricant film is not neglected. The stiffness values at the contacts are determined by Hertzian Theory, than the stiffness and damping caused by the lubricant film is added to the model. (Figure 2.3)

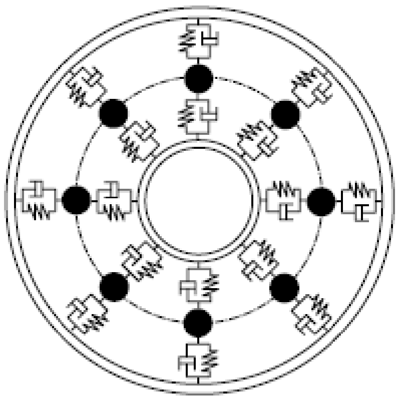

Figure 2.3: The lubricated contacts in a ball bearing are modeled with the EHL contact model. [8]

2.1.2.1. Component Mode Synthesis (CMS) Technique

In order to have higher efficiency at the design process, engineers divide mechanical systems into substructures and components. The components of a bearing model are often having well-defined connections with each other. The connection model presented in Figure 2.3 can be good example for this. A model based on component-wise approach can have some advantages since:

- Forming criteria for the dynamic behavior of each component supplied by subcontractors is easier.
- The modifications about design can be evaluated more efficiently at component level.

- There is an opportunity to leave modeling and analysis of components to subcontractors.
- The modeling of identical components is done only once.
- To test all the structure may not be feasible compared to testing the components individually.
- When modeling large systems which contain both linear and non-linear components, grouping the components having similar behaviors is more efficient.

Defining the dynamic motion of the system by a *global shape functions* series is called the Ritz method. To obtain the smallest set of those shape functions or component modes describing the dynamic behavior with satisfactory accuracy is the challenge of CMS methods. Wensing developed a new CMS method in order to reduce the sizes of FEM models of linear components. Otherwise, for time dependent analysis, it was not possible or feasible to solve the problem. Also, the known CMS methods were not capable of modeling structures under moving and rotating loads, since in the earlier methods it was assumed that the interface was fixed. At the new CMS method the moving interface loads can be applied to an interface surface. Wensing [8] modeled an application shown in Figure 2.4. The critical steps on the way of modeling this application are listed below:

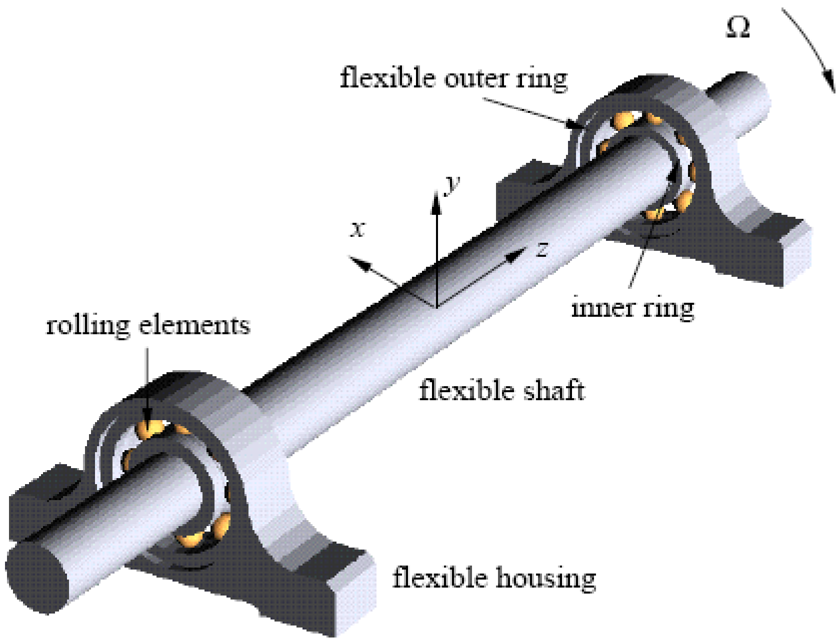

Figure 2.4 : The modeled application in reference [8]

- The outer rings and the housings are assumed as flexible whereas the balls and the inner rings are rigid. The contacts between the raceway and the ball are described as depicted in Figure 2.3.
- In order to apply CMS, the outer ring and the housing are connected to each other using linear constitutive relation.
- One of the outer rings has an axial movement freedom.
- The other outer ring is fixed to the housing. The outer ring and the housing are modeled using solid elements. These models are reduced using the new CMS method.
- The elastic shaft has a rotational motion with a constant speed. The model of the shaft is also reduced using CMS method.
- The inner ring is assumed to be rigid and it is pres-fitted to the shaft. It has two translational and three rotational Degree of Freedoms (DOFs).
- The rolling elements are assumed to be rigid with only one translational DOF, so the rotational inertias of the elements are neglected.
- Spinning motion of rolling elements due to gyroscopic effects is included in the model. Furthermore, the contact angle variations due to preload conditions cause another linear stiffness and damping in the tangential direction of the contacts. This damping is also included in the model.
- The cage structure is not included in the model.
- Based on the assumptions listed above, the kinetic, potential and dissipative energies of the system are determined. Then, the waviness effects are included in the model.
- All these properties are implemented in a computer code. The brief flow chart of the software developed is shown in Figure 2.5.

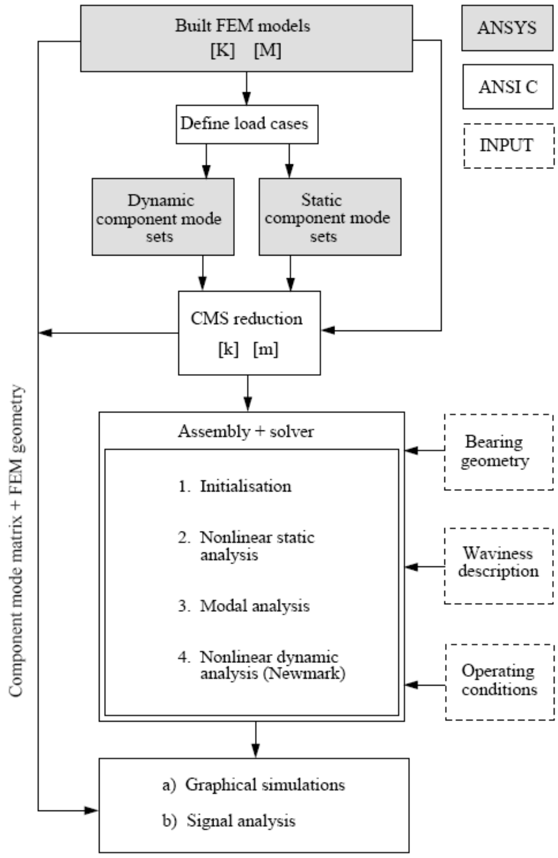

Figure 2.5 : Brief diagram of the computer software developed [8].

Finally, the numerical model developed is validated using experimental data. The experimental method followed in this study [8].

2.1.2.2. Multi-Body System Technique

Sopanen et al. [10] modeled a rotor- bearing system using multi-body simulation approach. They used a well-known commercial multi-body simulation software (ADAMS) for modeling an electric motor. They affirm that, with this approach, it is possible to model the rotor as a flexible body in order to observe the effects of individual components on the total response. Also the misalignments and waviness of the rings are implemented into the model.

In reference [10], a model of an electric motor (Figure 2.6), with 6010 type ball bearings at each side, is established. The bearing stiffness and damping values are taken from reference [9]. The shaft is assumed as flexible and modeled with lumped mass approach whereas the housings are modeled using linear springs and dampers. The symbols UB1 and UB2 in Figure 2.6 are the unbalance masses located on the disc and rotor, respectively. The shaft is assumed to rotate with a constant rotational speed.

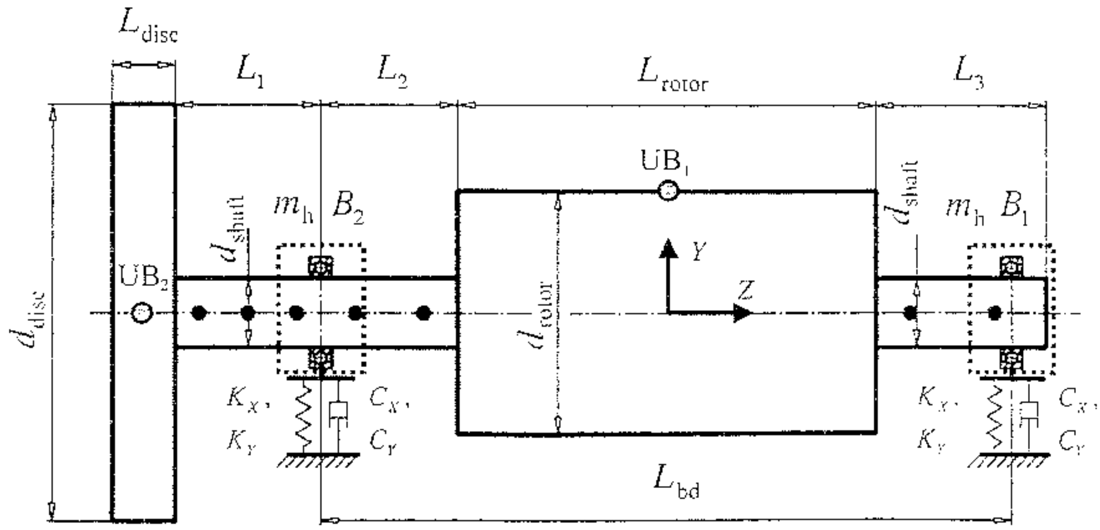

Figure 2.6 : The schematic view of the electric motor model in [9].

The equations of motion are solved under these assumptions and the results are compared to the analytical solutions and empirical data available in the literature.

It is observed in [9] that the ball bearing model developed in reference [9] yields acceptable results. Also, the effects of clearance and waviness are investigated. It is seen that the waviness factor creates vibrations at frequencies equal to the rotational speed times the waviness order.

2.1.3. Experimental Methods about Vibrations of Rotor-Bearing Systems

Several experimental methods are being used for measuring the vibrations caused by bearings. In the literature, the main objective of these experimental methods is to detect the defects of bearings [12, 13]. There are also experimental studies made in order to validate numerical models [8].

2.1.3.1. Methods for Diagnosis of Bearing Faults

Tandon and Choudry [12] discussed various experimental techniques of detecting bearing defects. The analyses are classified into two parts as time-domain and frequency-domain analyses. For frequency domain analysis, it’s crucial to filter the vibration signal. For a better detection, enveloping is also a good technique [13]. As shown in the envelope spectrum can give more clear information about faults. Based on the evaluation of amplitude modulation of random vibration and structural resonance, analysis is an efficient way to detect, diagnose and evaluate the condition of a rolling element bearing. Envelope analysis also has a much broader field of application if one considers that its main benefit is to 'shift' the high frequency modulation effect into the low frequency range. It therefore removes the need for an extremely high resolution that is often incompatible with the lack of speed stability encountered in rotating machines. Amplitude demodulation of pure tone components such as slot harmonics in electrical machines by the slip frequency; the gear meshing frequency by one of the gears; or the blade passing frequency by the rotating speed are all indicators of much sought after fault identification [13].

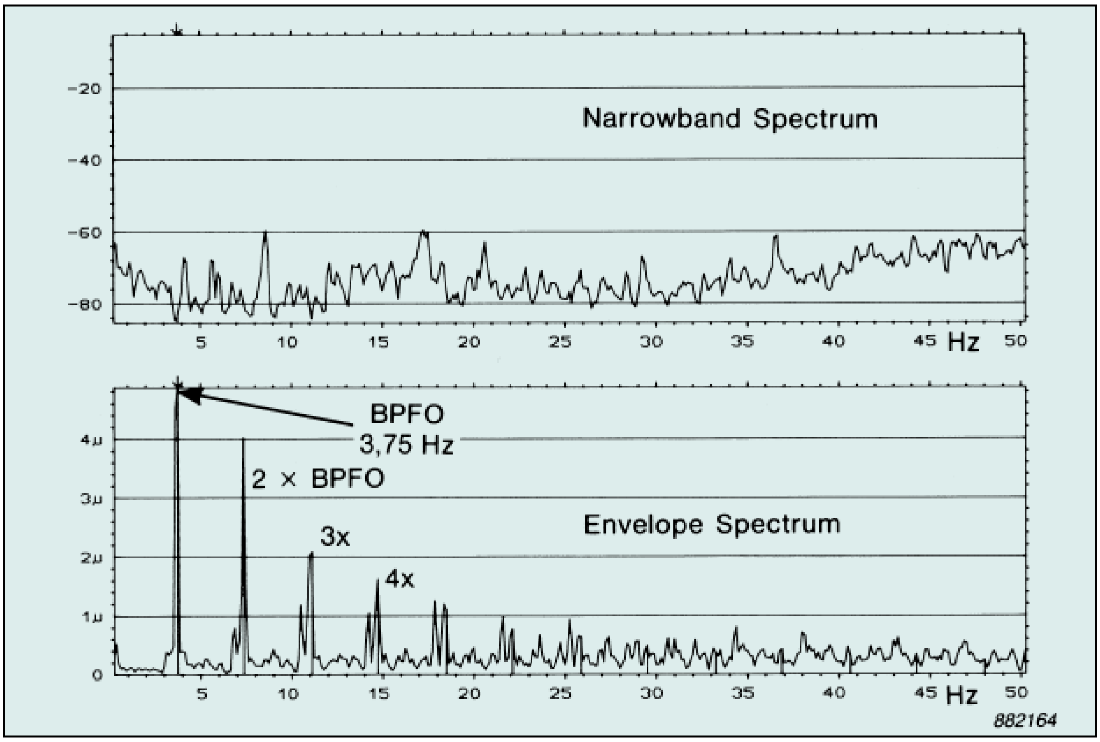

Figure 2.7 : Comparison of frequency spectrum and envelope spectrum of a defected bearing.

Order tracking is also a common technique being used while investigating of bearing vibrations. A signal's amplitude and/or the phase information are carried through the order spectrum, as a rotation frequency-dependent function [14]. Order analysis gives an opportunity to define and display the dynamic behaviours that are strongly related to rotation speed. As the vibrations excited by bearings depend on rotational speed, the order tracking analysis becomes very useful. Detailed information about order tracking analysis is included in chapter 3. Also Wensing [8] used this technique while verifying the numerical model.

2.1.3.2. Methods for Validation Procedures of Numerical Models

Wensing [8] used a standard test spindle, shown in Figure 2.8, for measuring the vibration behavior of ball bearings. The effects of other rotating components are eliminated due to the design of the testing system. It is claimed that this spindle is suitable for measuring bearing induced vibrations.

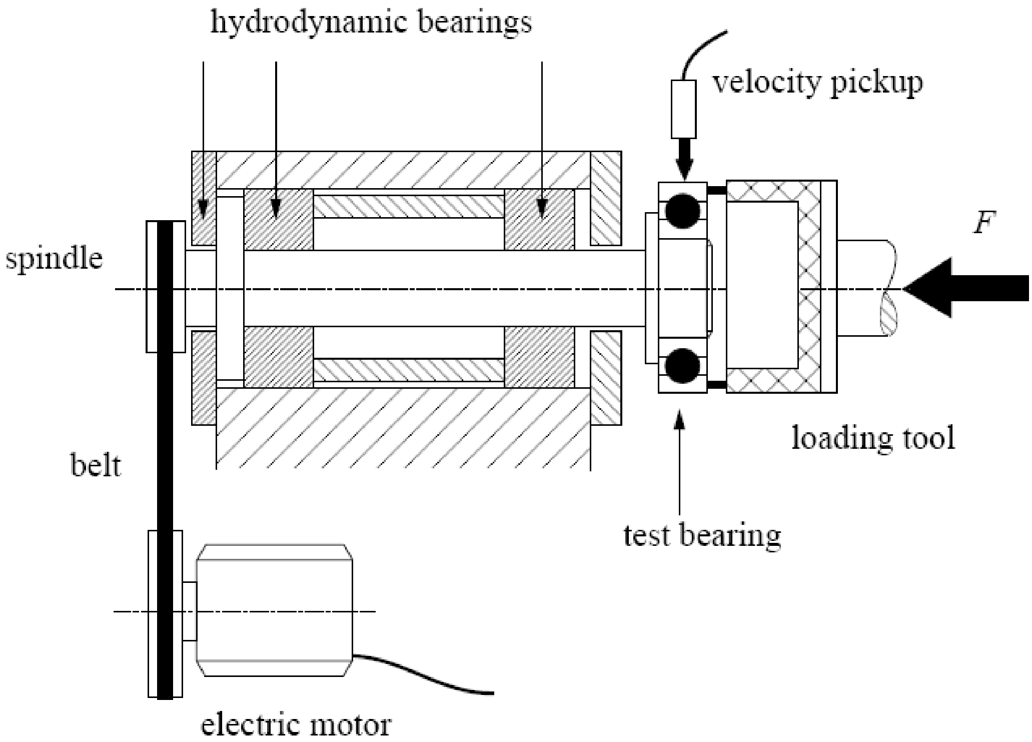

Figure 2.8 : Standard hydrodynamic test spindle for vibration testing of ball bearings [8].

The test spindle in Figure 2.8 is configured to rotate at 1800 RPM for bearings with maximum 100 mm outer ring diameter. An axial load is applied to the outer ring of the bearing. The vibration of the bearing is measured from the outer ring by means of velocity pickup. The research presented in [8] also contains measurements taken from another standard test spindle, which can be used for high speed applications (Figure 2.8). This time vibration is measured with accelerometers. Aerostatic bearings provide minimum friction, so that the effects of the structure to the vibrations are minimized. This enables to observe only the effects of investigated ball bearing on global vibration.

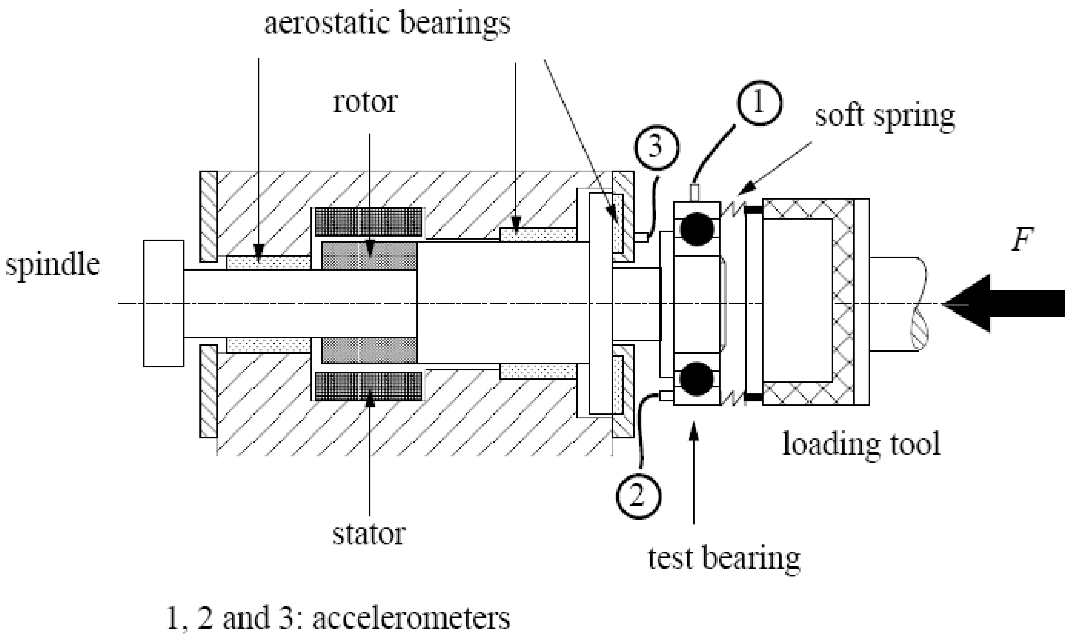

Figure 2.9 : Schematic view of the test Spindle which can be used for high speed applications [8].

The critical frequencies, where natural frequencies and bearing frequencies intersect, can be observed with the help of order tracking technique. On the other hand, Campbell diagrams, which is described in section 2, also gives satisfactory information about critical frequencies. Reference [8] also contains Campbell diagrams obtained using measured data. A typical example is shown in Figure 2.10

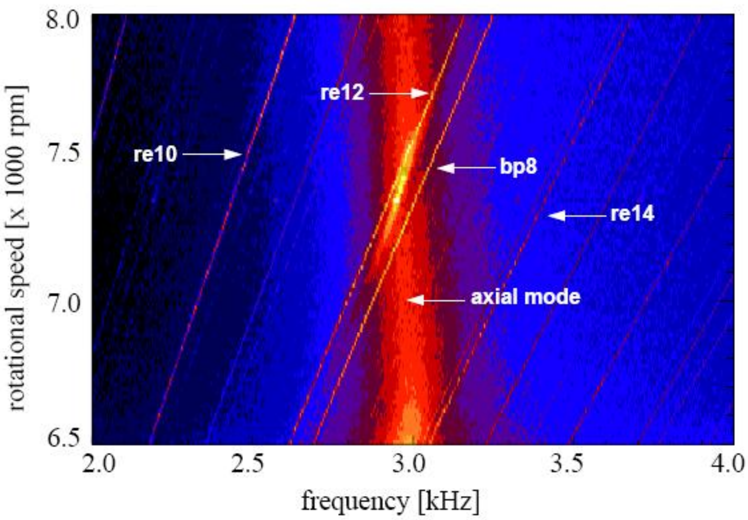

Figure 2.10 : Outer Ring’s Vibrations Shown in Campbell diagram [8].

3. THEORY

3.1. Theoretical Background for Numerical Model

The model of a structure created at the computer environment is named as numerical model. In recent years, due to the developments of the computer technology, dynamics of structures can be predicted by using computer codes and commercial softwares. Finite element method and multi-body dynamics approximations are widely used when analyzing the dynamic behaviours of complex systems. In rotating machinery, the dynamic behaviors of the systems may change significantly as a function of the rotational speed. This is because of the complications originating from bearings and due to the additional forces created due to rotation. This phenomenon complicates the model development and makes the predictions of vibrations in rotating machinery difficult. In order to simplify the problem, various assumptions are usually made during the modelling process. Also, some analytical relationships and/or empirical data can be utilized during model development. This chapter presents fundamental theoretical background necessary for, modelling rotating structures with ball-bearings. Furthermore, the procedure of numerical modelling is also discussed in this chapter.

3.1.1. Dynamic Characteristics of Ball-Bearings

3.1.1.1. Contact Stiffness in Ball-Bearings

Loads acting between the rolling elements and raceways develop only small areas of contact [15]. For ball bearings, this contact area is rather small and this kind of contact is named as point contact. Stiffness parameter associated with such contacts is usually calculated by using Hertzian Theory. Lubrication must be taken into account when modeling ball bearings that run at high operational speeds. This type of contact is called elastohydrodynamic (EHD) contact. In this study, the stiffness and damping effects of the lubrication film is neglected. The assumption made here is based on a dry contact mechanism.

The rolling elements are in contact with the inner and outer raceways in a ball bearing. The surface of a rolling element is convex whereas the surface of the outer raceway is concave. The surface of the inner raceway is convex in the direction of motion and concave in the transverse direction [8]. Figure 1 shows major geometric features of a ball bearing:

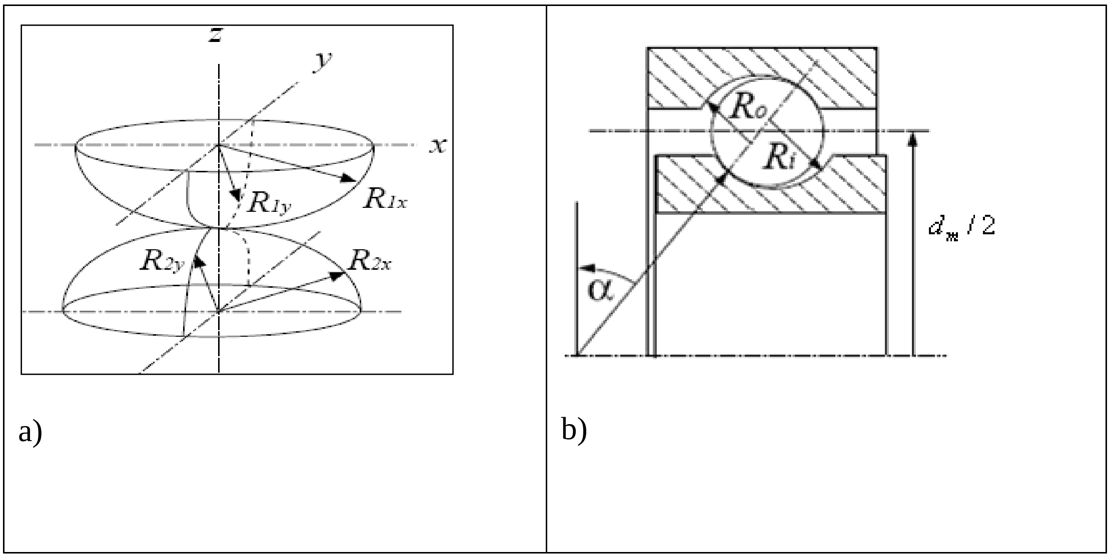

Figure 3.1 : a) Contacting bodies b) Geometric features of the contact region of a ball bearing [8].

$$R_{1x} = R_{re} \quad \textbf{(3.1)}$$

$$R_{1y} = R_{re} \quad \textbf{(3.2)}$$

$$R_{2x} = \frac{d_m/2}{\cos(\alpha)} - R_{re} \quad \textbf{(3.3)}$$

$$R_{2y} = -R_i \quad \textbf{(3.4)}$$

R_{re} denotes the radius of the ball itself and the equations above demonstrates the radii of curvature for the inner raceway- ball contacts. The R_{1x} and R_{1y} are same with the ones in and in (3.1) and (3.2) the radii of curvature for the outer contacts are:

$$R_{2x} = -(\frac{d_m / 2}{\cos(\alpha)} + R_{re}) \quad \textbf{(3.5)}$$

$$R_{2y} = -R_o \quad \textbf{(3.6)}$$

The so-called contact angle is a parameter which affects the radii of curvature of the raceway. However, when calculating the reduced radii, the assumption of a zero degree contact angle causes only a small error. Frequently, the shape problem in this type of contacts is reduced to the problem of a paraboloid shaped surface approaching a flat one. R, the radius of curvature of the paraboloid and R_d, curvature difference are described in [8] as

$$\frac{1}{R} = \frac{1}{R_x} + \frac{1}{R_y} \quad \textbf{(3.7)}$$

$$R_d = R(\frac{1}{R_x} - \frac{1}{R_y}) \quad \textbf{(3.8)}$$

$$\frac{1}{R_x} = \frac{1}{R_{1x}} + \frac{1}{Rx} \quad \textbf{(3.9)}$$

$$\frac{1}{R_y} = \frac{1}{R_{1y}} + \frac{1}{R_{2y}} \quad \textbf{(3.10)}$$

When a normal load is applied to the two contacting bodies, the point contact expands to an ellipse, an ellipticity parameter occurs

$$k_e = \frac{a_e}{b_e} \quad \textbf{(3.11)}$$

as ae and be are semi-minor and semi-major axes of this ellipse geometry [9]. Also it can be defined as a function of curvature difference R_d and the elliptic integrals of the first ξ and second ζ kind as [16]

$$k_e = \left[\frac{2\xi - \zeta(1+R_d)}{\zeta(1-R_d)} \right]^{1/2} \tag{3.12}$$

where

$$\xi = \int_0^{\pi/2} \left[1-(1-\frac{1}{k_e^2})\sin^2\varphi \right]^{-1/2} d\varphi \tag{3.13}$$

$$\zeta = \int_0^{\pi/2} \left[1-(1-\frac{1}{k_e^2})\sin^2\varphi \right]^{-1/2} d\varphi \tag{3.14}$$

where φ is an auxiliary angle. As can be seen, iteration procedure is required in order to determine the ellipticity parameter ke, and elliptic integrals. Brewe and Hamrock [17] used one point iteration and curve fitting techniques and obtained the approximation formulae given below:

$$\bar{k}_e = 1.0339 \left(\frac{R_y}{R_x} \right)^{0.6360} \tag{3.15}$$

$$\bar{\xi} = 1.0003 + 0.5968 \frac{R_x}{R_y} \tag{3.16}$$

$$\bar{\zeta} = 1.5277 + 0.6023 \ln\left(\frac{R_y}{R_x} \right) \tag{3.17}$$

The stiffness coefficient at the contact for the elliptical contact assumption can be calculated as:

$$K_c = \pi \bar{k}_e A E' \sqrt{\frac{R\bar{\xi}}{4.5\bar{\zeta}^3}} \tag{3.18}$$

where the effective modulus of elasticity, E', is defined as:

$$\frac{1}{E'}=\frac{1}{2}\left(\frac{1-\upsilon_1^2}{E_1}+\frac{1-\upsilon_2^2}{E_2}\right) \qquad \textbf{(3.19)}$$

E is the modulus of elasticity and υ is the Poisson's ratio and the subscripts refer to solids 1 and 2. In the case of ball bearing, both of the solids have the same elasticity properties [9]. The Kc only refers to one contact, for example the contact between the inner ring and ball. If the ball is contacting to both the inner ring and the outer ring, the total stiffness coefficient must be determined with the summation of these two stiffness values.

3.1.1.2. Ball Bearing Geometry and Kinematics

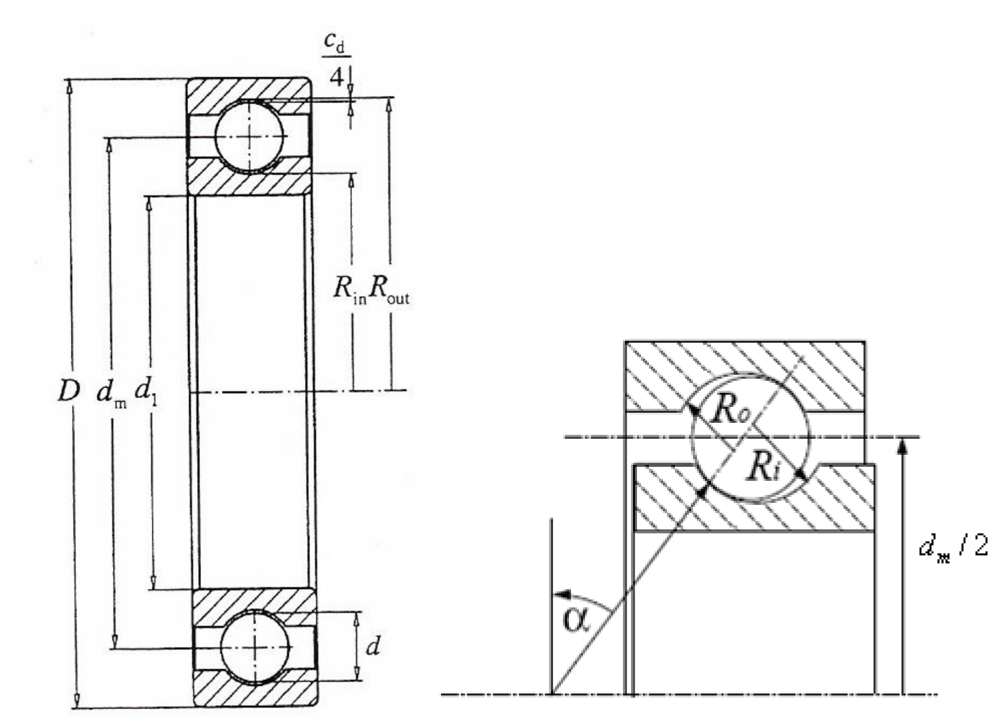

Figure 3.2 : Geometric Features of Ball Bearing [9].

D = Outer diameter d_i = Bore diameter	R_i = Inner groove radius R_o = Outer groove radius

d_m = Pitch diameter R_{in} = Inner raceway radius R_{out} = Outer raceway radius	d = Ball diameter C_d = Diametral clearance R_{re} = Ball radius α = Contact angle

The key dimensions of a deep groove ball bearing are shown in Figure 3.2. The bearing *pitch diameter* is the mean of the inner and outer race contact diameters an can be defined as:

$$d_m = R_{in} + R_{out} \tag{3.20}$$

The diametral clearance is defined as

$$C_d = 2(R_{out} - R_{in} - d) \tag{3.21}$$

Diametral clearance can be seen as a maximum distance within which one race move freely within another race in radial direction. In practice, both the inner and outer race radii are not known accurately. They are not generally defined in catalogues. On the other hand, pitch diameter and diametral clearance are usually known.

Race conformity is a measure of the geometrical conformity of the race and the ball in a plane that passes through the centre of the bearing and is transverse to the race. Race conformity is defined as the ratio between the race groove radius and ball diameter [9].

$$R_r = \frac{r}{d} \tag{3.22}$$

Also o*sculation* is another term about ball bearing geometry, which describes the ratio between the ball radius and the radius of curvature of the raceway in the transverse direction. Hence, for the inner and outer osculations it follows:

$$f_i = \frac{R_i}{R_{re}} \tag{3.23}$$

$$f_o = \frac{R_o}{R_{re}} \tag{3.24}$$

The perfect race conformity is equal to 0.5. In general, good conformity between the race and the ball decreases the maximum contact pressure, [9]. Decreasing the contact pressure reduces fatigue damage to the rolling surfaces; however, good conformity increases the heat generation. For these reason, race conformity in ball bearings ranges between 0.51 and 0.54, and 0.52 is the most common value.

Contact angle is another critical parameter about ball bearings. But in deep-groove ball bearings the contact angle is very close to zero. However, it depends on the diametral clearance of the bearing and it can be critical for preloaded case.

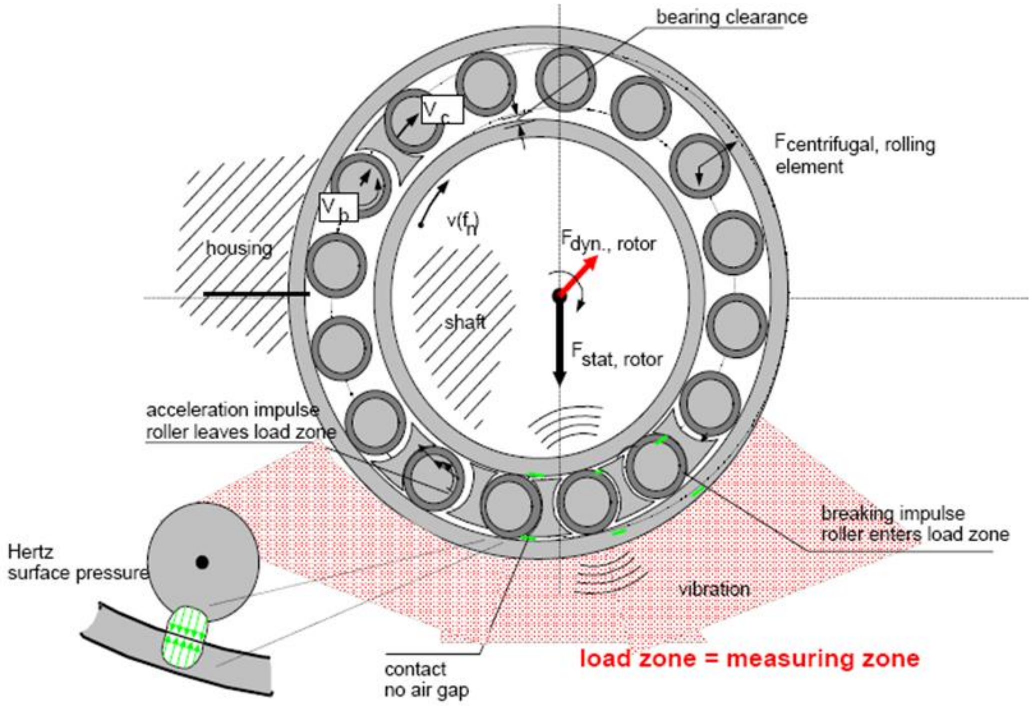

Figure 3.3 : Load zone and forces acting on a ball bearing [13]

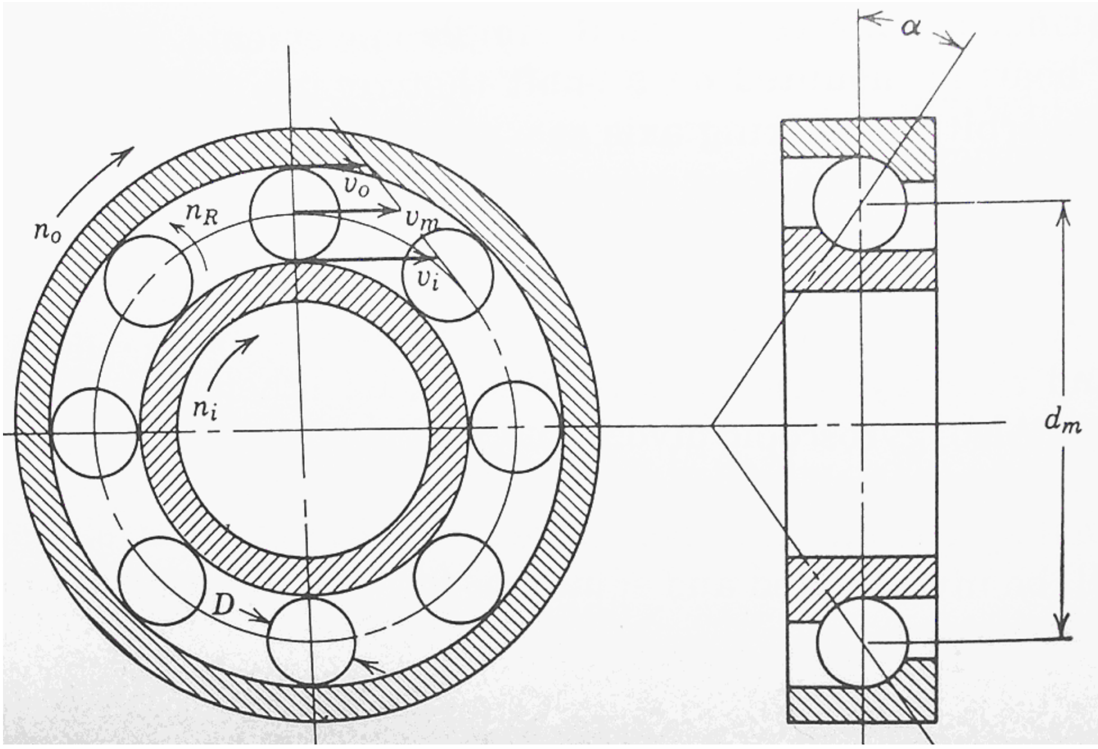

Figure 3.4 : Speeds of each elements of a ball bearing an definition of contact angle [15]

Unlike other bearings, motions occurring in ball bearings are not restricted to simple movements [15]. As shown in Figure 3.3 and Figure 3.4 due to geometric features, different components have different rotational speeds and different loading conditions occur. According to Harris [15] the speeds of the ball bearing components are:

Cage speed:

It is known for a rotation about an axis;

$$v = \omega r \tag{3.25}$$

in which ω is the angular velocity in radians per second. And v is the tangential velocity in m/s. Hence for the inner and outer ring of a ball bearing these velocities are:

$$v_i = \frac{1}{2}\omega_i(d_m - d\cos\alpha) \tag{3.26}$$

similarly

$$v_o = \frac{1}{2}\omega_o(d_m + d\cos\alpha) \tag{3.27}$$

since

$$\omega = \frac{2\pi n}{60} \tag{3.28}$$

in which n is in rpm.

$$v_i = \frac{\pi n_i}{60}(d_m - d\cos\alpha) \tag{3.29}$$

and

$$v_o = \frac{\pi n_o}{60}(d_m - d\cos\alpha) \tag{3.30}$$

If there is no gross slip at the raceway contact, then the velocity of the cage and rolling element set is the mean of the inner and outer raceway velocities. Hence;

$$v_m = \frac{\pi}{120}[n_i(d_m - d\cos\alpha) + n_0(d_m + d\cos\alpha)] \tag{3.31}$$

since;

$$v_m = \frac{\pi d_m n_m}{60} \tag{3.32}$$

Cage speed is the rotational speed of the cage and it can be determined as a function of the inner and outer shaft speeds and the geometric parameters as:

$$n_m = \frac{1}{2}[n_i(d_m - d\cos\alpha) + n_0(d_m + d\cos\alpha)] \tag{3.33}$$

Ball spinning speed:

Assuming no gross slip at the inner raceway-ball contact, the velocity of the ball is identical to that of the raceway at the point of contact. Hence,

$$\frac{1}{2}(\omega_m - \omega_i)(d_m - d\cos(\alpha)) = \frac{1}{2}\omega_R d \quad \textbf{(3.34)}$$

Therefore, since n is proportional to ω

$$n_R = \frac{1}{2}\frac{(n_m - n_i)(d_m - d\cos(\alpha))}{d} \quad \textbf{(3.35)}$$

When n_m is substituted:

$$n_R = \frac{1}{2}\frac{d_m}{d}(n_m - n_i)(1 - \frac{d\cos(\alpha)}{d_m})(1 + \frac{d\cos(\alpha)}{d_m}) \quad \textbf{(3.36)}$$

When the outer ring is considered as constant, *ball spin speed* is:

$$n_R = \frac{1}{2}\frac{d_m}{d}n_i(1 - \frac{d\cos(\alpha)}{d_m})^2 \quad \textbf{(3.37)}$$

3.1.1.3. Ball Bearing Damping

Dietl *et al.* [18] listed the sources of bearing damping as:

- Lubricant film damping in rolling contacts;
- Material damping due to the Hertzian deformation of rolling bodies;
- Damping in the interface between the outer ring and bearing housing.

Experimental studies showed that damping of a bearing decreases when the rotation speed increases [9, 18]. In this current study, a constant damping value, based on the experimental data, is used due to the relatively small damping in the bearing.

3.1.2. Vibration generation in ball bearings

3.1.2.1. Parametric excitations

Even if the geometry of a ball bearing is perfect, it will still produce vibrations. The vibrations are caused by the rotation of a finite number of loaded rolling contacts between the balls and the guiding rings. The varying contact conditions cause, time-dependent stiffness values. In general, a time varying stiffness causes vibrations, even in the absence of external loads. Since the stiffness can be regarded as a system parameter, the variable stiffness leads to a so-called *parametric excitation* [8].

While the shaft is rotating, applied loads are supported by a few balls restricted to a narrow load region and the radial position of the inner ring with respect to the outer ring depends on the elastic deflections at the ball to raceway contacts. Balls are deformed as they enter the loaded zone where the mutual convergence of bearing rings takes place, and the balls rebound as they move to the unloaded region as shown in Figure 3.5. As the positions of the balls change with respect to the applied load vector when they move from the loaded to the unloaded zone, the load distribution on the shaft changes thus producing a relative movement between inner and outer rings, i.e., a periodic relative motion between the rings must occur even though the bearing is geometrically perfect [7].

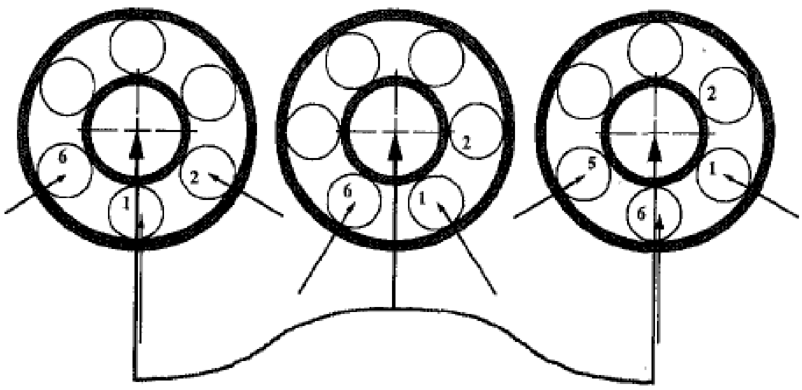

Figure 3.5 : Variation of total force for different positions of ball set [7]

When the contacts between the rings and rolling elements are assumed to behave like springs, it is seen that the number of springs under load is varying. This will result in a vibration at every ball pass when the system is viewed from a reference point. The frequency of this vibration is called the *ball passage frequency* (BPF). In mathematical terms, the BPF can be described as the cage speed times the number of balls. When N_b denotes the number of balls, the ball passage frequency in rpm is:

$$n_{bp} = \frac{1}{2} N_b [n_i (d_m - d\cos\alpha) + n_0 (d_m + d\cos\alpha)] \tag{3.38}$$

$$BPF = \frac{N_b}{120} [n_i (d_m - d\cos\alpha) + n_0 (d_m + d\cos\alpha)] \text{ Hz.} \tag{3.39}$$

The preload and diametral clearance affects the size of the load zone and the contact angle. Change in the load zone has a significant effect on the vibration amplitudes at BPF and its harmonics. As shown in Figure 3.6, when the clearance is increased the size of the load zone decreases and this leads to reduction of the numbers of load carrying balls. When the balls get into contact, the loads on them are greater so as the amplitude of the BPF vibrations are.

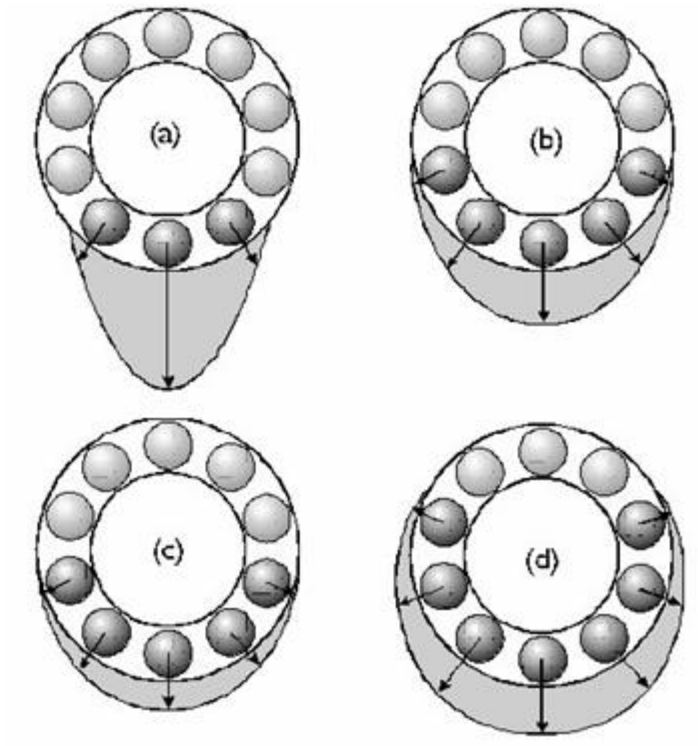

Figure 3.6 : Effect of the clearance and preload on load zone size a.) C_d >0, α <90° b.) C_d >0, α <90°c.) C_d =0, α =90° d.) C_d <0, α >90° (preload) [15]

Often, ball bearings are subjected to an externally applied load in order to establish preload to maintain Hertzian contacts. In a two-dimensional model, the effect of an axial load can be modelled by introducing a negative radial clearance as shown in Figure 3.7. In the case of a negative clearance and a perfect geometry, the outer ring of a ball bearing with rolling elements is loaded with eight uniformly distributed contact loads. The resulting displacement field of the outer ring consists of extensional deformations [8]

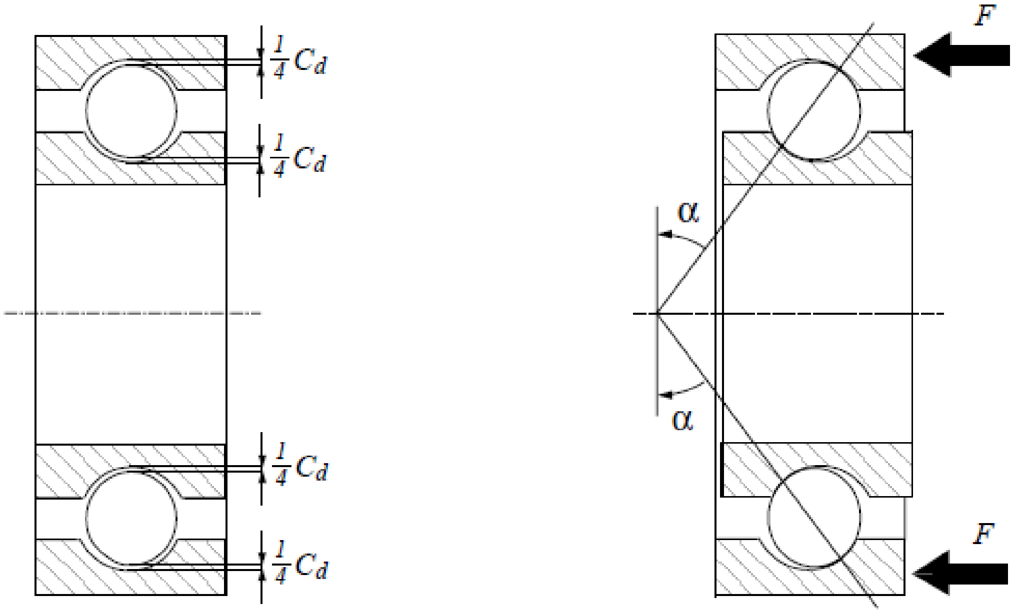

Figure 3.7 : Under an externally applied axial load, the radial clearance disappears and the bearing is loaded at contact angle α [8]

3.1.2.2. Vibrations caused by geometric imperfections

Defects responsible for damage to the bearing can be either localized or distributed. Localized defects, generally occurring as a result of the fatigue process, include cracks, pits or spalls as shown in Figure 3.8. Distributed defects, due to unavoidable manufacturing imperfections, include surface roughness, waviness, misaligned races and rolling elements with slightly different sizes. Vibration responses caused by localized defects are important in condition monitoring and system maintenance, while responses from distributed defects are used for quality inspection [2].

The defects on each component of the bearing cause excitations at different frequencies. These frequencies are called *bearing defect frequencies* which are excited by localized defects illustrated in

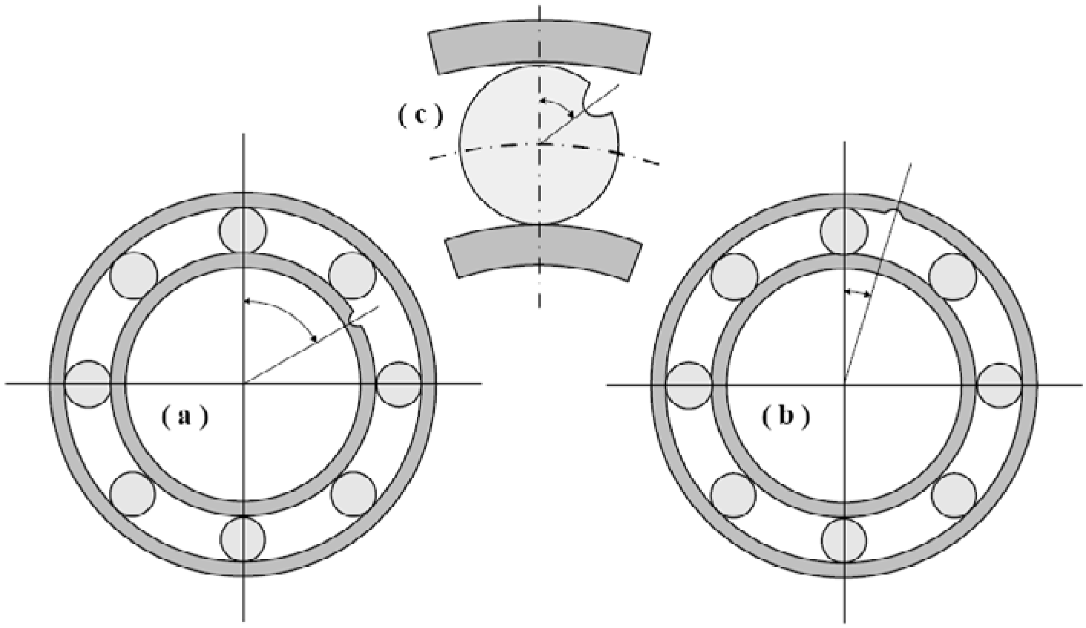

Figure 3.8 : Different positions of localized defects affecting a ball Bearing. (a) Defect on inner Race. (b) Defect on outer Race. (c) Defect on ball.

Ball pass frequency outer ring:

$$BPFO = \frac{N_b}{120}[(n_i - n_0)(d_m - d\cos\alpha)] \tag{3.40}$$

Ball pass frequency inner ring:

$$BPFI = \frac{N_b}{120}[(n_i - n_0)(d_m + d\cos\alpha)] \tag{3.41}$$

Ball spin frequency:

$$BSF = \frac{N_b}{120}[\frac{d_m}{d}(n_i - n_0)(\frac{1 - d\cos\alpha}{d_m})^2] \tag{3.42}$$

Waviness is also another factor that causes significant excitations. It can be defined as distributed sinusoidal imperfections of components. It generates vibrations at waviness orders times the cage speed. However, the effects of waviness on ball bearing vibrations are not modelled/investigated in this study.

3.1.3. Single-mass rotor dynamics

A brief summary of the theoretical background of rotordynamics is given in the following sections. Determination of natural frequencies and critical speeds for symmetrical shafts in case of both flexible and rigid assumptions supported by rigid and flexible anisotropic bearings are explained. Also, the gyroscopic effects on rotor systems are briefly discussed.

3.1.3.1. Flexible shaft in rigid bearings

A disc on the rotor can be idealized as a system comprising a single mass m mounted on a light flexible shaft which runs in rigid bearings. The centre of gravity of the rotor G is offset from the geometric centre C by a distance e. F_y and Myz are forces and moments acting on the shaft which has lateral and angular deflections, y and θ. Also, the rotor has an unbalance force $me\omega^2$ acting in the direction shown in Figure 3.9.

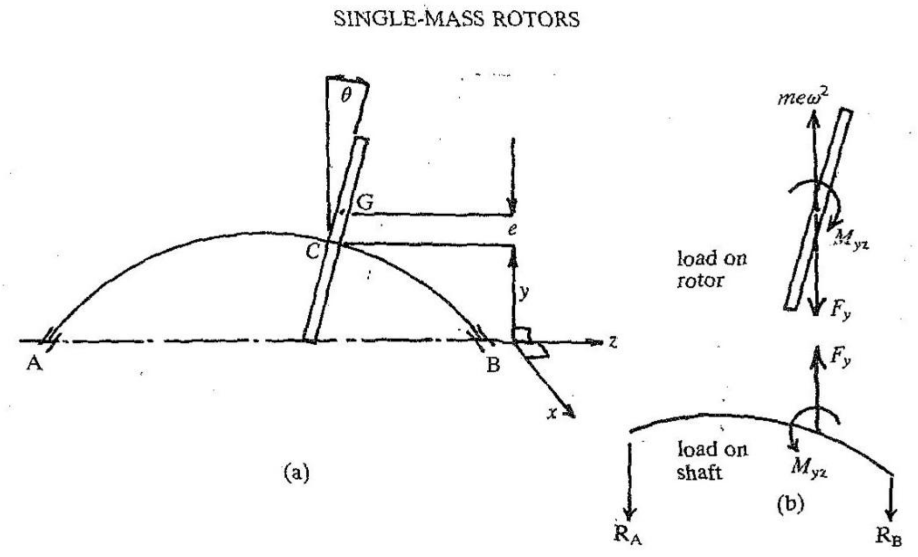

Figure 3.9 : a) Single mass-rotor mounted on a light flexible shaft running in rigid bearings, b) Loads applied to rotor [19]

The relationship between, Fy and Myz and the shaft deflection, y and θ take the form:

$$\begin{Bmatrix} y \\ \theta \end{Bmatrix} = \begin{pmatrix} ab(b-a)\big/3EIl & -(3a^2l-2a^3-al^2)\big/3EIl \\ ab(b-a)\big/3EIl & -(3al-3a^2-l^2)3EIl \end{pmatrix} \begin{Bmatrix} F_y \\ M_{yz} \end{Bmatrix} \tag{3.43}$$

Where a and b are the distances of the disc to the bearings, l is the length of the shaft, E is the modulus of elasticity and I is the shaft second moment of area. This equation can be simplified as:

$$\begin{Bmatrix} y \\ \theta \end{Bmatrix} = \begin{pmatrix} a_{11} & a_{12} \\ a_{21} & a_{22} \end{pmatrix} \begin{Bmatrix} F_y \\ M_{yz} \end{Bmatrix} \tag{3.44}$$

Where the terms a_{11} a_{22} a_{33} etc. are called influence coefficients. This equation can also be written in another form as:

$$\begin{Bmatrix} F_y \\ M_{yz} \end{Bmatrix} = \begin{pmatrix} k_{11} & k_{12} \\ k_{21} & k_{22} \end{pmatrix} \begin{Bmatrix} y \\ \theta \end{Bmatrix} \tag{3.45}$$

The equations of motion for the rotor mass are written as:

$$me\omega^2 - F_y = m\ddot{y} \tag{3.46}$$

$$M_{yz} = I_d\ddot{\theta} \tag{3.47}$$

Noting that for harmonic vibrations in frequency domain:

$$\ddot{y} = -\omega^2 y \tag{3.48}$$

and

$$\ddot{\theta} = -\omega^2\theta \tag{3.49}$$

may be substituted into the equations of motion and this leads to [19]:

$$\begin{Bmatrix} me\omega^2 \\ 0 \end{Bmatrix} = \begin{pmatrix} (k_{11} - m\omega_n{}^2) & k_{12} \\ k_{21} & (k_{22} - I_d\omega_n{}^2) \end{pmatrix} \begin{Bmatrix} y \\ \theta \end{Bmatrix} \tag{3.50}$$

which may than be arranged to give

$$\begin{Bmatrix} y \\ \theta \end{Bmatrix} = \begin{pmatrix} (k_{11} - m\omega_n{}^2) & k_{12} \\ k_{21} & (k_{22} - I_d\omega_n{}^2) \end{pmatrix}^{-1} \begin{Bmatrix} me\omega^2 \\ 0 \end{Bmatrix} \tag{3.51}$$

where ω is running speed and ω_n is natural frequency. This matrix equation gives the rotor deformation in the vertical plane with running speed (ω). The motion of the rotor in the x-z plane takes the same form, but is out of phase with that in the y-z plane because the forcing is 90° out of phase.

A plot of y/e against frequency ratio ω/ω_n for the case of a rotor mounted at shaft mid-span, a system first analyzed by Jeffcott (1919), is shown in Figure 3.9. It is known that as speed increases from zero to ω_n, vibration amplitude increases from zero to infinity. At speeds greater than ω_n vibration amplitude, tending to a minimum value of -e at very high speeds. The significance of the negative vibration amplitude here is that the shaft deflects in the opposite direction to the unbalance eccentricity e. It follows from this that at very high speeds y tends to -e, the rotor mass centre G moves toward the line joining the bearing centers.

The frequency ω_n is known as the system "whirling speed" or "critical speed" [19]. It is noteworthy that whirling is not a vibration of the shaft in the sense that a point on the shaft surface is subjected to a fluctuating stress, it simply means that it rotates in a bent configuration (in the shape of a banana). In the more general case, when the disc is mounted at the centre of the shaft, there are two critical speeds- one associated with lateral motion of the rotor and one associated with angular motion.

In the system shown in Figure 3.9 the forces related to deflection of the shaft are transmitted through bearings. The reaction forces on bearings are:

$$\begin{Bmatrix} R_A \\ R_B \end{Bmatrix} = \begin{pmatrix} b/l & -1/l \\ a/l & 1/l \end{pmatrix} \begin{Bmatrix} F_y \\ M_{yz} \end{Bmatrix} \tag{3.52}$$

which may be written as:

$$\{R\} = [I]\{p\} \tag{3.53}$$

whereas;

$$\{R\} = [I][k]\{d\} \tag{3.54}$$

$$= [I][k][Z]\{f\} \tag{3.55}$$

$$= [C]\{f\} \tag{3.56}$$

which may be written more explicitly as:

$$\begin{Bmatrix} R_A \\ R_B \end{Bmatrix} = \begin{pmatrix} c_{11} & c_{12} \\ c_{21} & c_{22} \end{pmatrix} \begin{Bmatrix} me\omega^2 \\ 0 \end{Bmatrix} \tag{3.57}$$

It can be shown from the above that the forces transmitted through the bearings are also maximum at the system critical speed. These forces are dynamic forces and are superimposed on any steady loads which may be present, for example, due to gravity loading.

In the system considered above, the vibration of the disc was accommodated by flexure of the shaft. The bearings are assumed as rigid. For some other applications the shaft and the rotor can be assumed as rigid whereas the bearings and pedestals can be considered flexible. In the study presented in this thesis, a single-mass disc and a flexible shaft form the rotor part, and the bearings are modeled as flexible components of the system. The anisotropy of the bearings is modeled via multi-body system commercial software.

3.1.3.2. Gyroscopic effects

In some machines the rotor mass is mounted on the shaft such that, at the location of the disc deflection of the shaft also tends to result in a change in slope of the shaft. This is generally the case especially for overhung rotors. The rotor will tend to whirl in conical path and centrifugal forces act on the rotor mass as shown in Figure 3.10. The effect of these centrifugal forces is to tend to straighten the shaft making it to behave as if it is constrained not to change the slope at the rotor location. Because of this, the deflection of the shaft will tend to decrease as its stiffness will effectively increase. As a result, there will be a corresponding increase in the system natural frequency [19].

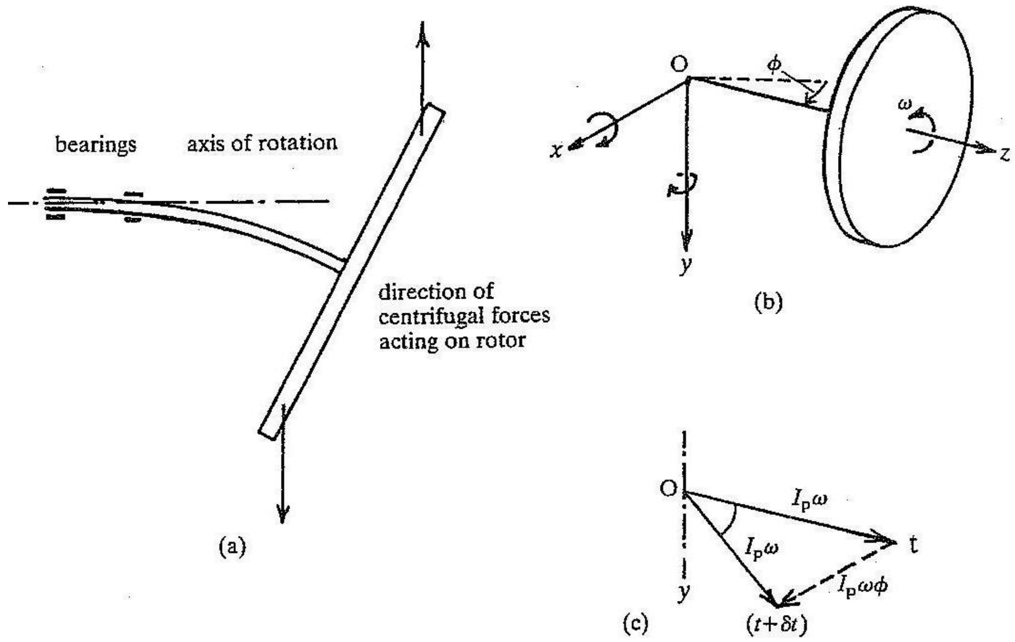

Figure 3.10 : Gyroscopic effects associated with a spinning rotor, (a) an overhung rotor mounted on flexible shaft; b) general angular motion c) angular momentum vectors shown in (b).$I_p\omega$ Are the vectors representing angular momentum about spin axis O_x/O_y, $I_p\omega\Theta$ is the change in momentum during time δt. [19]

The system shown in Figure 3.10 spins with angular velocity ω about the spin axis OZ axis. At the instant in time shown in the figure, the rotor is also processing with angular velocity $\dot{\theta}$ about a vertical axis OY. Figure 3.10 shows angular momentum vectors drawn (parallel to the axis of rotation they refer to, the direction of rotation being clockwise when viewed from the arrow tail) representing the system angular momentum at some time t and at a small interval of time later. It can be seen that the change in angular momentum over the time interval considered is $I_p\omega\Theta$ where I_p is the polar moment of inertia of the rotor, and so the gyroscopic moment which must be applied to produce this change, equal to the rate of change of angular momentum, is given $I_p\omega\dot{\theta}$. In Figure 3.10 the gyroscopic couple applied to the rotor (or strictly, the moment that reacts the gyroscopic couple by the rotor to the support structure), say M_g , must act about the axis Ox, since this axis corresponds with the orientation of the vector $I_p\omega\Theta$ in Figure 3.10, The angular sense of this couple is clockwise about Ox when viewed from O. The net moment about the axis Ox is equal to the product of rotor moment of inertia about the Ox axis and the angular acceleration about the Ox axis, that is:

$$M_x - M_g = I_d\ddot{\theta} \tag{3.58}$$

Where M_x is a moment which is applied to the rotor by the shaft and I_d is the rotor moment of inertia about a diameter. Alternatively, this may be written as:

$$M_x = I_p\omega\dot{\phi} + I_d\ddot{\theta} \tag{3.59}$$

A similar expression may also be developed describing the rotor motion in the xz plane as:

$$M_y = -I_p\omega\dot{\phi} + I_d\ddot{\theta} \tag{3.60}$$

The angular displacements of the rotor will be periodic and will take the form:

$$\phi = \phi_2 \cos\omega t + \phi_1 \sin\omega t \tag{3.61}$$

$$\theta = \theta_1 \cos\omega t + \theta_2 \sin\omega t \tag{3.62}$$

in general, for an isotropic system where the rotor support characteristics are the same in both directions, the amplitudes of ϕ and θ will be equal and in this case:

$$\theta = \psi \cos\omega t \tag{3.63}$$

$$\phi = \psi \sin\omega t \tag{3.64}$$

the motion in one direction lags behind that in the perpendicular direction by one quarter of a cycle. Moment in xz axis applied to the shaft can be defined as:

$$M = -(I_p - I_d)\omega^2\psi \tag{3.65}$$

In the case of an overhung rotor, the deflection and the slope of the rotor will take the form

$$z = \frac{l^3F}{3EI} + \frac{l^2M}{2EI} \tag{3.66}$$

and

$$\psi = \frac{l^2 F}{2EI} + \frac{lM}{EI} \tag{3.67}$$

The centrifugal force F is equal to $mz\omega^2$ where m is the rotor mass, I is the total moment of inertia and l is the shaft length.

Gyroscopic effects tend to be particularly significant in situations where there is either an overhung rotor (so that any forcing causes a considerable slope of the shaft at the rotor) or when the rotor runs at very high speeds. In cases where the rotor itself forms most of the shaft, as opposed to the case where the rotor is disc-like and is mounted on a relatively light shaft, gyroscopic effects are less significant.

3.2. Theoretical Background for Experimental Model

3.2.1. Experimental modal analysis

3.2.1.1. Measurement

FRF Measurements: The Frequency Response Function (FRF) is a fundamental function that can be used to identify the inherent dynamic properties of a mechanical structure such as natural frequencies, damping levels and mode shapes. FRF describes the input-output relationship between two points on a structure as a function of frequency. Since both force and motion are vectoral quantities, they have magnitudes and directions. Therefore, an FRF is actually defined between a single input DOF and a single output DOF. An FRF is a measure of *how much displacement, velocity, or acceleration response* a structure has *at an output DOF per unit of excitation force at an input DOF*. As shown in Figure 3.11. FRF is defined as the *ratio of the Fourier transform of an output response,* X (ω), *divided by the Fourier transform of the input force,* F (ω) *that* caused the output [20].

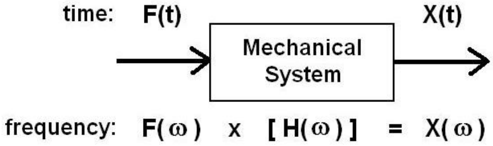

Figure 3.11 : Input, output definition and the system [20]

Depending on whether the response motion is measured as displacement, velocity, or acceleration, the FRF and its inverse can have a variety of names,

· **Receptance** ⇔ (displacement / force)

· **Mobility** ⇔ (velocity / force)

· **Inertance** ⇔ (acceleration / force)

· **Dynamic Stiffness** ⇔ (1 / Compliance)

· **Impedance** ⇔ (1 / Mobility)

· **Dynamic Mass** ⇔ (1 / Inertance)

Testing Real structures: When real continuous structures are considered it is known that they have an infinite number of DOFs and an infinite number of modes. From a testing point of view, a real structure can be *sampled spatially* at as many DOFs as desired/required. However, in practice, a small subset of the FRFs are usually measured on a structure, because of time and cost constraints.

As mentioned, it is possible to determine the modes that are within the frequency range of the measurements. Of course, the more we *spatially sample* the surface of the structure by taking more measurements, the more definition we will give to its mode shapes.

Modal Testing: In modal testing, FRF measurements are usually made under controlled conditions, where the test structure is artificially excited by using either an impact hammer or one or more shakers driven by using appropriate signals. A multi-channel FFT analyzer is then used to make FRF measurements between input and output DOF pairs on the test structure.

Measuring FRF Matrix Rows or Columns: Modal testing requires that FRFs be measured from *at least one row or column* of the FRF matrix. Modal frequency and damping are global properties of a structure, and can be estimated from any or all of the FRFs in a row or column of the FRF matrix. On the other hand, each mode shape is obtained by assembling together FRF numerator terms from at least one row or column of the FRF matrix.

When the output DOF is fixed and FRFs are measured for varying input DOFs, this corresponds to measuring elements from a *single row* of the FRF matrix. This is typical of a roving hammer impact test. When the input DOF is fixed and FRFs are measured for multiple output DOFs, this corresponds to measuring elements from a *single column* of the FRF matrix. This is typical of a shaker test.

The most common type of modal testing is done with either a single fixed input or a single fixed output. A roving hammer impact test using a single transducer is an example of single reference testing. The single fixed output is called the reference in this case. When a single fixed input (such as a shaker) is used, this is called SIMO (Single Input Multiple Output) testing. In this case, the single fixed input is the reference. When *two or more fixed inputs* are used, and FRFs are calculated between each of the inputs and multiple outputs, FRFs from multiple columns of the FRF matrix are obtained. This is Multiple Reference or MIMO (Multiple Input Multiple Output) testing. In this case, the inputs are the references. Similarly, when *two or more fixed outputs* are used, and FRFs are calculated between each output and multiple inputs, this is Also multiple reference testing. Multi-reference testing is done for the following reasons:

The structure cannot be adequately excited from one reference point.

All modes of interest cannot be excited from one reference.

The structure has *repeated roots*, modes that are so closely coupled that more than one excitation is needed to identify them.

With the ability to compute FRF measurements in an FFT analyzer, impact testing has become the most popular modal testing method. It is a fast, convenient, and low cost way of finding the modes of machines and structures. The following equipment is required to perform an impact test:

1. An *impact hammer* with a load cell attached to its head to measure the input force.

2. An *accelerometer* to measure the response acceleration at a fixed point and direction.

3. A 2 or 4 channel *FFT analyzer* to compute FRFs.

4. *Post-processing modal software* for identifying modal parameters and displaying the mode shapes in animation.

A wide variety of structures and machines can be impact tested. Different sized hammers are required to provide the appropriate impact force, depending on the size of the structure; small hammers for small structures, large hammers for large structures.

3.2.1.2. Analysis

Obtaining modal parameters: The different ways in which modal parameters can be obtained, both analytically and experimentally are listed here. A growing amount of finite element modeling, with extraction of modal parameters is being done to solve structural dynamics problems. Experimental modal analysis is also done for this same purpose. The majority of modern experimental modal analysis relies upon the application of a modal parameter estimation (curve fitting) technique to a set of FRF measurements. As indicated in Figure 3.12, the inverse FFTs of FRFs can also be computed and curve fitting techniques applied to their equivalent Impulse Response Functions.

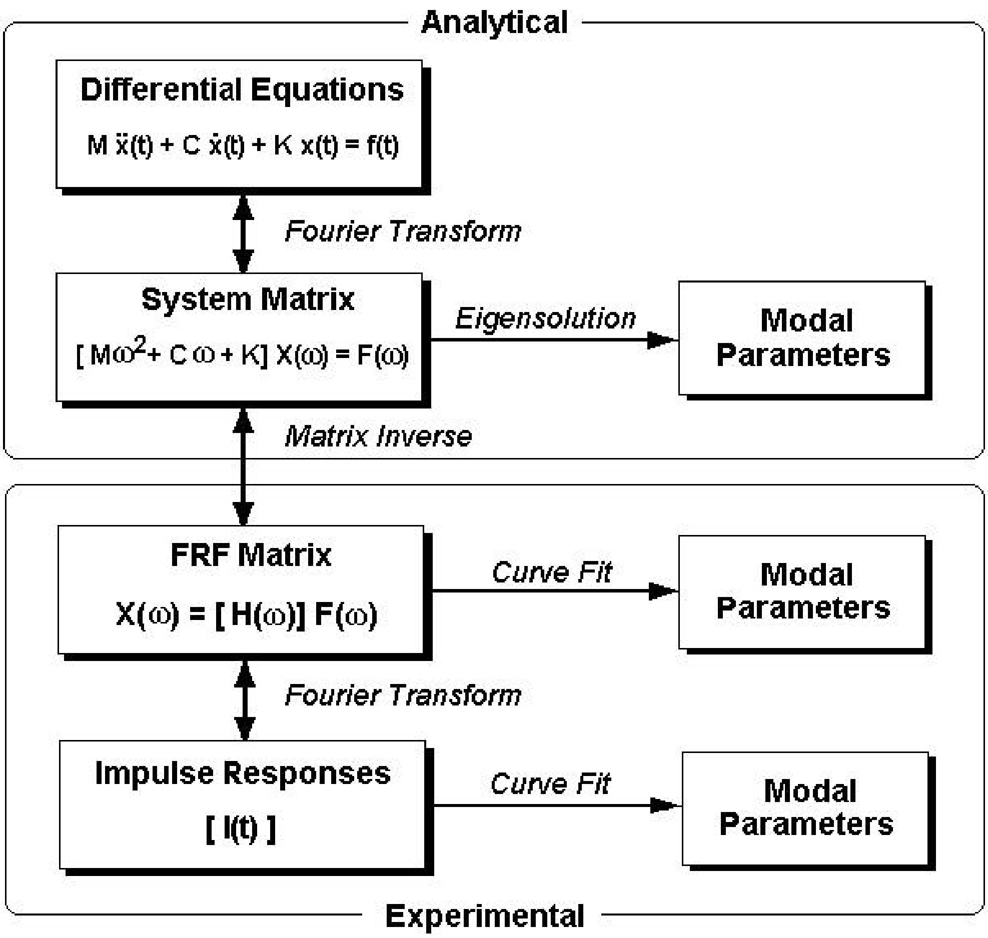

Figure 3.12 : FRF Measurements [20]

3.2.2. Order tracking analysis

Analysis of vibration or acoustic signals from rotating machines is often preferred in terms of order spectra rather than frequency spectra. An order spectrum gives the amplitude and/or the phase of the signal as a function of harmonic order of the rotation frequency. This means that a harmonic or sub-harmonic order component remains in the same analysis line independent of the speed of the machine. The technique is called order tracking, as the rotation frequency is being tracked and used for analysis (Figure 3.13). Most of the dynamic forces exciting a machine are related to the rotation frequency so interpretation and diagnosis can thus be greatly simplified by use of order analysis.

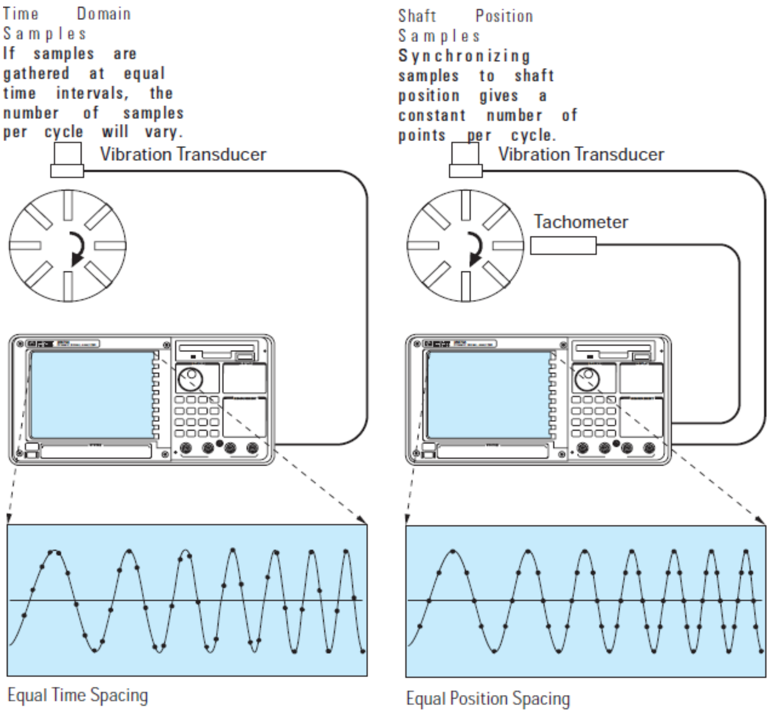

Figure 3.13 : a) FFT analyzer, sampling in Time b) Order analyzer sampling in revolution [14]

The classical problem of smearing of the frequency components caused by speed variations of the machine is solved by using order analysis. In situations where the frequency components from a normal frequency analysis are smeared together, proper diagnosis will only be facilitated with order analysis.

Of particular interest is the analysis of the vibrations during a run-up or a coast-down of a machine in which case the structural resonances are excited by the fundamental or the harmonics of the rotational frequencies in the mechanical system.

Determination of the critical speeds, where the normal modes of the rotating shaft are excited, is very important on large machines and rotating systems with various components [14].

When an FFT analyzer in the normal sampling mode with a fixed sampling frequency (i.e., nontracking) is used and the spectrum at certain fixed steps in rotation speed of the machine is plotted, the so-called Campbell diagram is obtained. This is a 3-D waterfall or contour type of plot, where vibration levels as a function of frequency are plotted against rotation speed (RPM) of the machine. This means that the harmonic components appear on radial lines through the point (0Hz, 0 RPM) while horizontal straight lines represents the structural resonances and natural frequencies. Thus such a plot can be very useful (Figure 3.14).

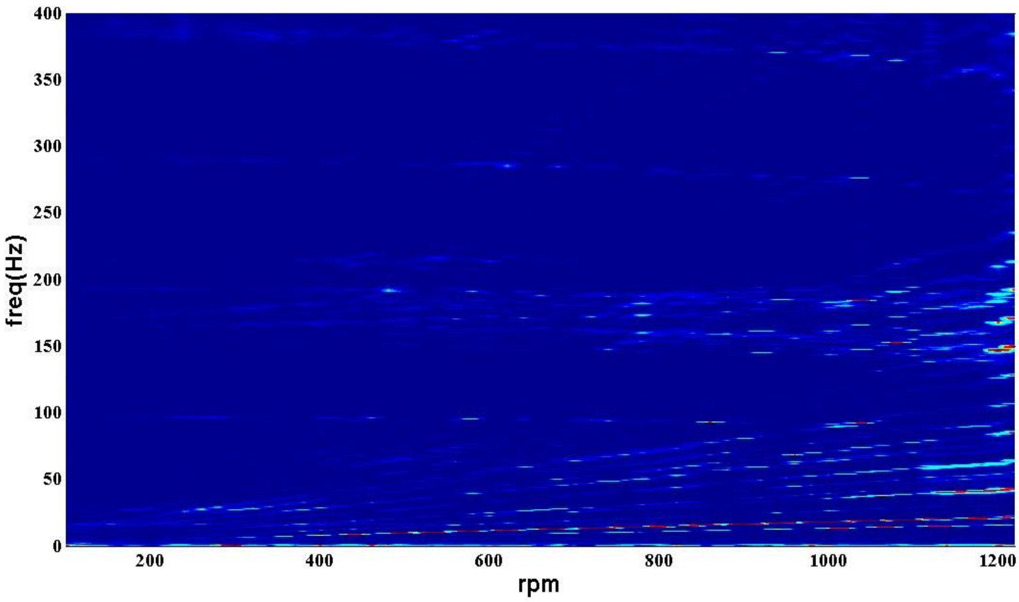

Figure 3.14 : A Campbell diagram obtained from FFT Analyzer

The disadvantage of this technique is the smearing of the components, which appears because the time window used for the individual spectra represents a certain sweep in the speed. The power of the components becomes spread over several lines. In particular, high frequency components in the spectrum, such as tooth mesh frequencies, might be smeared so much that details in sideband structures are lost in the analysis [14].

4. DEVELOPING A NUMERICAL MODEL FOR A ROTOR-BALL BEARING SYSTEM

In order to perform dynamic analyses and also to optimize the performances of machines, numerical models validated by experimental data are necessary. In this chapter, numerical models for ball bearings and rotor parts are developed and validated separately. Then, these models are assembled so as to predict the dynamic behaviour of the whole assembly.

First of all, a specific type of a deep groove ball bearing is modelled. The FE models of the ball bearing components are built. During this process, some assumptions are made about the flexibilities of some components of the ball bearing system. Then, a multi-body system model of the ball bearing system under consideration is built using Msc. ADAMS software. Afterwards, a rotor part is designed, which included some features that made it possible to observe not only the effects of ball bearings and unbalances on vibration behaviour but also the gyroscopic effects clearly. The flexibility of the rotor parts are modelled based on FE appoach and the model is validated using the results of experimental modal analysis. Finally, the rotor model and the ball bearing model are assembled. In the light of the experimental procedure, which will be represented in the next chapter, the model is modified and improved. In chapter 6, the comparison of the results and the modifications of the numerical model are described in detail.

4.1. Modelling the Ball Bearing

During this study, a single row deep groove ball bearing is used. The designation of the ball bearing studied here is 6206. The 3D geometry of the bearing with no shield or seal is given below in Figures 4.1. In Figure 4.2 the sectional view of the ball bearing with critical dimensions are shown. The description of these dimensions and load capacity properties of the ball bearing studied here are listed in Table 4.1.

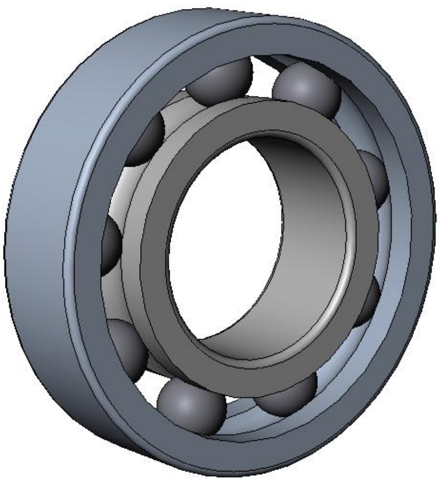

Figure 4.1 : Front view of the 3D model of 6206 ball bearing

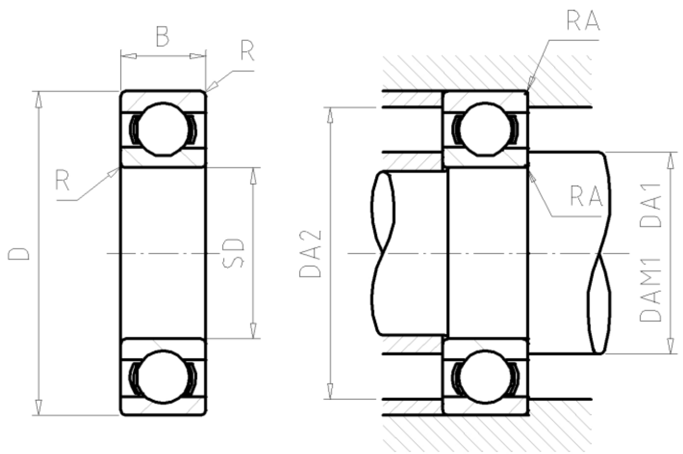

Figure 4.2 : Section view of the 6206 ball bearing

Table 4.1 : The dimensions and load carrying capacities of 6206 bearing

STAN (Standard)	Standard
ORDER (Bearing No.)	6206
SD (Inside Diameter / mm)	30
D (Outside Diameter / mm)	62
B (Width / mm)	16
R (Chamfer Dimension / mm)	1
CR1 (Basic dynamic load rating / N)	19500

COR1 (Basic Static Load Ratings / N)	11300
CR2 (Basic dynamic load rating / kgf)	1980
COR2 (Basic Static Load Ratings / kgf)	1150
LG (Limiting Speed Grease / rpm)	11000
LO (Limiting Speed Oil / rpm)	13000
DAM1 (Abutment and Fillet Dimension min. / mm)	35
DA1 (Abutment and Fillet Dimension max. / mm)	38.5
DA2 (Abutment and Fillet Dimension max. / mm)	57
RA (Abutment and Fillet Dimension max. / mm)	1
MASS (Mass / kg)	0.199

4.1.1. Modelling the components of the ball bearing

A ball bearing consists of inner and outer rings, rolling elements, and cage and for some types shield or sealing. Shields or sealings are not included in the model described below. At first, FE models for individual components are built using I-DEAS software. One of the aims during this modelling process was to access whether some parts could be assumed as rigid bodies. The FE models for outer and inner rings, rolling element are described in this part. Also the results of the numerical modal analysis are presented. The materials of the elements are steel and the properties are shown in Table 4.2.

Table 4.2 : Mechanical properties of the ball bearing components

Modulus of Elasticity (GPa)	**Density** (kg/mm^3)	**Poisson Ratio**
200	7.82e-6	0.29

4.1.1.1. Outer ring

Figure 4.3 shows a 3D FE model of the outer ring. The part is meshed with tetrahedral solid elements. After the meshing procedure modal analysis is performed with I-DEAS commercial software. After the modal analysis, the first eight natural frequencies of the outer ring are listed in Table 1.3. It can be seen that the natural frequencies are very high values which are out of the interested frequency region.

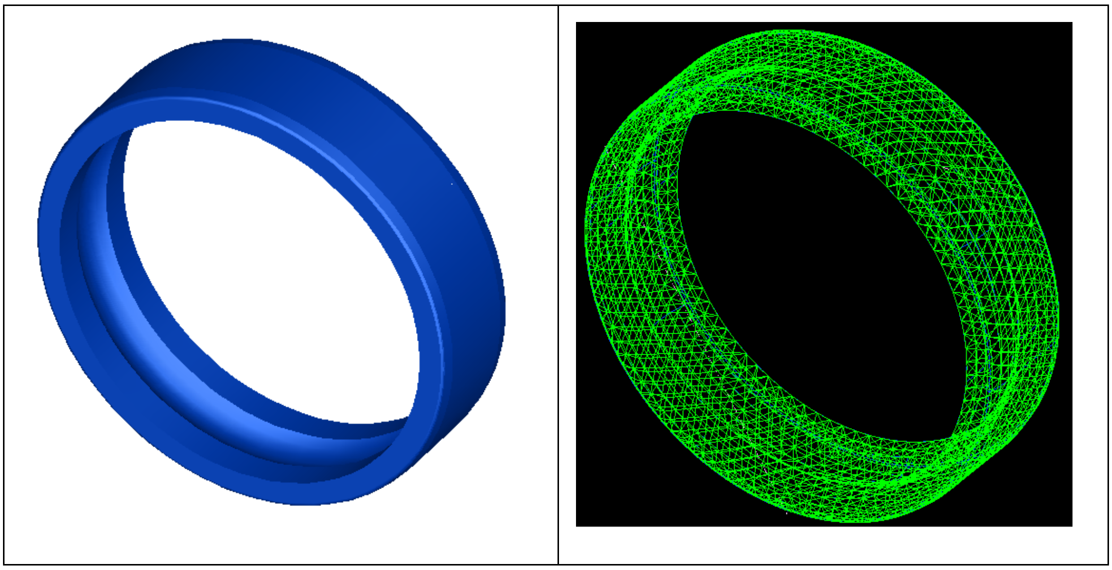

Figure 4.3 :3D and FE model of the outer ring

Table 4.3 : Predicted natural frequencies (from I-DEAS)

Mode #	Frequency (Hz)
1	3540
2	3540
3	6324.77
4	6326.61
5	9846.63
6	9847.05
7	17632.41
8	17633.127

4.1.1.2. Inner ring

The same procedure is also carried out for the inner ring. The 3D and FE models are shown in Figure 4.4. After the modal analysis the first eight natural frequencies of the inner are obtained are and shown in Table 4.4. The natural frequencies of the inner ring are even higher than the outer rings' due to the smaller volume and mass.

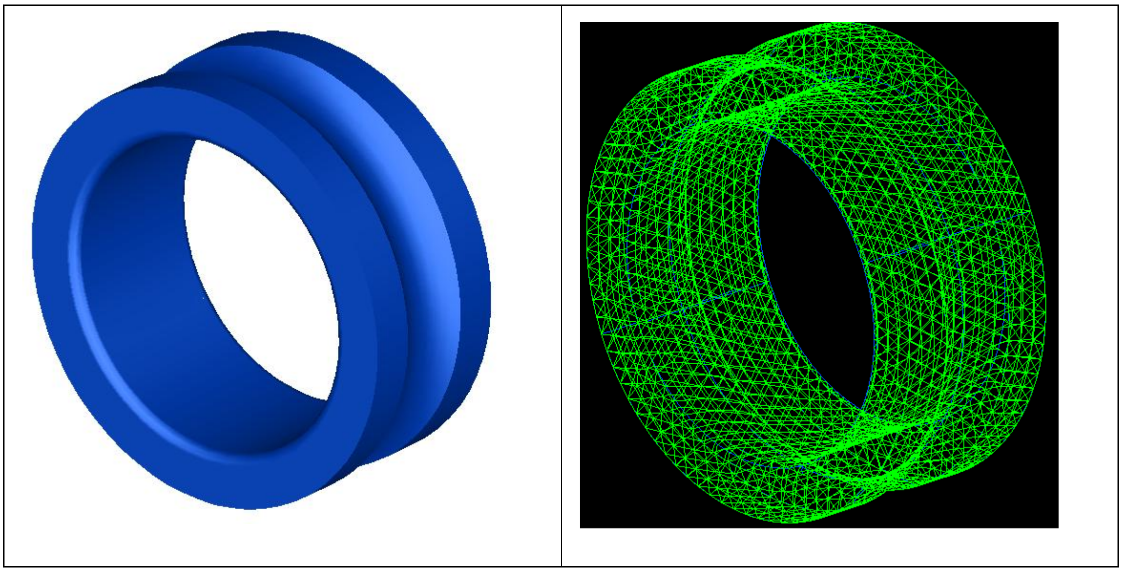

Figure 4.4 :3D and FE model of the inner ring

Table 4.4 : Predicted natural frequencies (from I-DEAS)

Mode #	Frequency (Hz)
1	9693.28
2	9693.28
3	12952.20
4	12952.90
5	26031.81
6	26033.81
7	32395.45
8	32397.18

4.1.1.3. Rolling elements

As mentioned before, rolling elements are connected to each other via cage structure. In this particular bearing studied, the ball bearing has 9 rolling elements. Finite element model is built for one ball and shown in Figure 4.5. The natural frequencies of the ball are listed at Table 4.5. As expected, and as can be seen in the table, the natural frequencies of a ball are really high due to the small geometry and mass properties.

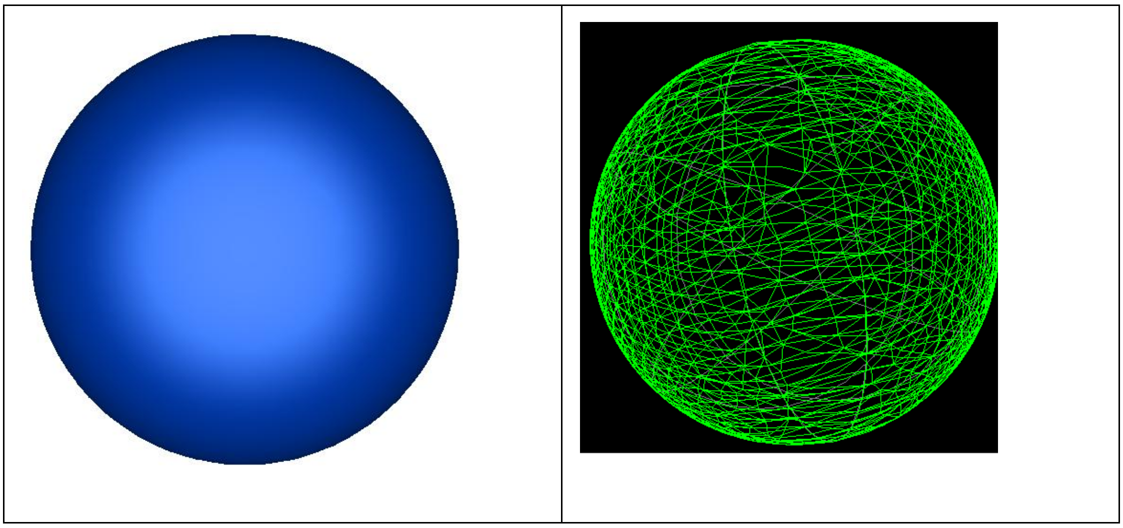

Figure 4.5 : 3D and FE model of the rolling element

Table 4.5 : Predicted natural frequencies (from I-DEAS)

Mode #	Frequency (Hz)
1	267100
2	267100
3	268004
4	268004

4.1.2. ADAMS model of the ball bearing

Ball bearing consisting of rolling elements, inner and outer rings and cage structures can be described as a multi-body system. In order to predict the dynamic behavior, a deep groove ball bearing can be modelled and analyzed as a multi-body system this section explains how a ball bearing is modelled with multi-body system approach by using Msc. ADAMS commercial software.

As seen from the Table 4.3, Table 4.4 and Table 4.5, the components of the ball bearing have very high natural frequencies, due to the high stiffness and small mass values. The standalone natural frequencies of the components are usually out of the frequency range of interest. The frequency range of interest for the rotor-ball bearing system is assumed to be up to 400 Hz. The highest running speed (in a washing machine where this ball bearing is used) is 20 Hz and 400 Hz contains the 20th order of the running speed. As it will be described in detail in chapter 6, this is an acceptable frequency range for monitoring the ball bearing defect frequencies and some resonance behaviour of the system. However, for fault detection issues high frequency analysis may also be required in order to observe significant fault clues. The natural frequencies of the rings can be important while identifying the location of the defect. The rigidity assumption of the ball bearing components can limit the observation of these high frequency vibrations. On the other hand, a flexibility assumption of these components can lead to a severe increase in CPU requirements.

Some simplifying assumptions are made during the development of a ball bearing model using ADAMS software. They are listed below:

The inner and outer rings and rolling elements are assumed to be rigid.

The contact properties between the rings and balls can be determined based on the Hertzian Theory (3.18).

The cage, connecting the balls to each other, is modelled using rigid links.

The balls are positioned equi-pitched around the inner ring and there is no interaction between them.

The damping caused by Elasto-HydroDynamic (EHD) contacts are assumed to be negligible.

In what follows, the process of building up the ball bearing model using ADAMS software is described step by step:

Step 1: Creating the paths

After the 3D models of the ball bearing components (rings and balls) are imported to the ADAMS environment, the paths on which the motion transmission occurs are defined. As shown in Figure 4.6 these paths are defined as curves. The balls and the races get into contact on these paths.

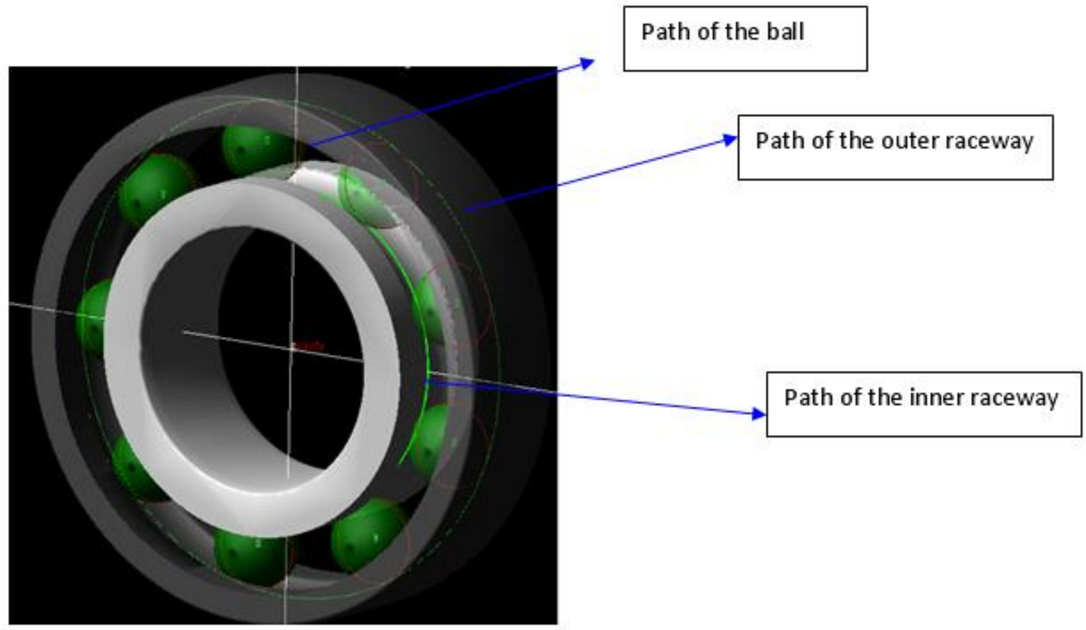

Figure 4.6 : The ball bearing model and the defined paths

Step 2: Definition of the contacts:

When the balls and the rings get in touch with each other, the properties of this contact must be defined correctly in order to ensure realistic dynamic behaviour. In ADAMS software, this kind of contacts can be defined either as solid to solid or curve to curve. Best approximations can be obtained using solid to solid contacts. But, this choice will increase the CPU times sharply and when the structure becomes more complex after the rotor part is added, the CPU requirements may well exceed the resources. Furthermore, it is observed that, the model using curve to curve assumption can give satisfactory results.

A dry friction assumption has been made in order to achieve a rolling motion of balls without slipping on the races. In the model, for the friction between two contacting lubricated steel is taken from the table of ADAMS/View and for dynamic case friction coefficient is assumed as μ_d=0,16 whereas for the static case μ_s=0,23

As mentioned in chapter 3, the contact stiffness is calculated via Hertzian Theory. The values of the geometric features of the ball bearing are listed in Table 4.6.When these values are put into equation (3.18) the contact stiffnesses between balls and rings can be obtained as shown in Table 4.7. Damping at the contacts are defined as

100 N.s/mm. This value is obtained using an iterative approach and viscous damping ratio is 0.214.

Table 4.6 : The geometric values of the observed 6206 bearing

D = 62 mm	R_i = 5.18 mm
d_i = 30 mm	R_o = 5.18 mm
d_m = 46 mm	d = 9.96 mm
R_{in} = 28 mm	C_d = 0.04 mm (C3)
R_{out} = 18mm	R_{re} = 4.98 mm
	α = 0.2 rad

Table 4.7 : The contact stiffness values between contacting components

$Kinner = 9.2201 \times 10^5 \ N/mm$	$Kouter = 9.6880 \times 10^5 \ N/mm$

Step 3: Modelling the cage structure

The balls of the bearing are connected to each other via rigid connectors. This structure represents the cage of the ball bearing. In order to avoid the hyperstatic condition, the first and the last balls are not directly connected to each other. (Figure 4.7)

Step 4: Defining the constraints and the motion

After the paths and contacts are defined, the kinematical relationship between the parts has to be specified. The outer ring is fixed to the ground. Balls, outer ring and inner ring are constrained to be in the same plane by using planar joints. Inner ring is hold by balls and it is not connected to ground. The joint between the shaft and the inner ring will be described when the rotor model is assembled. Motion is defined on the inner ring. For example, it is accelerated to 1200 rpm in 10 seconds. The completed ball-bearing model is shown in Figure 4.7. The angular velocities of the balls, cage and inner ring are shown in Figure 4.8. It can be seen that the relationship between the angular velocities of inner ring, cage and ball is as described in chapter 3. This confirms that the ball bearing model is functioning properly and satisfies the kinematic behaviour of the real ball bearing.

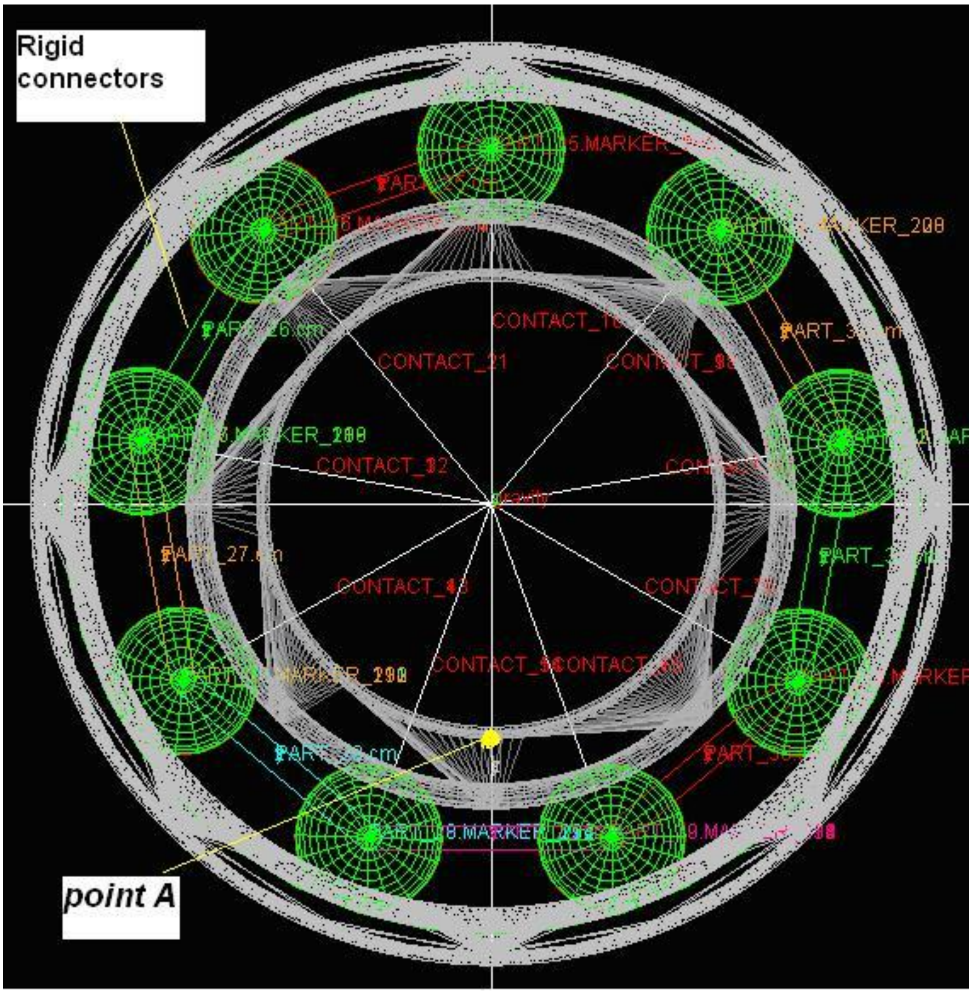

Figure 4.7 : The ADAMS model of the ball bearing

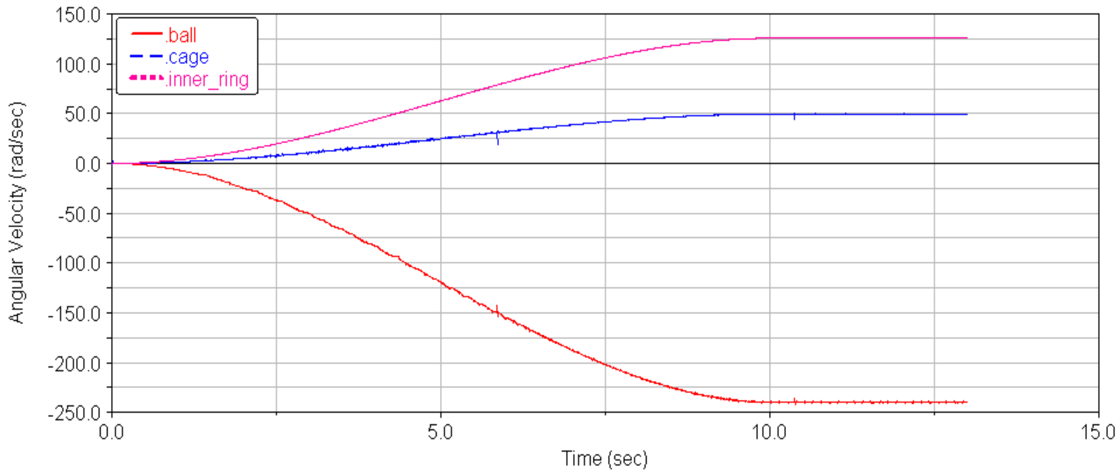

Figure 4.8 : The angular velocities of the ball-bearing components

The acceleration of the point A shown in Figure 4.7 on the inner ring along the vertical direction is obtained from ADAMS simulations. A Fast Fourier Transform (FFT) is applied to the time-domain data and the amplitude spectrum is obtained when the system is at steady state and the rotational speed is 1200 rpm. As seen in Figure 4.9 the rotation speed at 20 Hz, Ball Passing Frequency (BPF) at 71 Hz and its harmonics at 142, 213... Hz are visible. Also there are significant peaks at sidebands of the BPF and its harmonics. The Fundamental Train Frequency (FTF) of this system is 7.72 Hz. The sidebands of the BPF are BPF ±nxFTF. The amplitudes are very high because they are not vibrations; they are the motion of a point on inner ring around the global vertical axis.

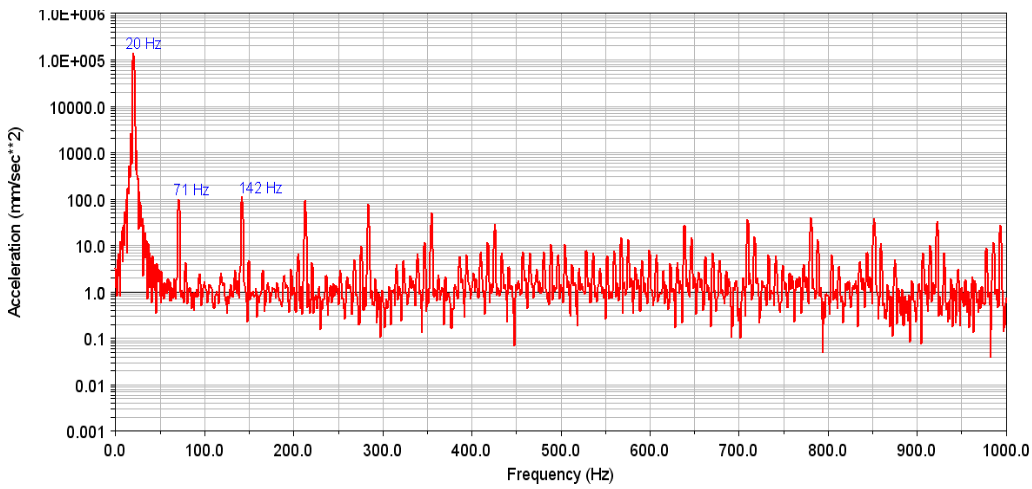

Figure 4.9 : The Amplitude spectrum of the standalone ball bearing model

4.2. Modeling the rotor part

4.2.1. Shaft

After the ball bearing model is created, the rotor part is built as an assembly of a shaft and a disc at one the end of the shaft. The shaft and its dimensions are shown in Figure 4.10. The diameter of the shaft is 30 mm, which is equal to the inner diameter of the ball bearing. There is a rabbet with 35 mm diameter. This is necessary for assembling the ball bearing. At the end of the shaft there is a key geometry which allows the disc to be assembled.

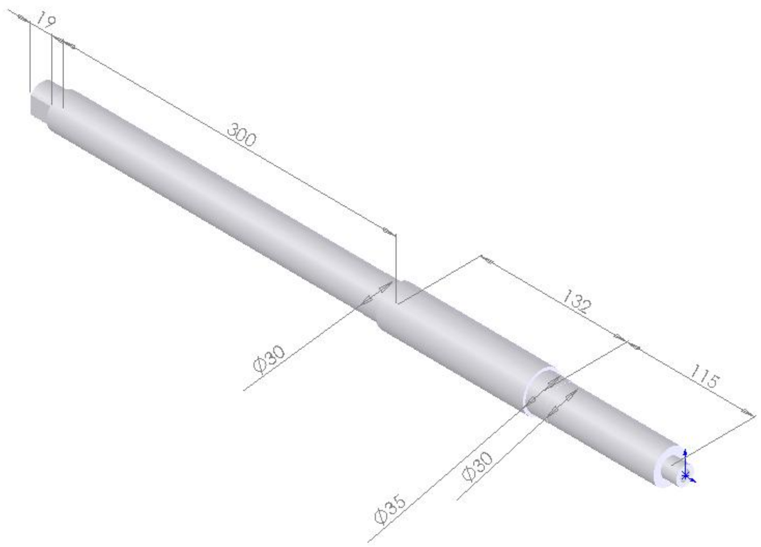

Figure 4.10 : The CAD model of the shaft

As far as the shaft is concerned, two cases are considered. In the first case, it is assumed that the shaft is rigid. In the second case, however, a Finite Element (FE) model of the shaft is developed in order to include its flexibility in the model. Flexible shaft model consists of three dimensional beam elements. The FE model of the shaft is shown in Figure 4.11. Once the model is built, numerical modal analyses are carried out; also numerical FRFs are obtained from I-DEAS commercial software. The structure is excited and acceleration data is collected from the direction of excitation. Moreover experimental FRFs are taken from the real shaft structure under free-free conditions. The comparison of these results is shown in Figure 4.12. The good correlation between the numerical and experimental results is clearly seen. Especially for the first three natural frequencies, the predictions are in good agreement with the measurements. Also, there is a natural frequency corresponding to torsional mode at 2992 Hz. This torsional mode is seen in the experimental model with a very small peak, due to the impact hammer excitation with a very small tangential component. This natural frequency is also determined in the numerical model, although the visualisation of the mode shape is not good due to the beam model.

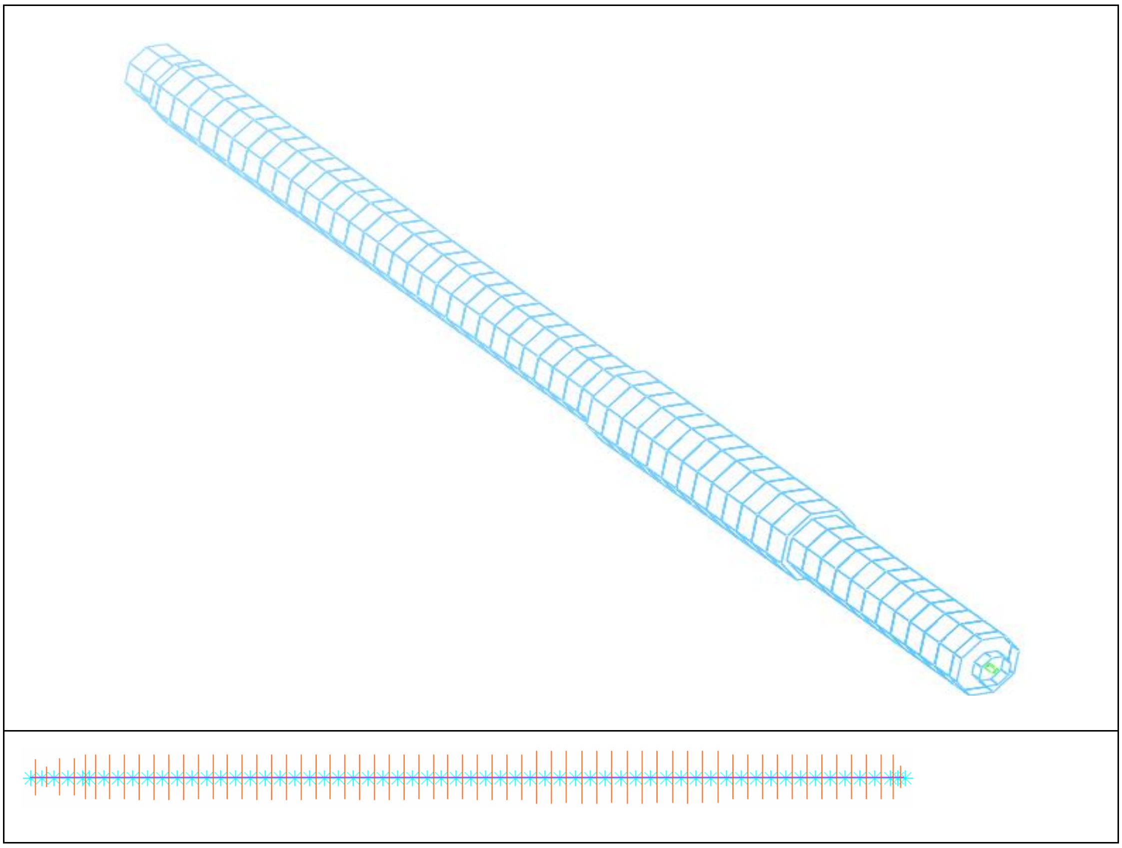

Figure 4.11 : The FE model of the shaft with beam elements

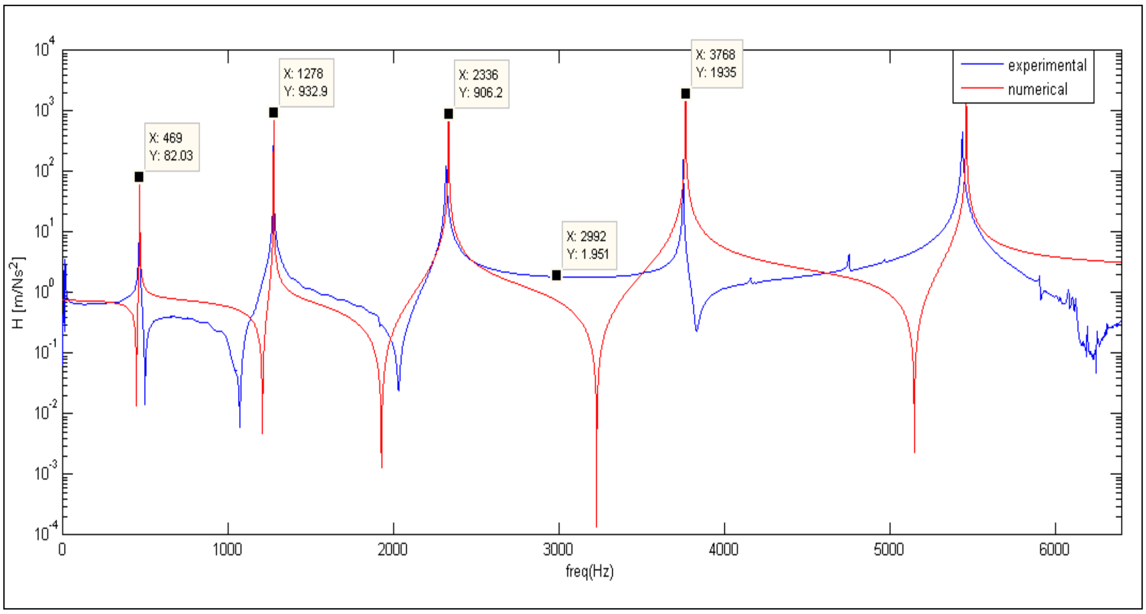

Figure 4.12 : Comparison of the numerical and experimental FRFs

The first three mode shapes obtained from both numerical modal analyses and experimental modal analyses are compared in Figure 4.13, Figure 4.14 and Figure 4.15.

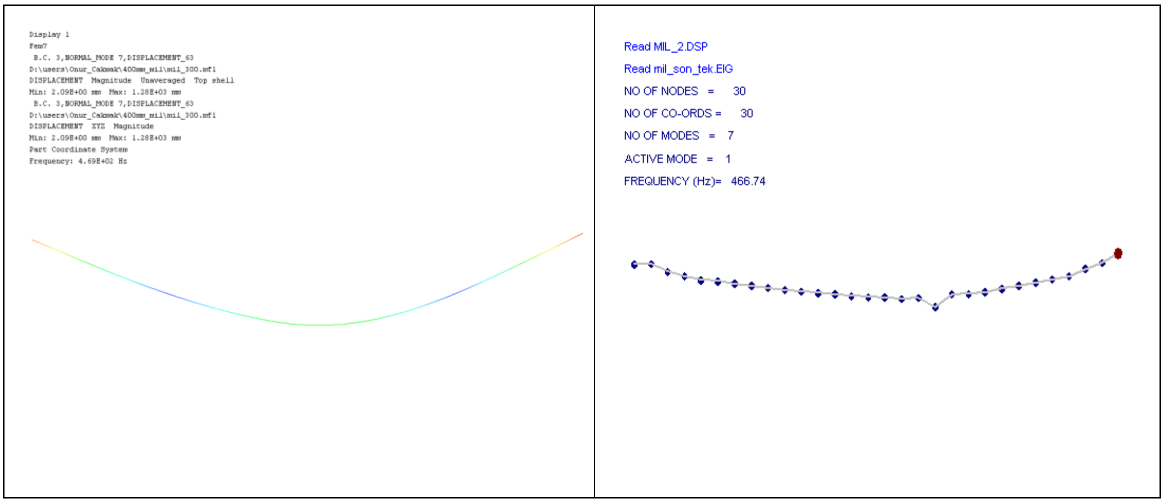

Figure 4.13 : Mode shape #1

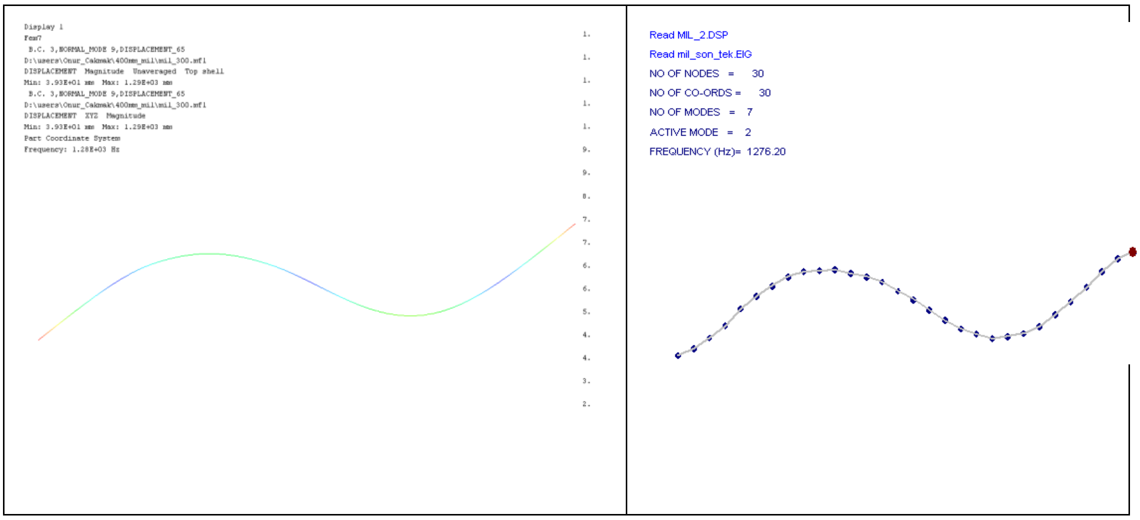

Figure 4.14 : Mode shape #2

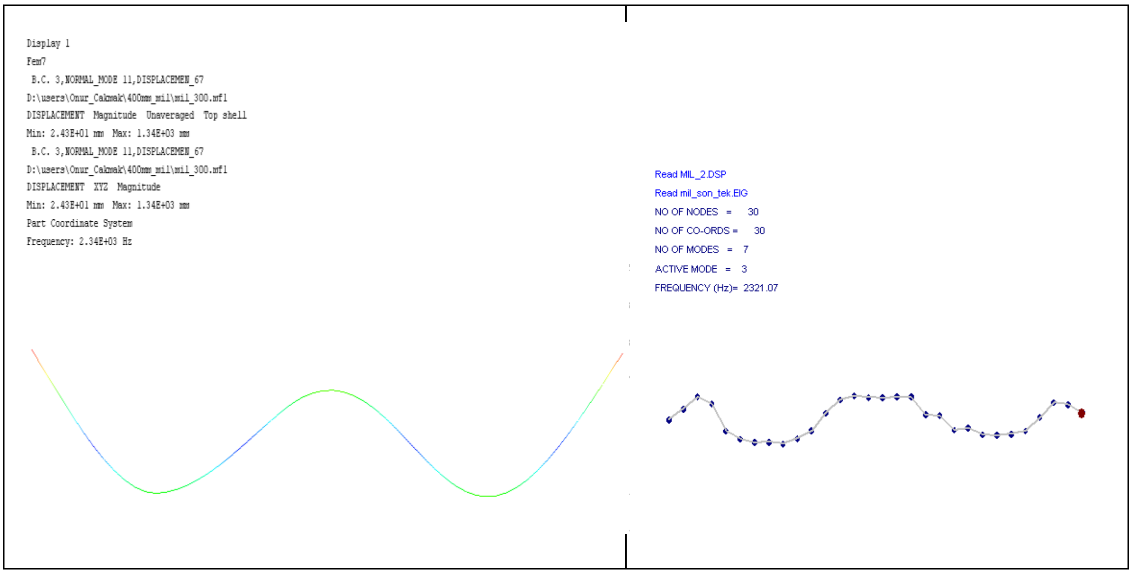

Figure 4.15 : Mode Shape #3

At the first mode shape the bending can be clearly seen at both numerical and experimental results. The numerical mode shape fits with the experimental mode shape for the second mode in a perfect manner. For the third mode shape there appears a slight difference between the mode shapes. This is possibly due to the experimental errors resulting from moving accelerometer mass. However, these results are satisfactory for correlation purposes.

4.2.2. Disc

The 3D geometry and the dimensions of the disc are shown in Figure 4.16. As can be seen, there are 12 holes with 12 mm diameter, allowing the addition of unbalance masses into the model. The centers of these holes are 100 mm away from the centre of the disc itself. Also shown is the key geometry at the center, which is same with the one on the shaft.

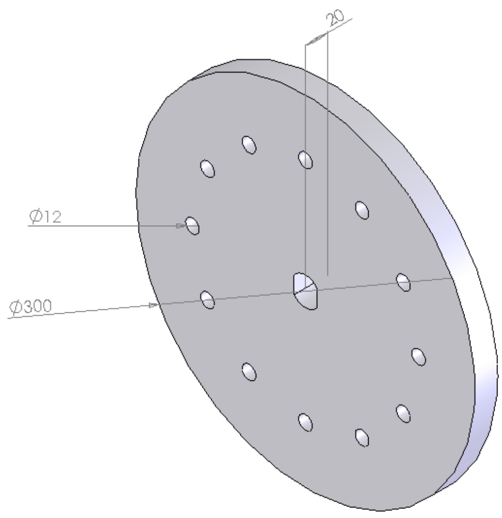

Figure 4.16 : The CAD model of the disc

At the numerical model the disc is assumed to be rigid. The mass and inertia properties of the disc is calculated and implemented in the model.

The model of the assembled rotor is shown in Figure 4.17

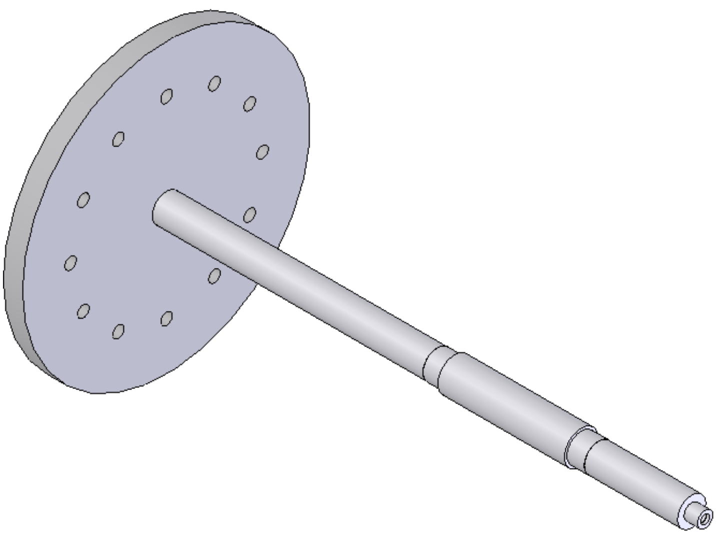

Figure 4.17 : The CAD model of the shaft-disc assembly

4.3. Joining the rotor and the bearing models

While modelling the rotor-bearing systems several assumptions are usually made [19]. The bearing part can be modelled using primitive joints. These joints are defined with constraints on nodes. In many practical applications about rotor-dynamics, there is a general assumption that spherical or cylindrical joints can be used to model roller bearings especially when they are fixed to the ground. During this study the accuracy of these assumptions are investigated.

In this section, first, the models with primitive joints are introduced. In those models, the shaft is assumed to be flexible and usually its FE model is used. Then, the model with flexible shaft and ball bearing model is introduced. The improvement process of this new model is described. The comparison of the FRF results taken from both flexible models and experimental model is also given in order to assess the accuracy of the models developed.

4.3.1. The models with primitive joints

For those models using primitive joints, shaft is assumed to be flexible and usually its FE model is used. The disc is assumed to be rigid and it is attached to the shaft with an interface node. The ball bearings and housings are modelled with cylindrical and spherical joints. The freedom properties of these joints are listed in Table 4.8 X and Y indicates the radial directions whereas Z indicates the axial direction.

Table 4.8 : The freedoms of primitive joist

	Cylindrical	Spherical
Translation X	Fixed	Fixed
Translation Y	Fixed	Fixed
Translation Z	Free	Fixed
Rotation X	Fixed	Free
Rotation Y	Fixed	Free
Rotation Z	Free	Free

The model with spherical joint is shown in Figure 4.18.

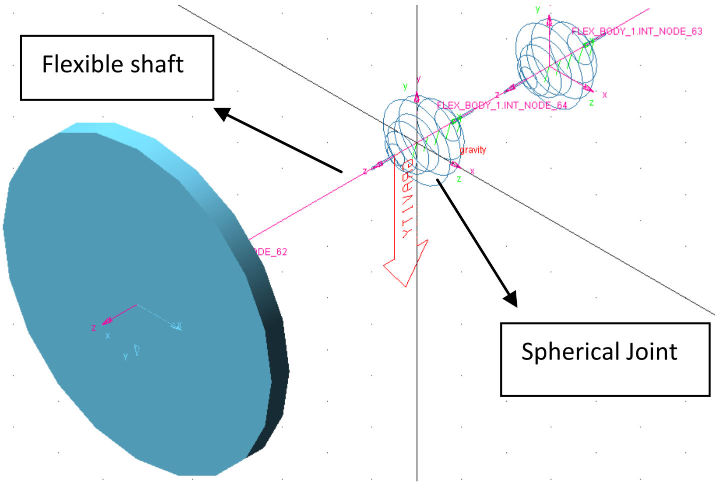

Figure 4.18 : Primitive model with spherical joints instead of ball bearings

After these primitive models are built, numerical modal analyses are performed by using Msc. ADAMS/Vibration tool. The natural frequencies obtained from both numerical models and experimental model are shown in Table 4.9. The details about the mentioned experimental model will be described in Chapter 4. The results obtained from experimental model are included here in order to demonstrate the accuracy of the numerical models.

Table 4.9 : Measured and predicted natural frequencies using primitive joints

Mode #	Model with cylindrical joint	Model with spherical joint	Experimental model
1 (First bending)	41.59	37.09	27.21
2 (First bending)	41.59	37.09	31.35
3 (torsion)	45.59	45.59	45.21

4 (Second bending)	204.5	196.1	169.73
5 (Second bending)	204.5	196.1	174.75

From this table it can be inferred that, the models with primitive joints cannot yield satisfactory results when the first two modes are considered. The first two natural frequencies correspond to the bending modes. As shown in Table 4.8 cylindrical joint does not allow translational or rotational motion at radial directions, this makes the system “over-constrained” when compared with reality. In reality, although it is very limited, ball bearings also allow rotation around the radial directions in addition to axial direction. Spherical joint, however, permits these rotational motions and as a result it yields results better than those of cylindrical joint. However, the results are still not satisfactory. The third natural frequency in Table 1-12 corresponds to the torsion mode. There is a good correlation between the results of the models and the experimental data for this mode. The natural frequency for the torsion mode is directly related to the elastic and the polar inertia properties of the rotor part and the bearing model has no influence on it. Therefore, predicted and measured the natural frequency for this mode correlate very well. . For the 4^{th} and 5^{th} natural frequencies, the results of the numerical models are not acceptable either. These natural frequencies are for the second bending modes.

Another important point about the experimental results presented in Table 4.10.is the difference between the natural frequencies for the bending modes in horizontal and vertical directions. According to the theory, when the shaft and disc are assumed to be homogeneous and symmetric in both directions, the bending natural frequencies in those directions should be the same. However, for the real system, the rotor part is connected to the ground with ball bearings and housings. These housings have different stiffness and damping characteristics in different directions. Therefore, the rotor-baring model has to be improved in order to include this behaviour. In the next section, the translational and rotational stiffnesses of ball bearings, housing and belt are taken into account in the improved model.

4.3.2. The model of the system with the developed model of the ball-bearing

After the ball bearing model and the validated FE model of the rotor part are built, they are assembled using the Msc. ADAMS/View environment. As discussed earlier in the previous section, the results obtained from those models based on primitive joints are not satisfactory; hence an improved model of the rotor-ball bearing system is required.

The FE model of the shaft is also used here. Interface nodes with superelement features are defined in the FE model at I-DEAS environment and ".mnf" files are created. The rigid disc and the ball-bearing model are attached to the flexible shaft at these interface nodes. The contact definition between the shaft and the inner ring of the ball bearing is an important criteria. As mentioned before, although very limited, deep groove ball bearings also have some rotational freedoms around radial axes. This freedom can have significant influence on the natural frequencies and dynamic behaviour of the system. In the proposed model, these freedoms are defined by using a so-called bushing element with rotational stiffness between the inner rings and the shaft. The combined model of the rotor-ball bearing system is shown in Figure 4.19. The outer rings of the ball bearings are fixed to the ground and the stiffness and damping of the housings are not included in the model.

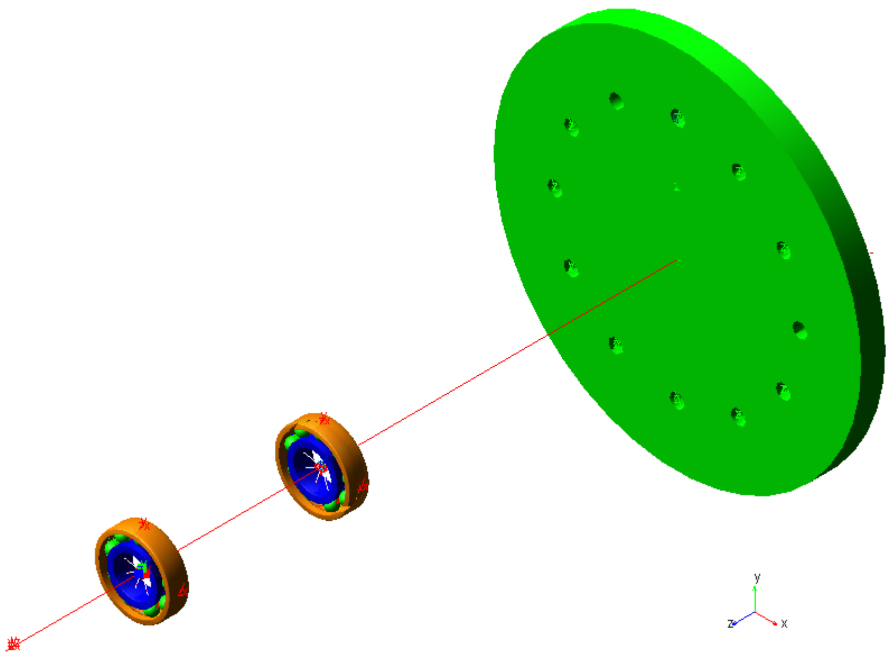

Figure 4.19 : ADAMS model of the combined rotor-ball bearing system

The natural frequencies predicted using this numerical model are listed in Table 4.10. The results are also compared with the experimental results.

Table 4.10 : First five natural frequencies of the numerical model with ball bearing and experimental model

Mode #	Numerical model	Experimental model
1	33.27	27.21
2	34.21	31.35
3	44.54	45.21
4	183.32	169.73
5	185.21	174.75

From Table 4.10, it can be inferred that the numerical results obtained from this model are much better when they are compared with those of the primitive models. The natural frequencies corresponding to 1st and 2nd bending modes are still not close enough to the experimental results. However, it can be seen that there is a small difference between the bending modes at different directions as in the experimental results. This is due to diametral clearance. As mentioned in Chapter 3, at static conditions a load zone occurs along the direction of the gravity, and due to the this load zone the contact characteristics at different directions can be different from each other. However this is not the main reason for the differences in natural frequencies for bending modes in orthogonal directions. In order to model this behaviour properly the difference in the flexibility of the housings in orthogonal directions must be taken into account.

The stiffness and damping properties of the housing in different directions will be investigated after the experimental studies. The experimental procedure is described in Chapter 5. In the light of these experimental results, the rotor-baring model will be improved further. The dynamic analysis will be performed with this improved and validated numerical model and the gyroscopic effects on the system's dynamic behaviour will also be represented in Chapter 6.

5. TEST RIG DEVELOPMENT FOR A ROTOR-BALL BEARING SYSTEM AND MEASUREMENTS

In order to validate the rotor-ball bearing model developed in the previous chapter, a test rig is designed and developed. The experimental results are also used for further improvements of the numerical model. The test rig comprises a shaft, a disc and two deep groove ball bearings supporting the rotor. The CAD of the test rig designed is shown in Figure 5.1.

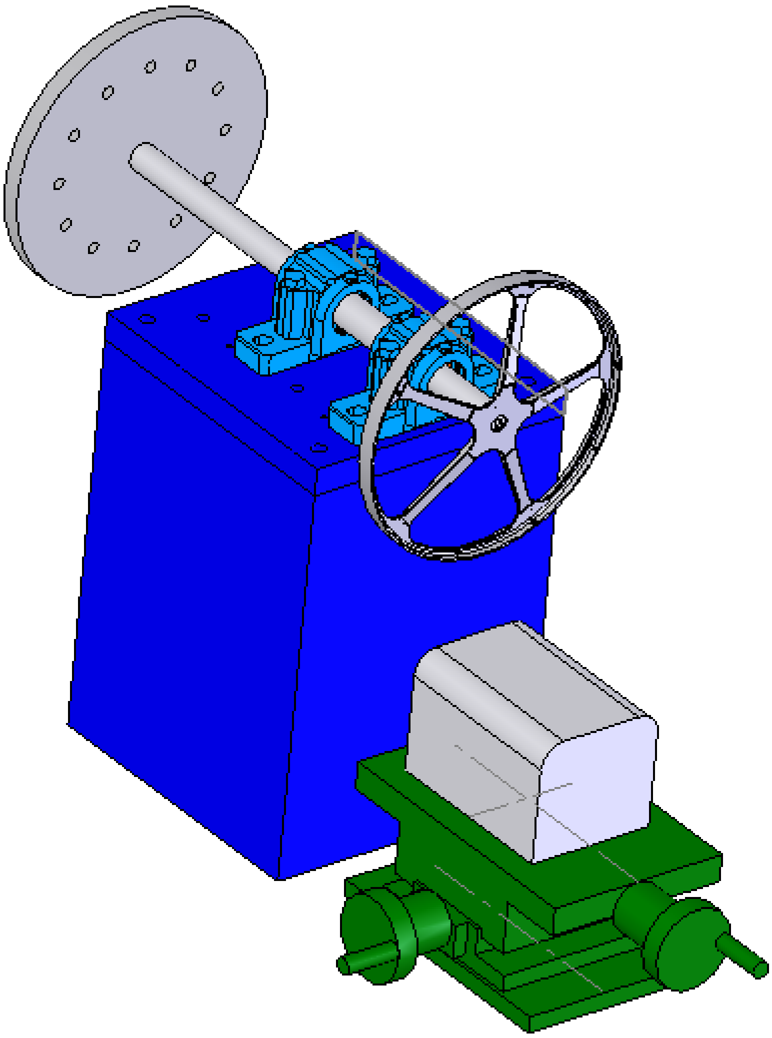

Figure 5.1: Isometric view of the 3D model of the test rig

As can be seen in Figure 5.1 the ball bearings are mounted on a heavy block. Further details including the dimensions and designation of these housings are given in Figure 5.2.

Split plummer block housings, SNL series for bearings with a cylindrical bore, with standard seals

Shaft		Appropriate bearings (basic designation)				Housing Principal dimensions				Mass	Designations
		Self-aligning ball bearings		Spherical roller bearings							
d_a	d_b					A	L	H	H_1		
mm		-				mm				kg	
30	35	1206	2206	-	22206	77	185	89	50	1,90	**SNL 206-305**

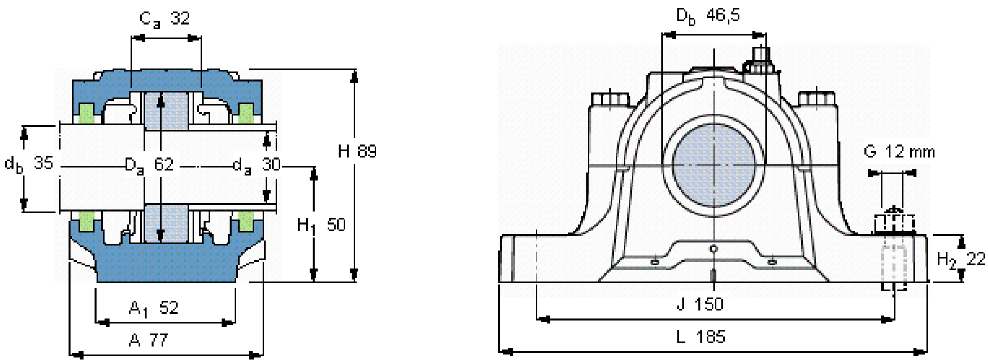

Figure 5.2 : Dimensions of the SKF SNL 206-305 housing [21]

The tolerances between the shaft and the bearings are chosen according to loose fit criteria [22]. This type of fitting criteria is also used induring the construction of washing machines.

The disc is described during the development of the numerical model in chapter 4. A matching key structure is designed at the centre of the disc for mounting the disc on the shaft. Also, in order to avoid the tilting of the disc a nut is used for locking the disc to the shaft. A heavy block, about 400 kg mass, is manufactured as a bench structure in order to provide a very stiff platform for the rotor-bearing system. This heavy block is filled with concrete and the top surface is grinded in order to obtain a smooth surface. The heavy block stands on soft supports.

The system is driven by an AC motor and the power transmission is provided by a belt-pulley mechanism. The shaft of the AC motor has 27.3 mm diameter whereas the pulley has 300 mm diameter. As a result, the transmission ratio between the motor and the system is about 11.0. AC motor is decoupled from the whole system and fixed to the ground in order to minimize its effects on the overall vibration. A coaster mechanism is designed a manufactured in order to move the motor in all directions. Motor can be positioned precisely so as to calibrate the belt tension. This mechanism is fixed to the ground.

A picture of the assembled test rig is shown in Figure 5.3.

Figure 5.3 : The test rig

The test rig is designed in such a way that it is quite easy to change some components in the assembly. For example, a shaft with a different length can be used and the ball bearings can be replaced with others with different clearance values. Unbalance masses can easily be added to the structure via the holes on the disc.

5.1. FRF analysis

In order to validate the numerical model and to improve it further, various measurements are carried out. For the static case (non rotating case), frequency response functions of the whole system and some individual components are measured. The equipments used during this experimental process are shown in Figure 5.4. The accelerometer used is CCLD type.

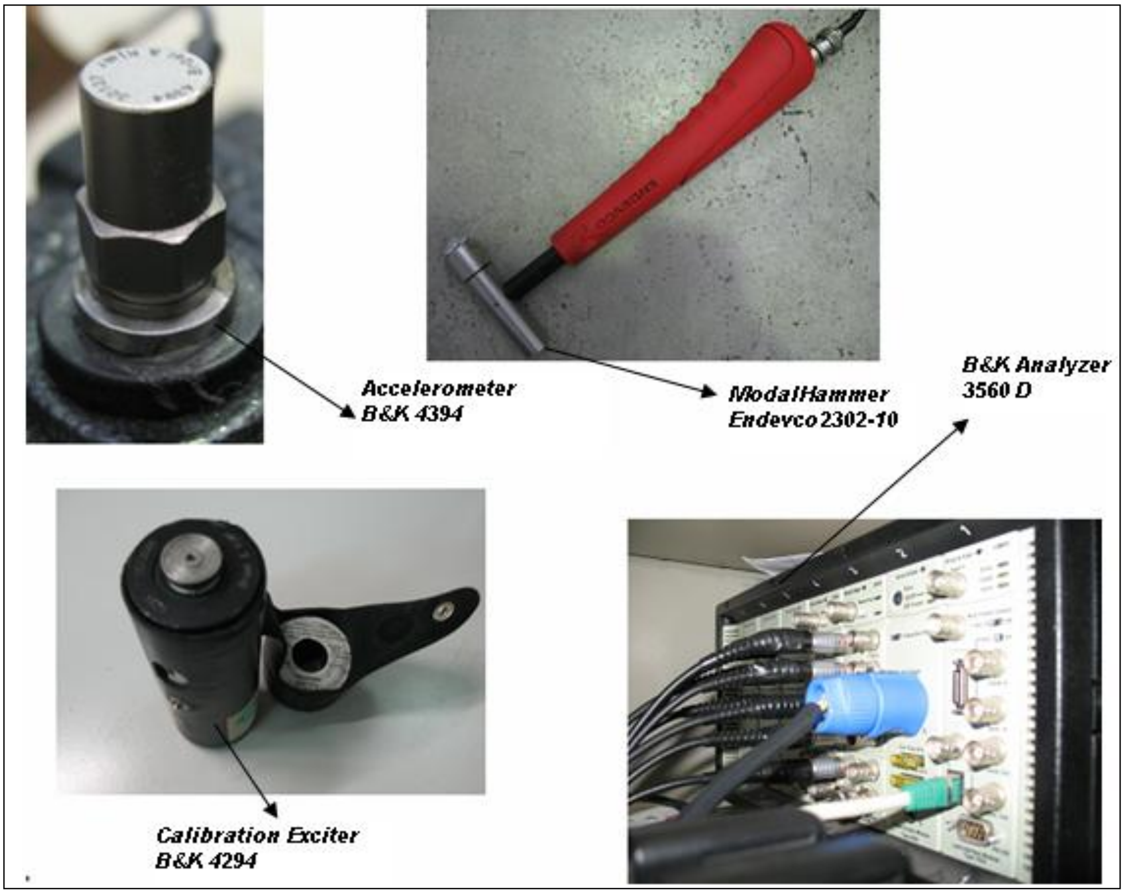

Figure 5.4 : Hardware used during FRF measurements

The structure is excited using a modal impact hammer and charge type accelerometers are used to measure the responses. An analyzer (B&K 3560) with proper signal conditioning hardware is used. The system is excited in both radial directions as shown in Figure 5.5. The response of the system is collected in the direction of excitation. The excitation point is stationary whereas the accelerometer location is changed during each FRF measurement.

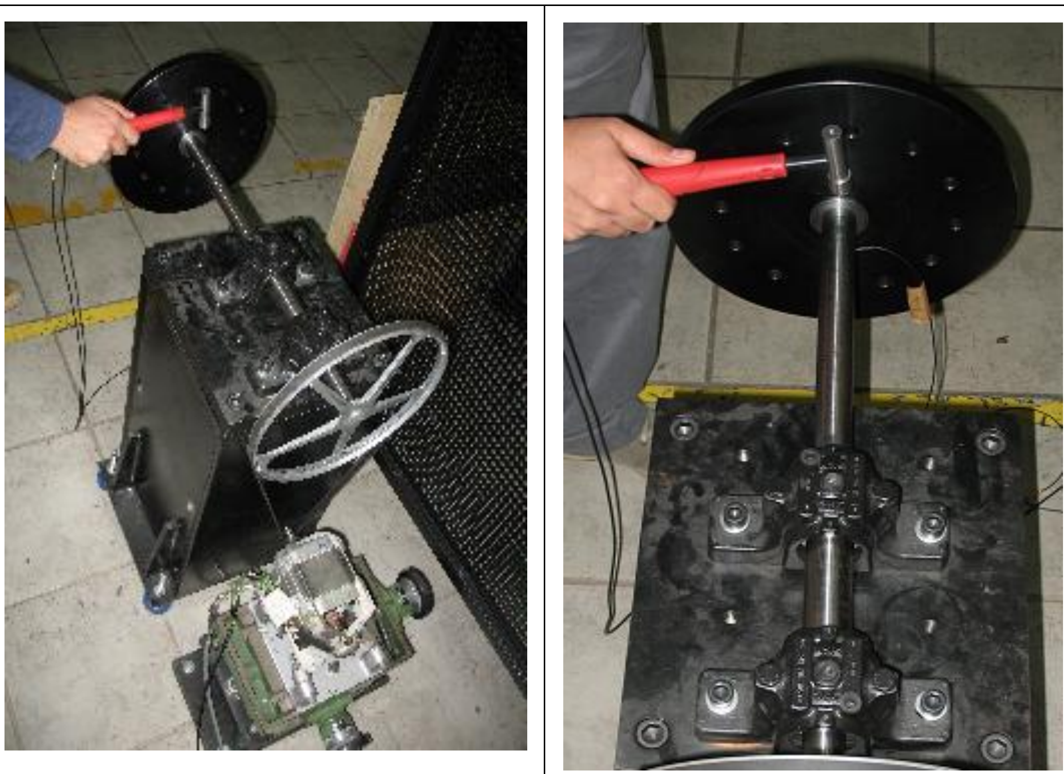

Figure 5.5 : The use of hammer excitation during FRF measurements

Two sample FRFs of the system are shown in Figures 1.6 and 1.7. The FRF in Figures 1.6 is obtained when the excitation is applied in vertical direction and response is measured in vertical direction. The FRF in Figures 1.7, on the other hand, is obtained when both excitation and response directions are in horizontal direction.

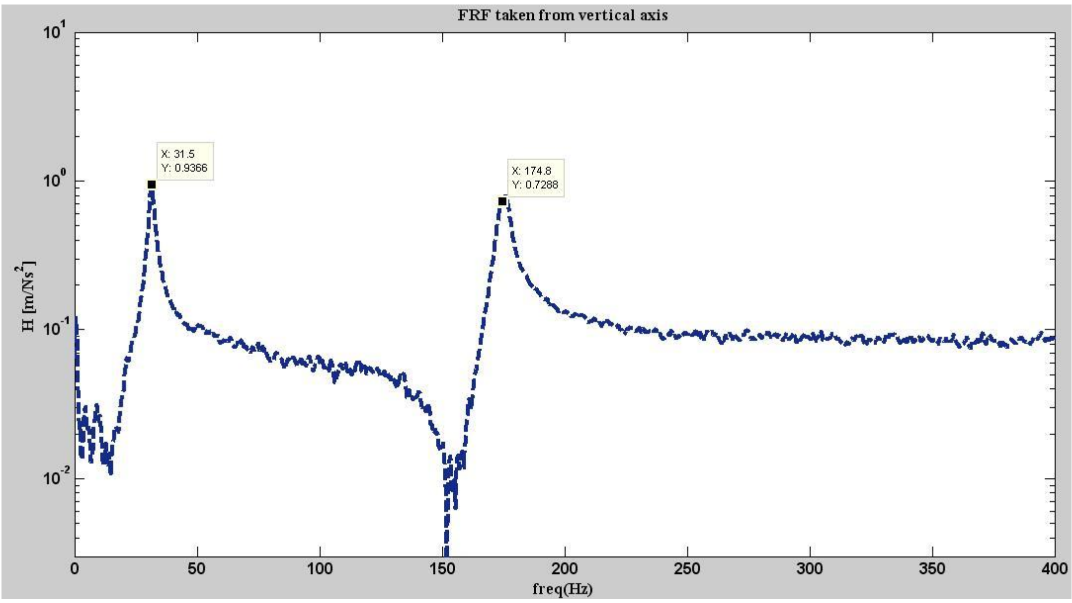

Figure 5.6 : FRF of the test rig for an impact in vertical direction

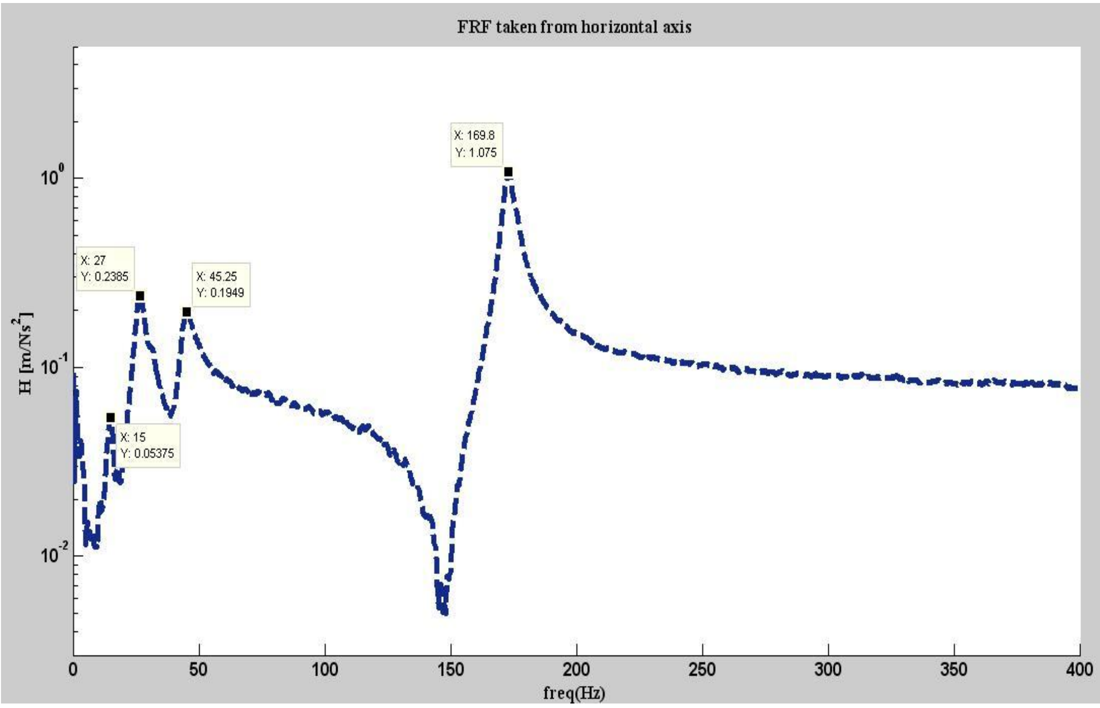

Figure 5.7 : FRF of the test rig for an impact in horizontal direction

The experimental FRFs in Figure 5.6 and Figure 5.7 show several peaks indicating natural frequencies.The peak at 15 Hz in Figure 5.7 is the natural frequency corresponding to the mode shape that can be described as rocking of the whole system as a rigid body on elastic supports of the heavy bench. Another peak at 45.25

Hz in measured FRF in horizontal direction corresponds to the torsional mode of the structure. The torsional mode appears here due to the impact hammer excitation having tangential component during the measurement. This causes torsional response of the system and appears as a peak in the measured FRF. Other peaks are corresponding to natural frequencies for the 1^{st} and 2^{nd} bending modes of the rotor. The mode shapes at those frequencies are obtained using the modal analyses software ICATS. The experimental mode shapes will be presented in Chapter 6 and they are compared there with the numerical mode shapes obtained from numerical models.

The FRFs measured in different directions are somewhat different from each other when the 1st and 2nd bending modes are considered. As discussed in Chapter 3, this is a result of different stiffness characteristics of the housings in different directions. Accurate modelling of the system flexibility in horizontal and vertical directions can be a bit difficult if purely theoretical approach is followed. However, experimental results can be utilized in order to model the system behaviour in horizontal and vertical directions. This is precisely the approach followed here, i.e., the stiffnesses of the housings' are determined in the light of the experimental data and implemented in the model.

5.2. Determination of the stiffness coefficients of the housings

In order to determine the stiffness coefficients of the housings the FRFs are measured along horizontal and vertical and directions as shown in Figure 1.8. Impact hammer is used to apply and impact excitation and the vibration response is collected in terms of acceleration. After obtaining the FRF of the system in terms of "Inertance", this function is converted into "Receptance" which can be described as the displacement response to the force. This conversion is easily done with the help of MODESH toolbox of the ICATS modal analyses software. The relationship between receptance and inertance are described in Table 5.1 [23], where α indicates accelaration, v is velocity χ is dispacement, f is force and ω is frequency.

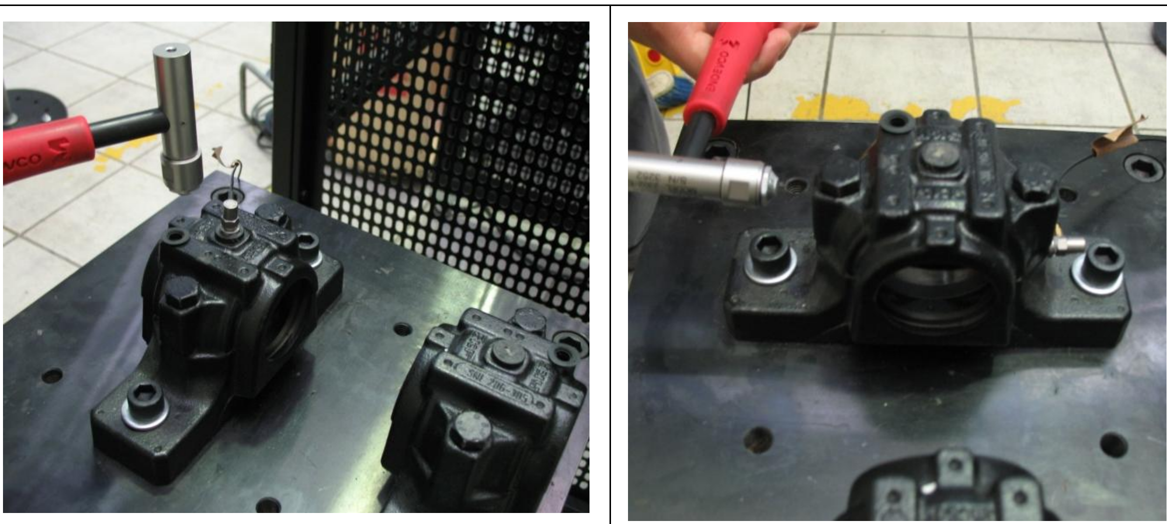

Figure 5.8 : Measurement of housing stiffness

Table 5.1 : The Forms of FRF

Receptance	Mobility	Inertance
$\alpha(\omega) = \dfrac{X}{F}$	$Y(\omega) = \dfrac{V}{F} = i\omega\alpha(\omega)$	$A(\omega) = \dfrac{A}{F} = \omega^2\alpha(\omega)$

When the FRF is plotted in terms of receptance the low-frequency straigt line [23] region can be considered as the static region. The stiffness of the structure through the excitation direction can be estimated from the values at that region. The stiffness of the housings can be determined as $1/\alpha(\omega)$ when ω approaches to zero. The FRFs taken from the structure are shown in Figure 5.9, Figure 5.10, Figure 5.11 and Figure 5.12.

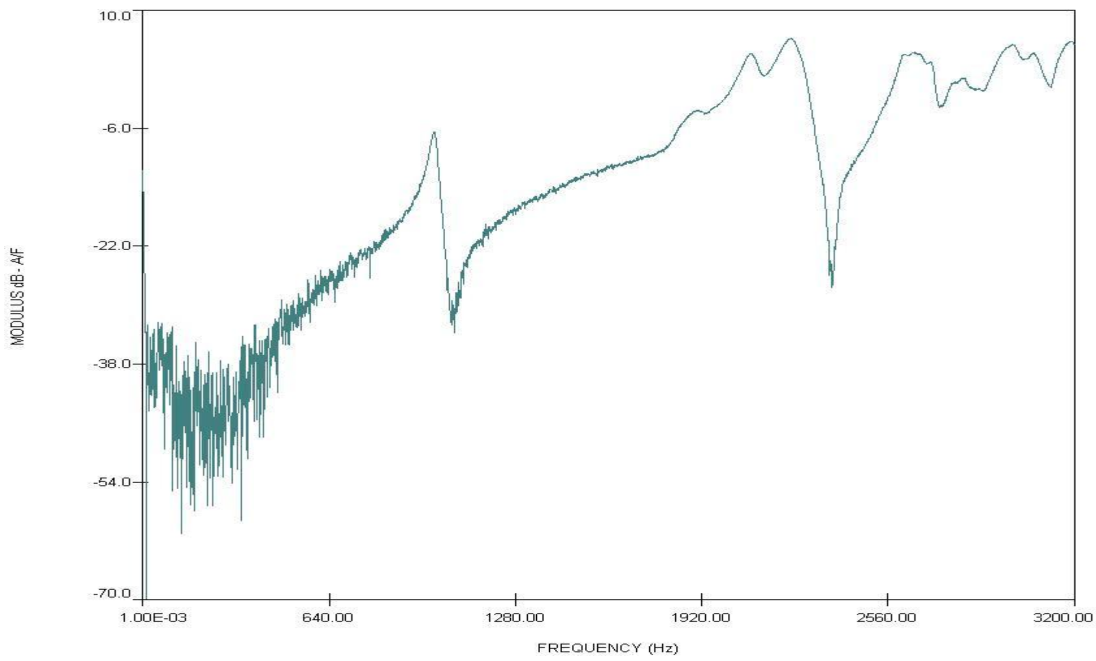

Figure 5.9 : Inertance of the housing in vertical direction

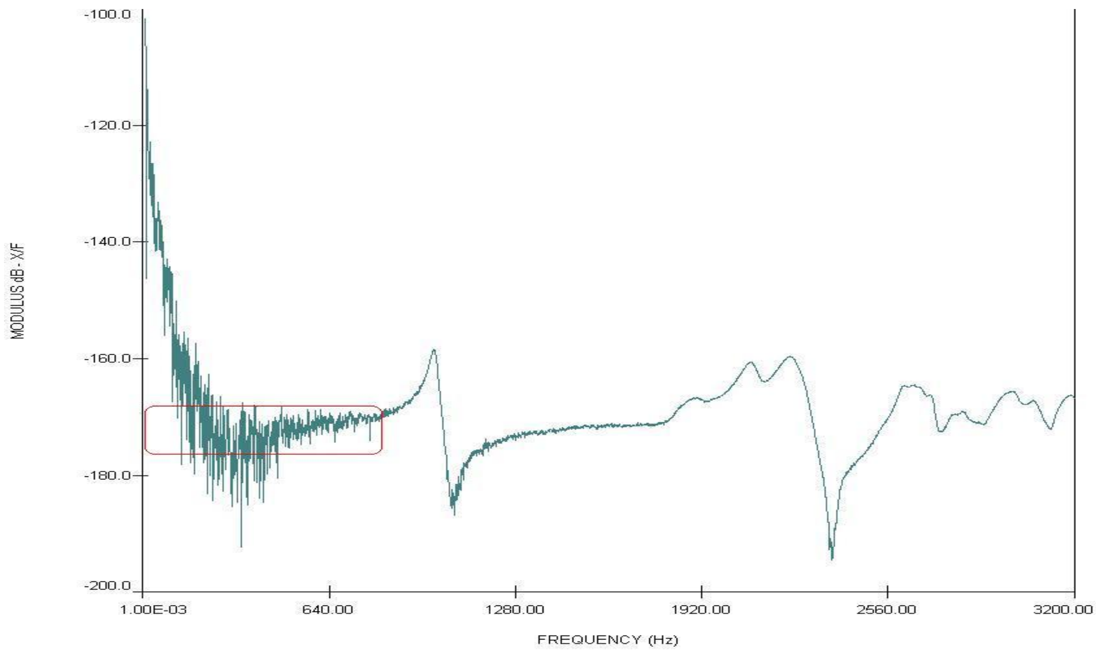

Figure 5.10 : Receptance of the housing in horizontal direction

As seen in Figure 5.10, the housing has a natural frequency at 1080 Hz in the vertical direction. The region on the left side of this peak is the area that is used for stiffness determination. As can be seen, when the frequency approaches to 0 Hz the response of the system is increasing. This can be related to the rigid body motion of the heavy block.

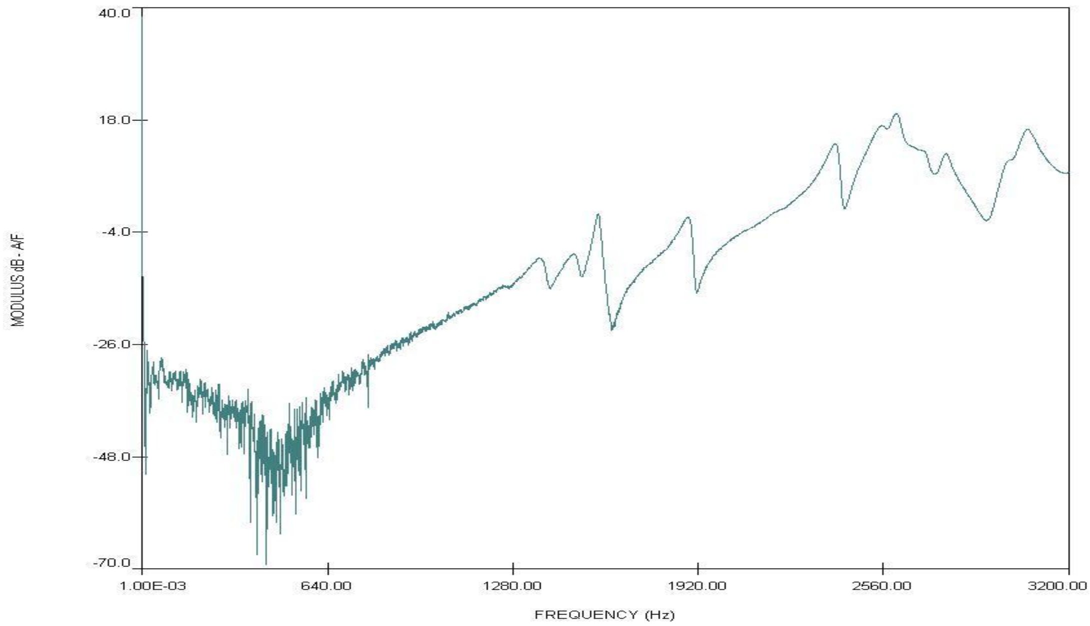

Figure 5.11 : Inertance of the housing in horizontal direction

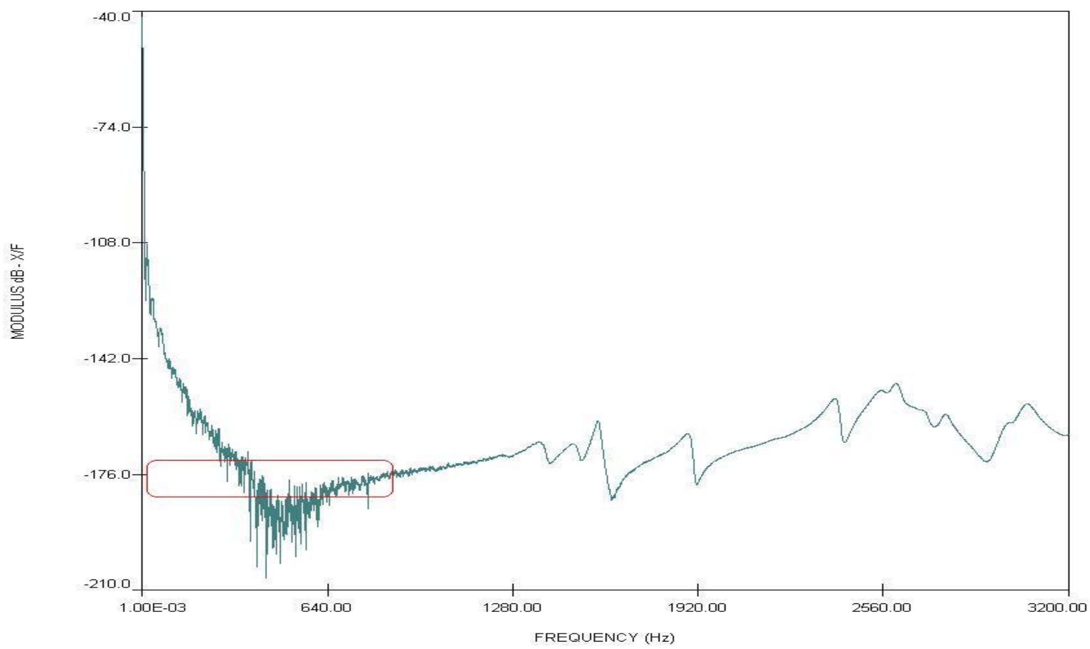

Figure 5.12 : Receptance of the housing in horizontal direction

As seen in Figure 5.12, the FRF of the housing in horizontal direction have several peaks around 1372 Hz, 1501 Hz and 1582 Hz. The measured FRF has similar characteristics with the one in the vertical direction around 0 Hz. As highlighted in FRF curves, the regions where the FRF curves become relatively straight are used for stiffness estimations. It must be noted, however, that accuracy of this estimation is not very high due to noisy data and also due to there being a rigid body mode of the whole system (whole system on soft supports). As a result, the stiffness values calculated from these plots provide a range that stiffness values can fluctuate. The precise stiffness values used in the numerical model are therefore determined within this range after some numerical trials.

5.3. Order Tracking Analysis

In order to determine the vibration behaviour of the test rig at different running speeds, the system is investigated using an order tracking analysis procedure. Information about the rotational speed is obtained by using the signal from an existing tacho probe on the AC motor (Figure 5.14) and the belt ratio. The accuracy of this tacho signal is verified using another laser tachometer tracing the rotation of the disc directly.

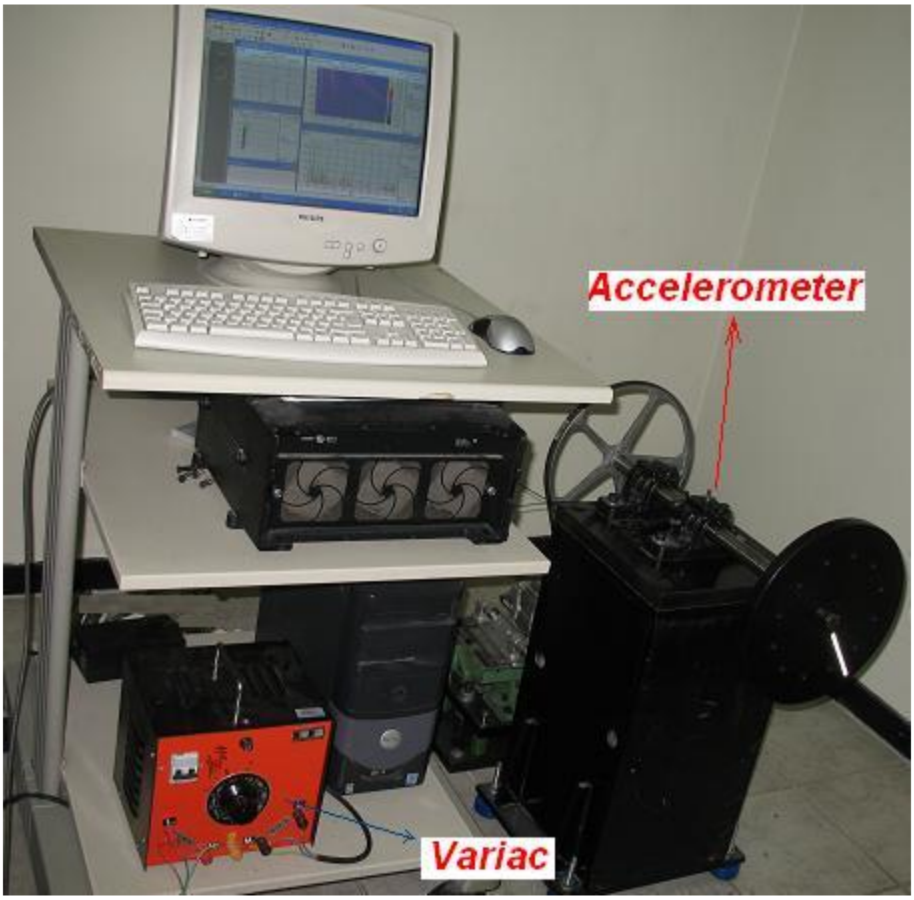

Figure 5.13 : The measurement setup

The complete measurement setup for order tracking analysis is shown in Figure 5.13. The variac is used to adjust the speed of the system and it is connected to the AC motor. Accelerometers are positioned on the block housings and vibrations on various directions are collected. They are CCLD type accelerometers shown in

Figure 5.4. The collected revolution and acceleration data are transmitted to the analyzer and then to the computer. B&K PULSE platform is used during these measurements in order to display the results and manage the measurement.

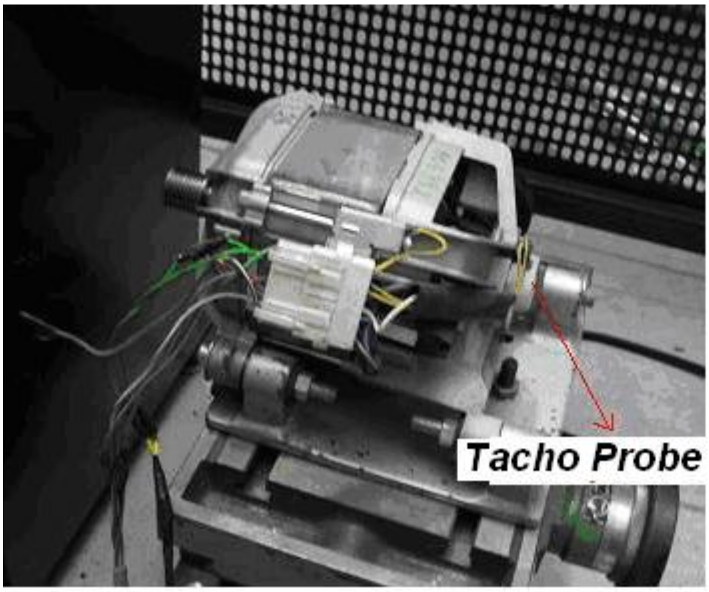

Figure 5.14 : The AC motor and tacho probe

The order tracking analysis can be done for both for run-up and coast-down situations. In this study, the analyses are performed for the run-up case. The vibration response of the system can be observed both with Order diagrams and Campbell diagrams. Also, the Pulse platform enables the adjustments of the order span, the rpm interval and the order resolution of the diagram. The analyzer has some limits about the resolution, order and frequency span. For instance, when more resolution in the rpm axis is desired, the order span or the rpm range should be reduced. During the experimental studies various span and resolutions are used for different cases.

In Figure 5.15, the Order and Campbell diagrams are presented. These results are obtained using the measurements in vertical direction. The order span of the measurement is chosen as 15 whereas the frequency span is 400 Hz. The measurement starts from 100 rpm and ends at 1360 rpm. Update rpm value is 20 rpm which means, the measurement of the response of the system will be refreshed at every 20 rpm.

The vibration amplitudes are not high, because no known unbalance excitations are applied during these measurements. However, the vibration characteristics of the system are clearly visible at every running speed. The regions marked in these diagrams show some important characteristics of the system. The Order 3.58 which corresponds to the ball passing frequency/running speed ratio is seen clearly in the order diagram. As discussed before, the paraboloid curves in order diagrams correspond to constant frequencies, whereas these frequencies are shown as straight lines in the Campbell diagram. The first natural frequency becomes visible especially when harmonics of rotational speed coincide with it. In the Campbell diagram, first bending natural frequency at around 31 Hz is seen. For the second bending natural frequencies, the frequency splitting phenomena as a function of the running speed is clearly visible. This is a result of gyroscopic effects. The 11th order indicates the running speed of the AC motor as the transmission ratio of the belt-pulley mechanism i=11.

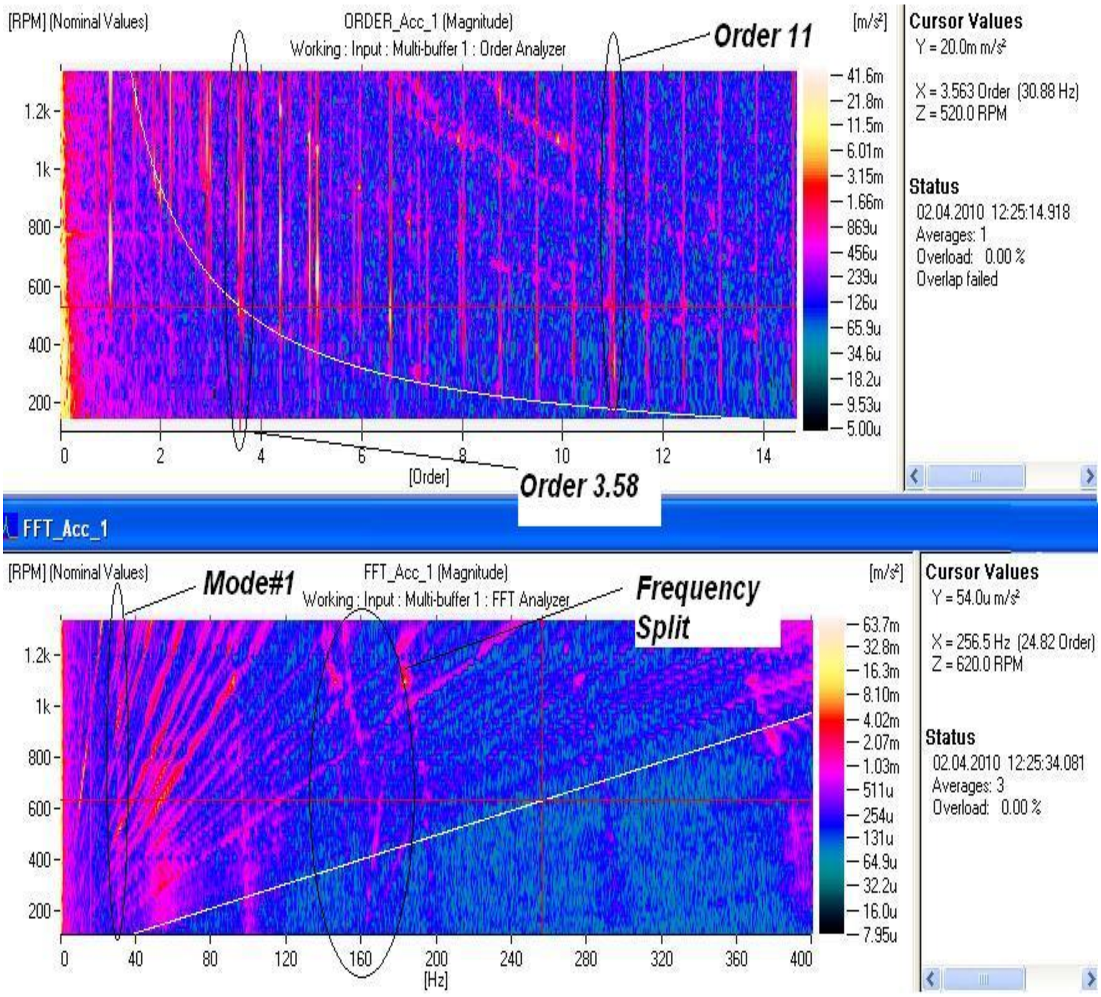

Figure 5.15 : Order and Campbell diagrams taken from Pulse interface

In order to observe the dynamic behaviour of the system at a specific speed range, the start and stop rpm values can be specified. The Order and the Campbell diagrams related to vibrations in horizontal direction are obtained when the system runs up from 900 rpm to 1300 rpm. Due to the reduced rpm span the resolution capacity is higher therefore update rpm value is chosen as 10 rpm, the results of this measurement is shown In Figure 5.16. Again, the frequency split behaviour is very distinct again for the natural frequencies corresponding to the second bending modes. However, the natural frequencies corresponding to first bending modes are not clear this time. At this running speed region, harmonics do not appear to coincide with the first bending natural frequency around 27-31 Hz. However, the running speed-dependent frequencies such as bearing defect frequencies are visible.

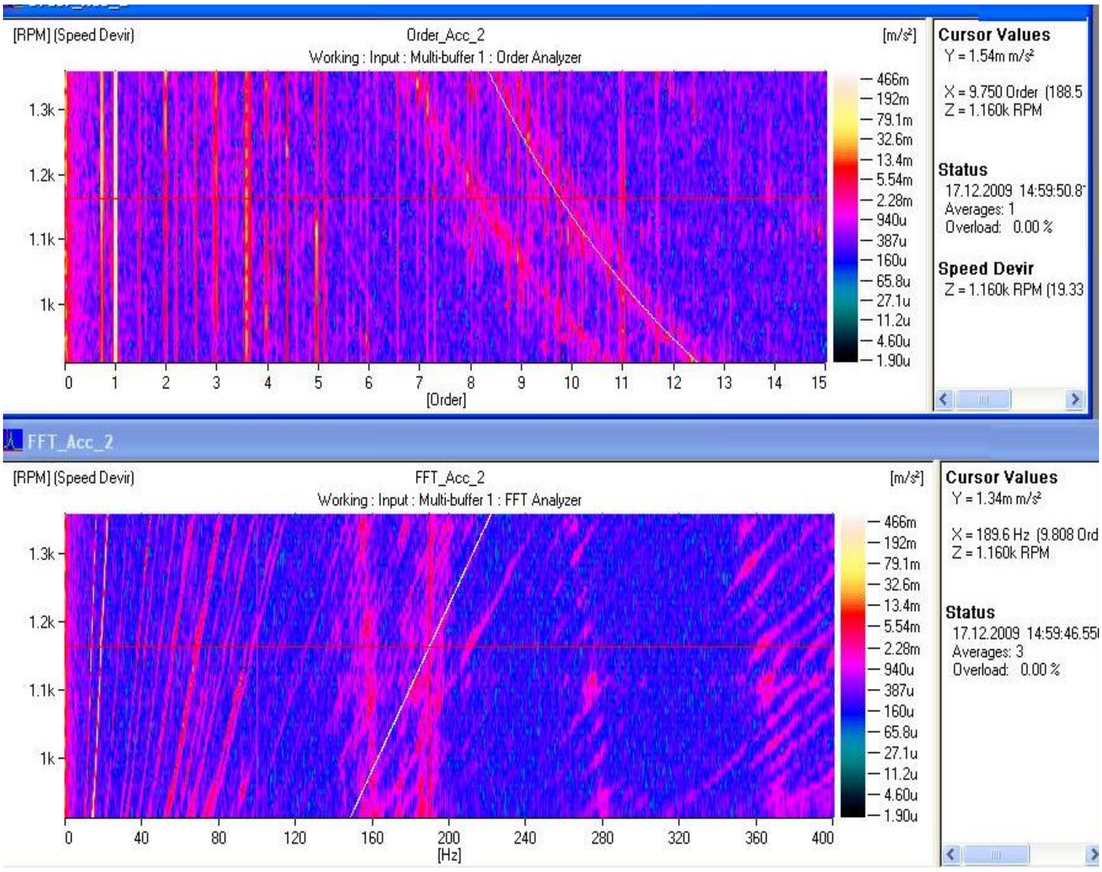

Figure 5.16 : Order and Campbell diagrams taken from Pulse interface

The measurements are also carried out under different excitations and when the system is changed from its reference condition. For example, the system is excited by adding known unbalance masses to the disc. The effect of the diametral clearance of the bearing on vibration behaviour is investigated. Furthermore, a defected bearing is included in these case studies. The results are presented in the next chapter and results are compared with the numerical predictions.

6. COMPARISONS OF NUMERICAL AND EXPERIMENTAL RESULTS

After the measurements taken from the test rig, at first the numerical model is improved in the light of these experimental data. Afterwards the results taken from the improved model are compared with experimental results.

6.1. Improvement of the rotor-ball bearing model

After the determination of the housing stiffness values using experimental results, the ADAMS model is updated in the light of this data. Housings are modelled using Frequency-Dependent (FD) damper elements in Msc. ADAMS software. These are frequency dependent elements which contain stiffness and damping properties. They are connected to the outer rings of the ball bearings. They are assumed to have stiffness and damping only in one direction. It should be noted that the outer rings do not have any rotational freedoms .Moreover outer rings are fixed in axial direction.

Also, during the measurements it is observed that the belt and pulley have a significant effect on the natural frequencies. Therefore, they are also included in the improved model of the rotor-bearing system. The pulley is assumed to be rigid and the mass and inertia properties are included in the model. The belt is modelled using a bushing element which has translational stiffness in vertical direction; also it has freedoms in other directions but they are very limited. The stiffness of the belt is determined after some numerical trials. However, the non-linearity of the belt is neglected in the model.

The unbalance masses can be inserted in the model at locations where there are holes on the disc. Two cylindrical parts are used in order to model the unbalance masses and their effects are validated using experimental results. The final model of the rotor-bearing system is shown in Figure 6.1.

The damping in the system is also adjusted using the experimental results. This required including the frequency dependent behaviour of the measured damping level in the model.

After the model improvements described above, numerical modal analysis is performed and the natural frequencies and mode shapes are determined using ADAMS/vibration solver.

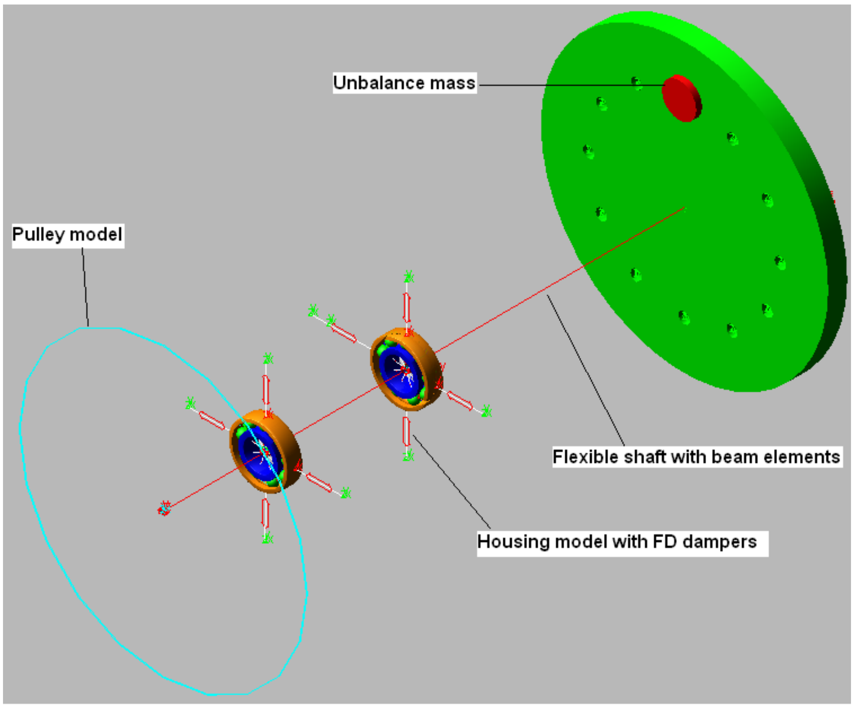

Figure 6.1: The latest rotor-ball bearing model

6.2. Comparisons of numerical and experimental results

6.2.1. Comparisons of the FRFs

The predicted FRFs using both primitive and improved numerical models are compared with experimental FRFs in vertical and horizontal directions in Figure 6.2 and Figure 6.3.

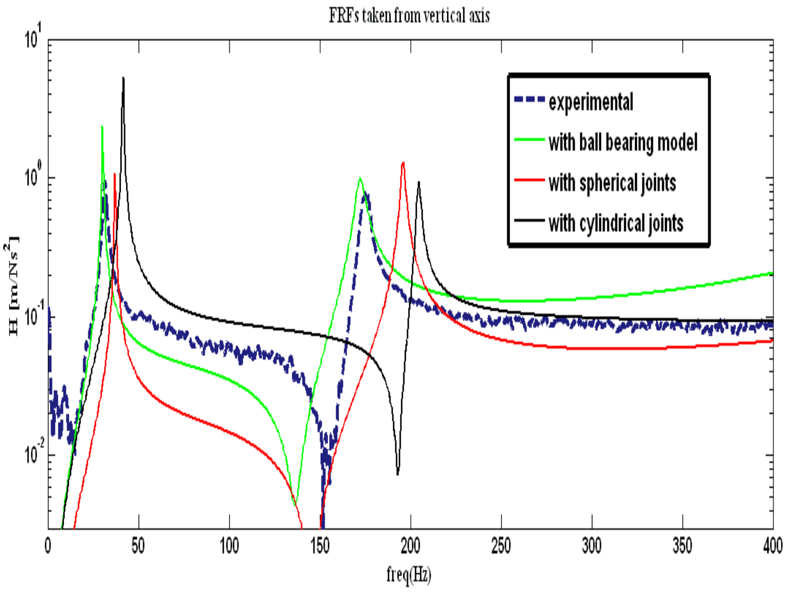

Figure 6.2 : Comparisons of predicted and measured FRFs in vertical direction

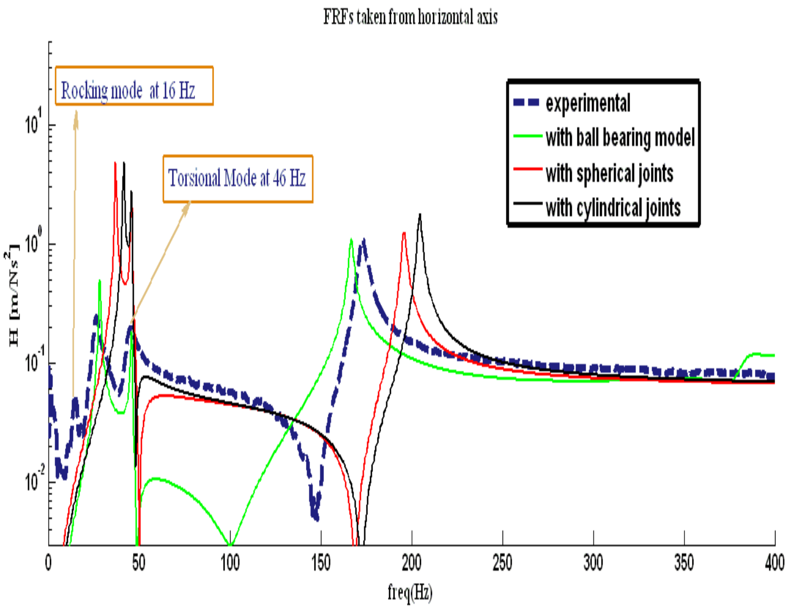

Figure 6.3 : Comparisons of predicted and measured FRFs in horizontal direction

The experimental FRFs in Figure 6.2 and Figure 6.3 show several peaks indicating natural frequencies. As discussed earlier, the one at 15 Hz is the natural frequency corresponding to the mode shape that can be described as the rocking of the whole system as a rigid body on elastic supports of the heavy bench and it is not included in the theoretical models. Another peak at 44.72 Hz in the measured FRFs corresponds to the torsional mode of the structure. The torsional mode appears here due to the impact hammer excitation having tangential component during the measurement. This causes torsional response of the system and appears as a peak in the measured

FRF. In order also to observe this torsional mode in the theoretical models, the system is excited in a way that enables significant angular vibration. The other peaks in the measured FRFs represent the first and the second bending modes of the system. It is noted that the measured and the predicted natural frequencies for the torsional and bending modes agree quite well for the case when the ball bearing model depicted in Figure 4.7 is used. The torsional mode is not affected by bearings hence the primitive models are capable of predicting the natural frequency of the torsional mode accurately. However, predicted natural frequencies for the bending modes are far from reality when the primitive bearing models are used.

6.2.2. Comparisons of the mode shapes

The first five mode shapes obtained from the improved model and test rig are represented in Figure 6.4, Figure 6.5, Figure 6.6, and Figure 6.7.The natural frequencies corresponding to those mode shapes are listed in Table 6.1 :

Table 6.1 : Comparisons of Natural Frequencies

Mode shape	Numerical (Hz)	Experimental (Hz)
First Bending	28.36	27.21
First Bending (vertical)	30.25	31.35
Torsional	45.82	44.72
Second Bending	167.73	169.27
Second Bending (vertical)	174.65	174.48

It can be seen from the results presented in Table 6.1 that differences in predicted and measured natural frequencies of the system is quite small. The natural frequencies within the frequency range of interest in this study (0-400 Hz) are predicted with acceptable accuracy. The corresponding mode shapes are shown in the figures below:

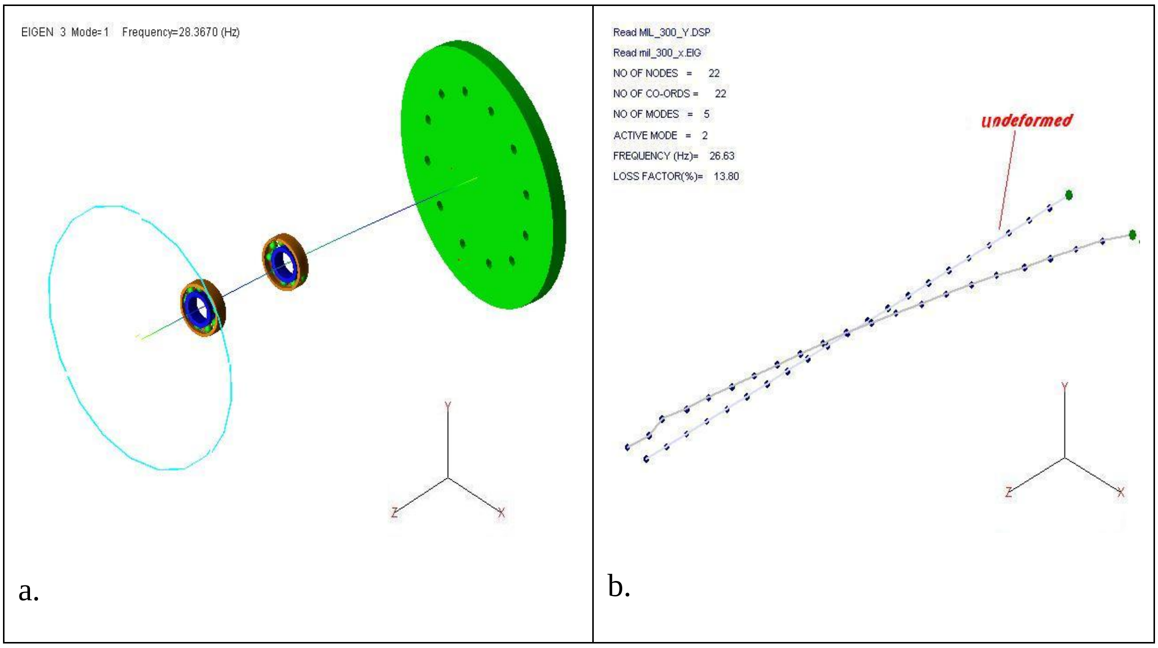

Figure 6.4 : The first bending mode in horizontal direction a) predicted b) measured

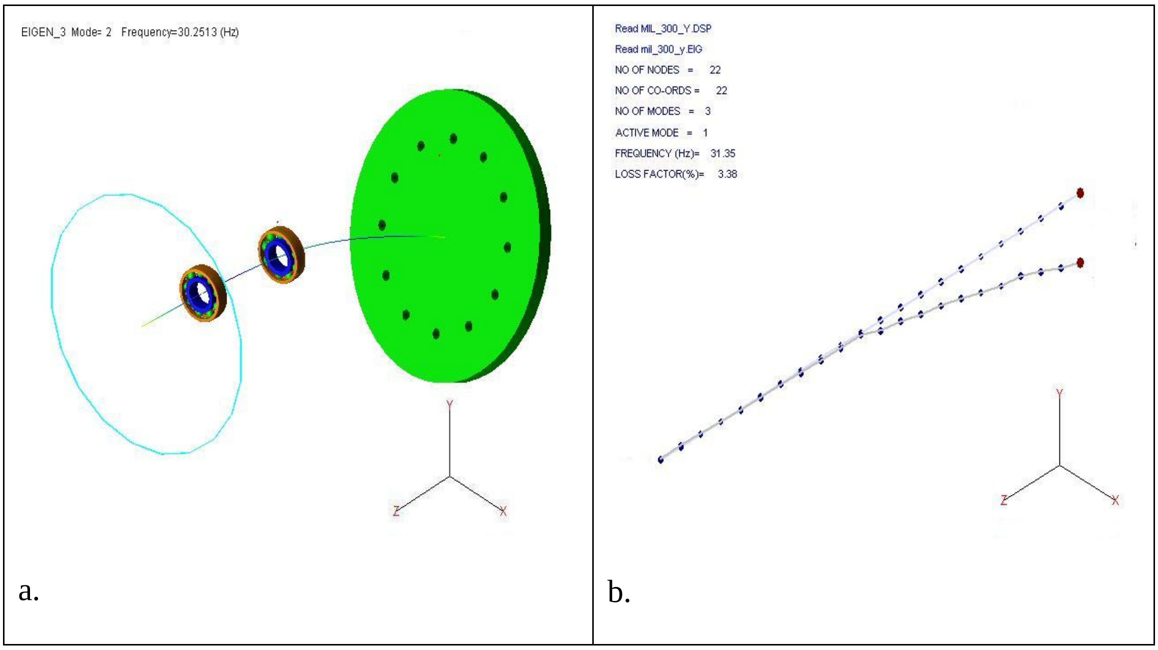

Figure 6.5 : The first bending mode in vertical direction a) predicted b) measured

As can be seen, the first two mode shapes are bending modes and there is a good correlation between the predicted (a) and measured (b) mode shapes. Figure 6.4 shows the bending mode shape in horizontal direction where Figure 6.5 shows the bending mode shape in vertical direction. The disc is not visible in the experimental model, but the node with large marker indicates the location of the disc.

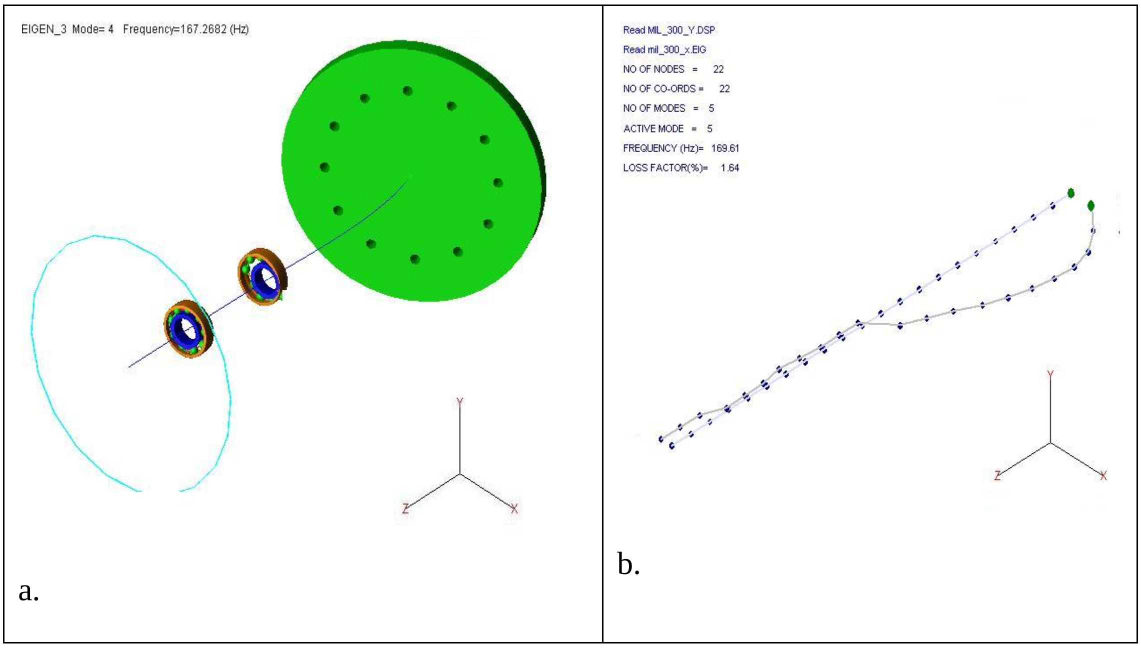

Figure 6.6: The second bending mode in horizontal direction a) predicted b) measured

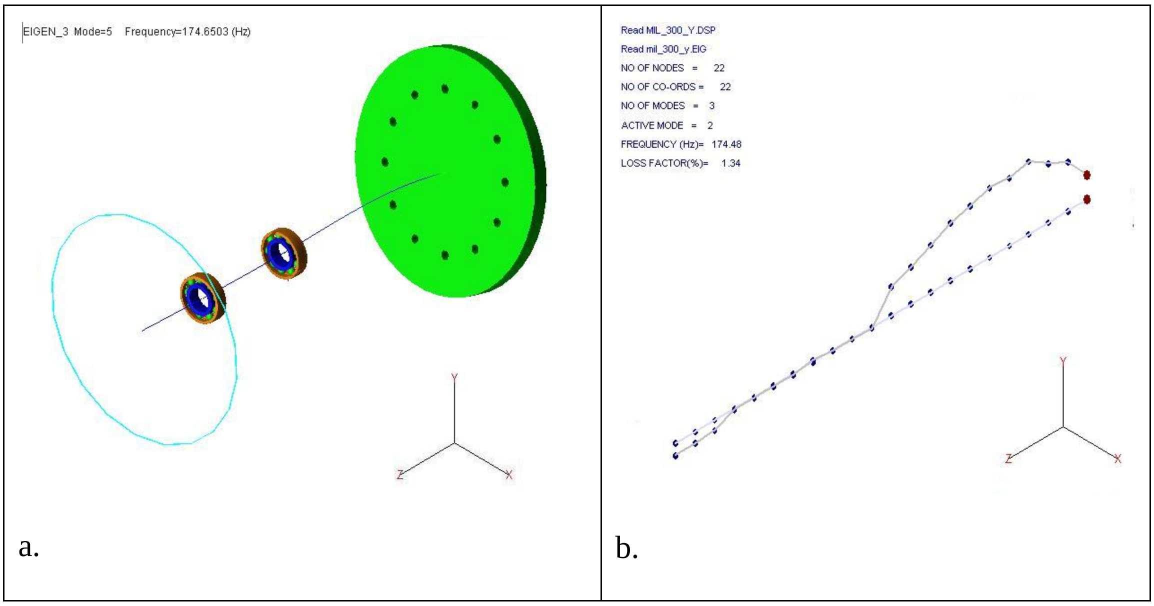

Figure 6.7 : The second bending mode in vertical direction a) predicted b) measured

The predicted second bending modes (Figure 6.6 and Figure 6.7) are also satisfactory when compared with experimental results. The torsional modes are also visible when the mode shapes are animated. However, they are not clearly visible when they are plotted as a snap shot; hence they are not shown here. The predicted torsional mode shape also fits with the measured one.

From these results, it can be stated that the predicted natural frequencies and mode shapes are in good agreement with the measurements. The model is validated for the static (non-rotating) case with acceptable accuracy. However, there are still some small differences between the predicted and measured behaviour. Possible reasons for these differences are:

- The disc and pulley are assumed to be rigid
- The stiffness of the belt is assumed to be linear and acts in one direction
- The oil film and its effects on damping are neglected.

6.2.3. Natural frequencies at different running speeds

As mentioned in Chapter 3, the natural frequencies of the system change as the rotational speed changes, mainly due to gyroscopic effects. In the proposed model these effects are also included and the natural frequencies at different running speeds are obtained. In order to demonstrate these gyroscopic effects and to determine the natural frequencies, a linearization [20] process is carried out and an eigensolution are performed at certain rotational speeds.

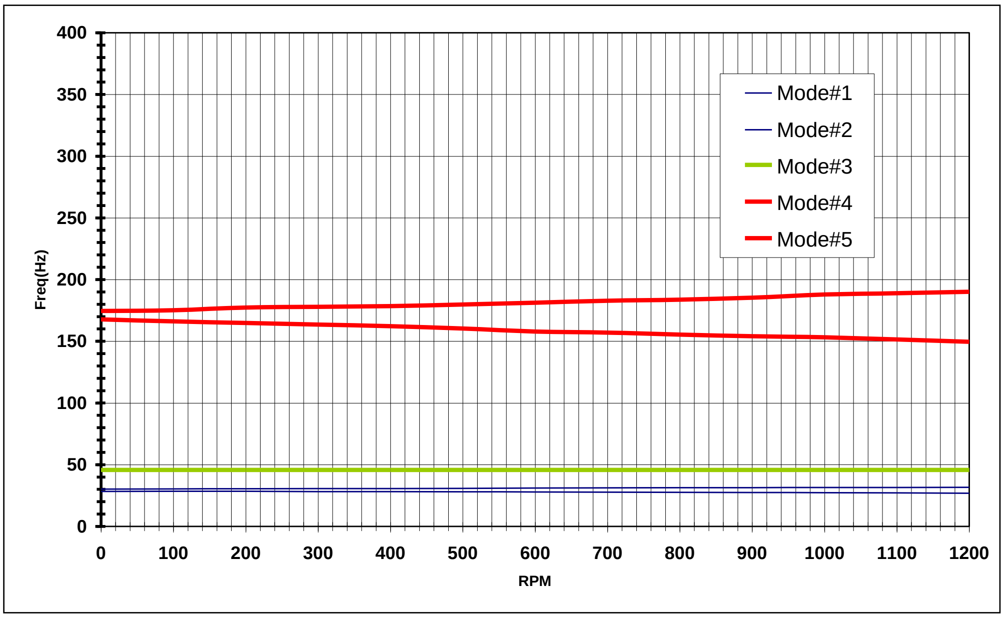

Figure 6.8 : Natural Frequencies of the system at different running speeds

As seen in Figure 6.8, the natural frequencies for the first bending modes do not show significant change when compared with the values at non-rotating conditions. However, although small, there are some changes and backward and forward traveling ways can be observed when the results are animated. The natural frequency corresponding to torsional mode does not show variation as the running speed increases. The most significant change is at natural frequencies corresponding to the second bending mode shapes.

Frequency split is also visible in measured results. The Campbell diagram obtained using measurement data is shown in Figure 6.9. The natural frequencies for the first bending modes are not clearly visible, but the torsional frequency is visible at around 46 Hz and it does not show any variation as a function of the rotational speed. However, as predicted, experimental results also show that there is a remarkable change in natural frequencies of the 2nd bending modes. , It can also be seen that vibration amplitudes are highest at frequencies close to the natural frequencies for the 2ndbending modes.   This is mainly due to the coincidence of the harmonics of running speed with the natural frequencies and bearing defect frequencies. After the modal results, the dynamic characteristics of the system at different running speeds are investigated. The bearing frequencies, harmonics of running speed and natural frequencies, and the critical regions are investigated under the dynamic results heading.

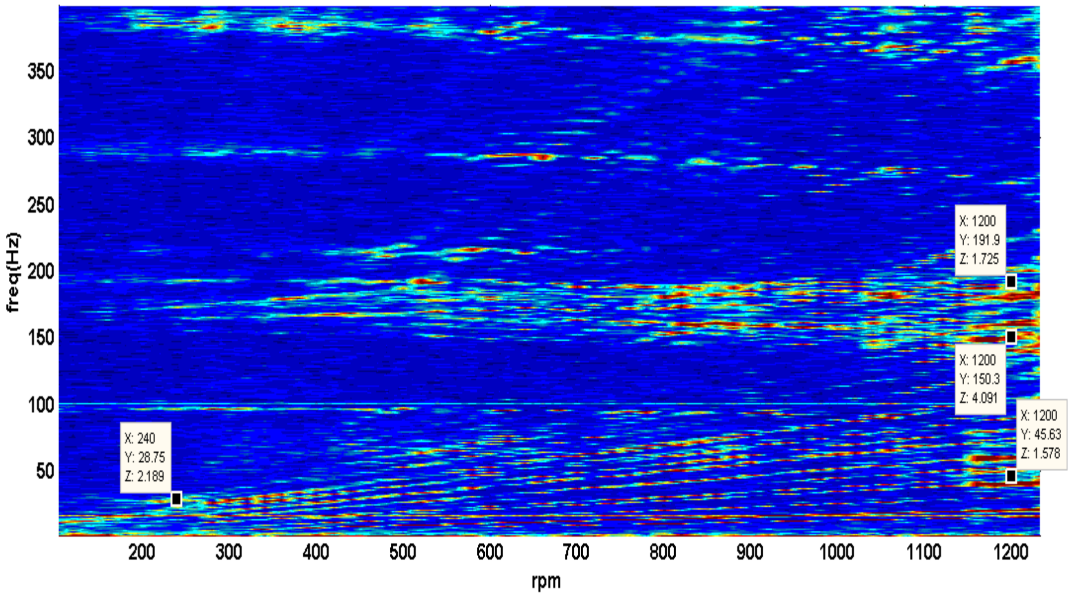

Figure 6.9 : Campbell diagram obtained from experimental model

6.3. Comparison of the dynamic results

For non-stationary, time-variant signals standard Fourier transform is deficient to analyze them. For such cases, Short Time Fourier Transform (STFT) technique can be used. In order to obtain Campbell diagrams based on numerical predictions, STFT technique is used. It is assumed in this technique that signal is stationary in short time intervals. The spectrogram of the signal is obtained in MATLAB using the vibration and time information taken from the simulations. The spectrogram of a signal (time-frequency plot) shows time information in horizontal axis. In ADAMS, the model is run-up to the desired speed slowly, and the vibration data are collected in terms of acceleration from the top of the housing, as in the measurements. The information about running speed is obtained from the time information, because the running speed is increasing proportional to time.

6.3.1. Case studies

6.3.1.1. Different unbalance conditions

The simulations and measurements are carried out for two different unbalance conditions. At first, a 30 gr unbalance mass is attached to the disc, then 66 gr unbalance mass is attached to the disc. For the case with 30 gr unbalance mass, the system is run-up to 1200 rpm whereas for the case with 66 gr unbalance mass the speed is increased up to 1000 rpm for safety issues.

The numerical rotor-bearing model is used to simulate this situation. STFT is applied to the time-domain acceleration data and Campbell diagrams are obtained numerically. The range of the color spectrum is the same in all the figures.

The Campbell diagram obtained using the experimental data corresponding to 30 gr unbalance is shown in Figure 6.10. The numerical counterpart for this condition is represented in Figure 6.11.

Also, the Campbell diagrams obtained from experimental results and numerical simulations of the system with 66 gr unbalance mass are presented in Figure 6.12 and Figure 6.13.

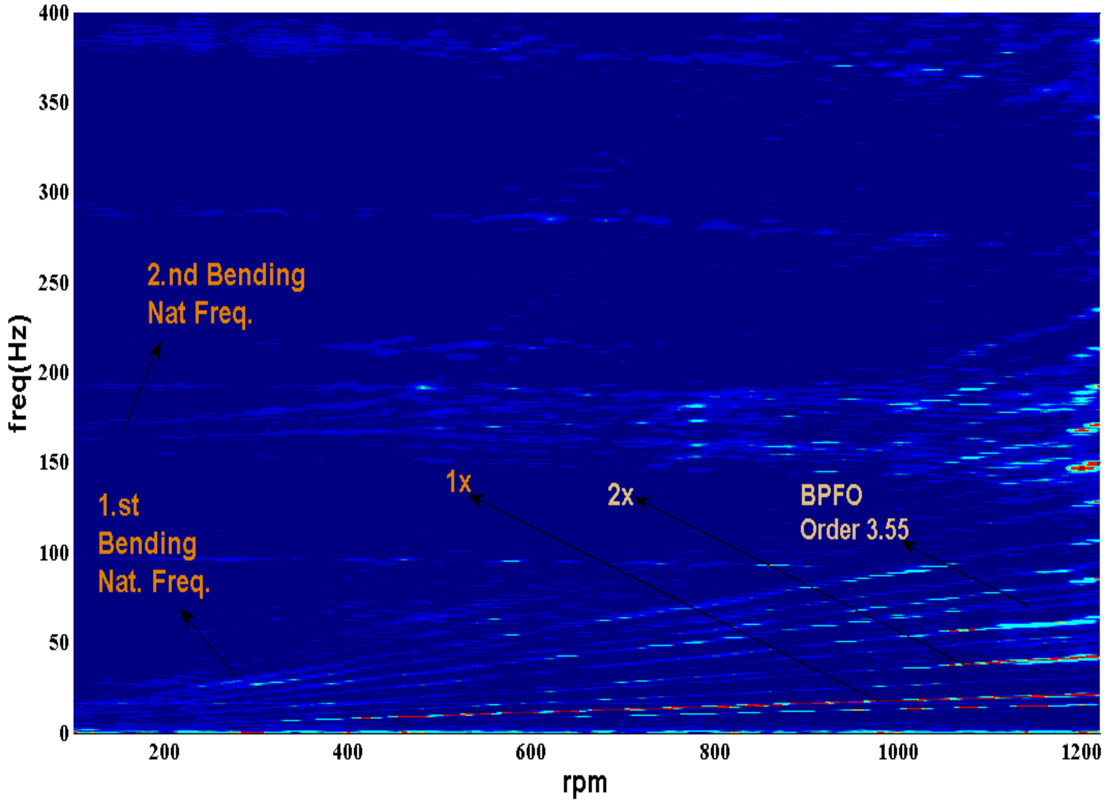

Figure 6.10 : The Campbell diagram of the test rig with 30 gr unbalance mass

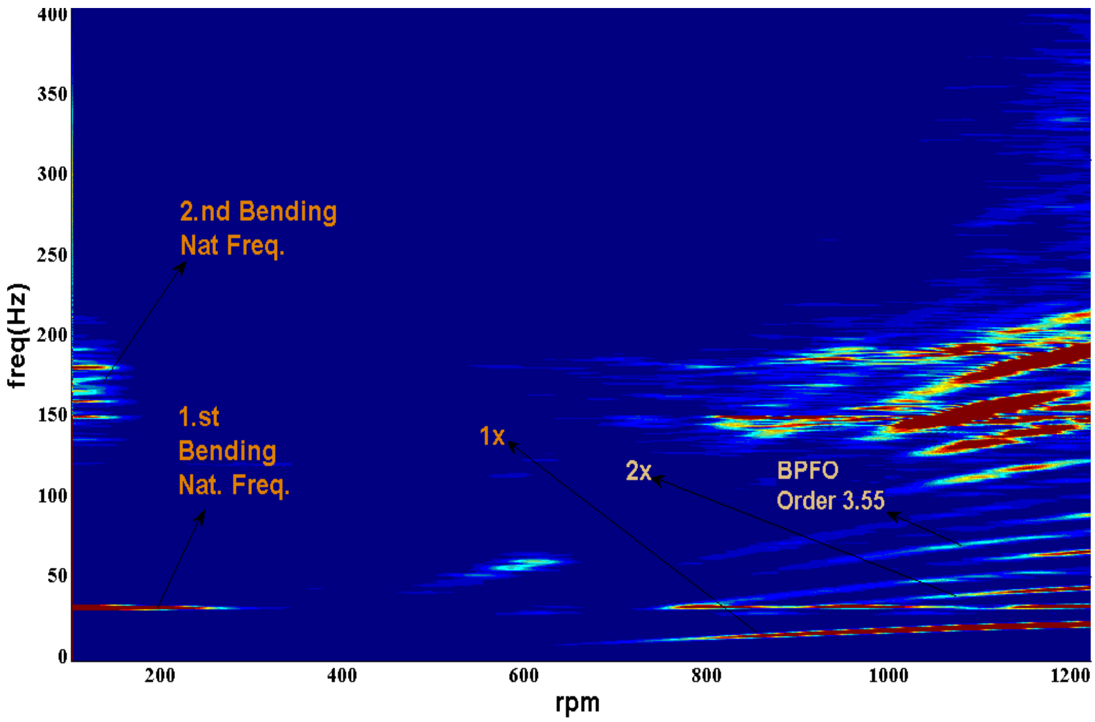

Figure 6.11 : The Campbell diagram of the ADAMS model with 30 gr unbalance mass

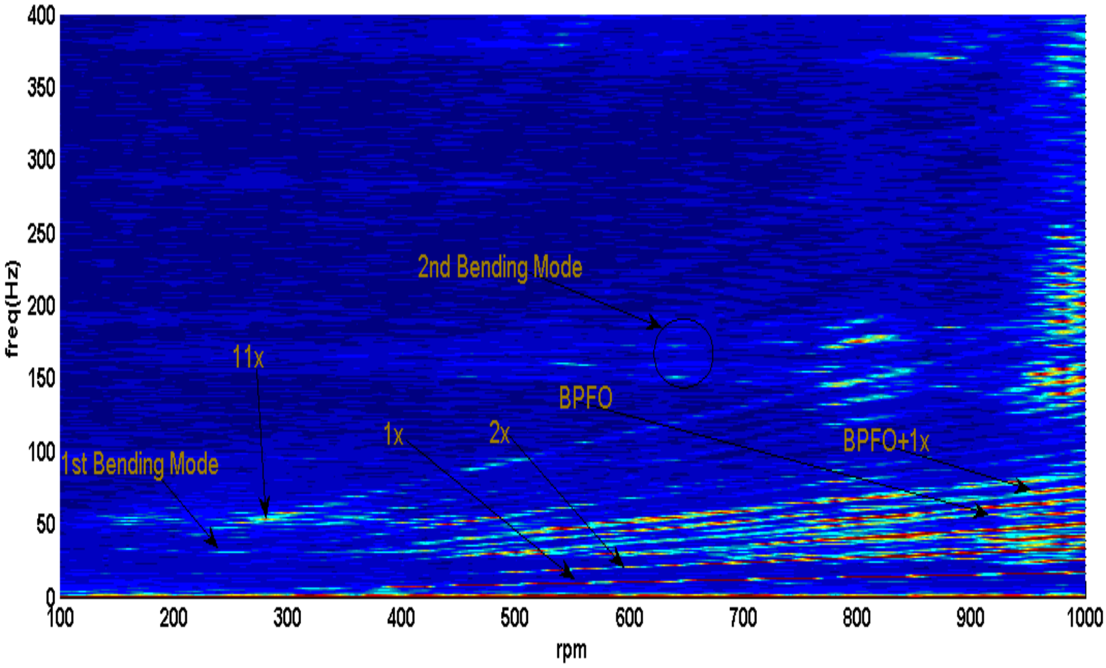

Figure 6.12 : The Campbell diagram of the test rig with 66 gr unbalance mass

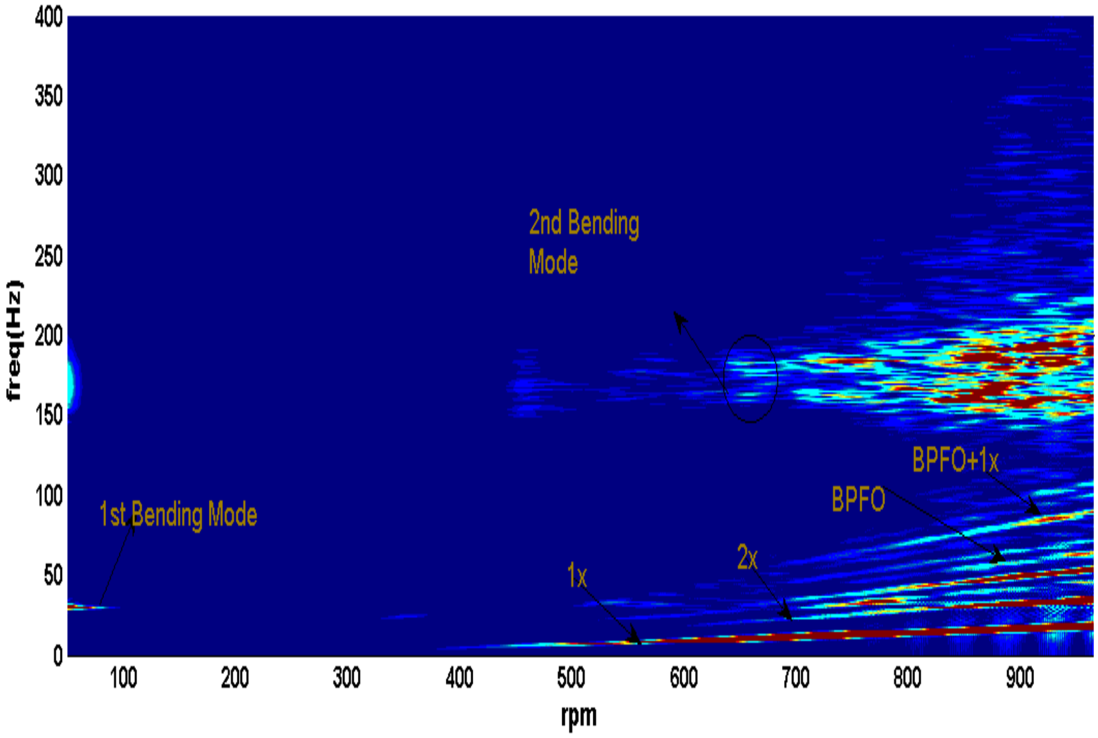

Figure 6.13 : The Campbell diagram of the ADAMS model with 30 gr unbalance mass

It is seen in both sets of results that because of the nature of imbalance, the 1st harmonic is very dominant. It should also be noted that for the ball bearing studied here, the ratio between the Ball Passing Frequency and shaft rotation speed is calculated as 3.55 in both experimental and numerical cases, the BPFO can be seen. However, they are not very significant as the bearings used can be considered defect free.

Also, the natural frequencies can be identified in both Figure 6.10 and Figure 6.11.It appears in the numerical result that the first bending modes are dominant at lower rotational speeds. In experimental Campbell diagram the 1st bending modes are less dominant, but they can be observed when some harmonics of the running speed or ball pass frequency coincide with the first bending natural frequencies. Also, as expected, when the higher harmonics (7th, 8th, 9th …) coincide with the second bending natural frequencies, higher levels of vibrations are obtained. The 11th order is also dominant and this is related to the vibrations of AC motor, due to transmission ratio being very close to 11.

For the dynamic case, a run-up procedure up to 1000 RPM is simulated numerically (Figure 6.12) and the same situation is created in reality using the test rig (Figure 6.13) A 66 g unbalance mass is attached to the disc in order to create the rotating unbalance force. In both Campbell diagrams, the 1st harmonic has very high amplitudes as a result of unbalance. Also, in both figures, Outer Ring Ball Passing Frequency (BPFO) with the sidebands are visible. It should be noted again that the experimental results indicate vibrations at the 11th harmonic of the running speed. This corresponds to the speed of electric motor which drives the test rig. This is also visible in the experimental results. The vibrations transmitted from the motor are not included in the numerical model; hence it is not visible in the predicted Champbell diagram.

The gyroscopic effects are quite significant for overhung rotors [19]. In both experimental and numerical Campbell diagrams with different unbalance conditions these gyroscopic effects are visible as frequency splits. While modelling the rotor-bearing system in Msc. ADAMS, the gyroscopic effect of the disc is included in the model [24]. It can be seen from both figures that the frequency split for 2nd bending modes is much more significant than that for the 1st bending modes.

There is a discrepancy between the numerical and experimental results when the regions with low vibration amplitudes are considered. There are noise and other sources, producing vibrations such as AC motor, clearance between the housing and ball bearing. They cause the system to produce response at some frequencies which can be considered as “background noise”. Obviously, the vibrations resulting from these are not seen in the predictions as these vibration sources are not included in the model.Also when Figure 6.10 and Figure 6.12 are compared, it can be seen that for running speeds below 1000 rpm, the system with 66 gr unbalance have higher amplitudes especially at 1^{st} and 2^{nd} harmonics. Moreover at the regions where harmonics of the running speed and natural frequencies coincide, the system with 66 gr unbalance has higher vibration amplitudes.

6.3.1.2. Analysis with a defected ball bearing

As discussed in chapter 1 the studies about rolling bearings are generally focused on defected cases. In order to simulate the effects of localized defects a small bump is created on the path of the proposed component in the numerical model. With this method simulations can be generated and give expected information about the location of the defect.

In the experimental model a bearing with a localized defect on the outer ring is used. It should be noted,however, that, it is not possible to create in the numercial model, an ideal/exact defect or bump on the surface of the outer ring as in the experimental (reality) case. Nevertheless, predictions are made and results are compared with the experimental results. The numerical and experimental frequency spectrums at 1180 RPM are shown in Figure 6.14.

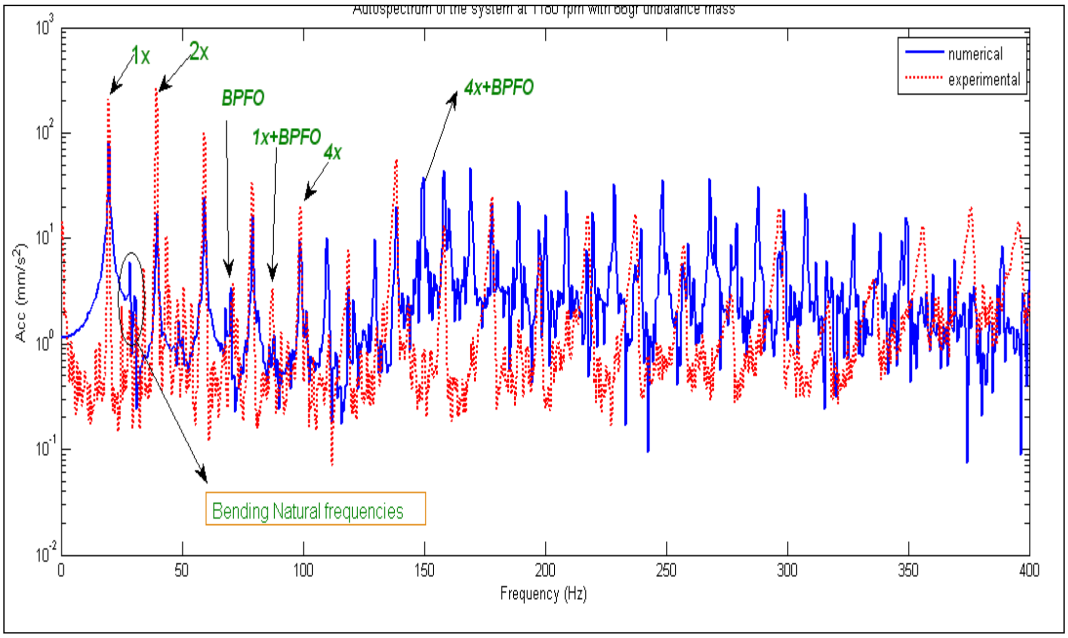

Figure 6.14 : Amplitude spectrum of the system with a defected ball bearing

It can be argued that the BPFO and its' side bands are visible in both cases in (Figure 6.14) Also, the predicted and the experimental vibration levels are quite close to each other. However, the level of correlation between the predicted and the measured spectrums decreases at higher frequencies.

7. CONCLUSIONS AND SUGGESTIONS FOR FUTURE WORK

7.1. Conclusions

In this study, a dynamic model of a rotor-ball bearing system is built using Msc. ADAMS software and vibrations occured in this kind of systems are analyzed. During this process different kind of models are built and investigated. A ball bearing model is developed first, then the rotor part consisting of a shaft and a disc at the end is created. Flexible parts are modeled using Finite Elements Method (FEM) via I-DEAS commercial software.

After the model is built, a test rig is designed in order to validate the numerical model. The numerical model is improved in the light of the experimental data and experimental and numerical modal analyses are performed. The numerical model is validated for the non-rotating case. Afterwards the simulations and measurements are carried out for the dynamic (rotating) case. STFT method is applied to the time-domain simulation results and Campbell diagrams are obtained from the numerical model. Order tracking analyses are also performed for the experimental case. Campbell and Order diagrams are obtained using the experimental measurements.

The most signficant results obtained from this study are listed below:

A dynamic model of a deep-groove ball bearing is built and the kinematic features of a ball bearing is satisfied in the model.

The deep-groove ball bearing model is assembled with the rotor part. Other parts(housings, belt, pulley) that effect the global vibrations of rotor-ball bearing system are also included in the model using inverse engineering approaches. The predicted modal results for the non-rotating case are correlating well with the experimental modal results especially for the frequency range up to 400Hz. First five mode shapes and natural frequencies are obtained and they are in good agreement with the experimental results.

It is shown that, the use of primitive joints instead of ball bearings and housings in the model does not yield satisfactory results.

For the rotating case, it is observed that some of the natural frequencies are dependent on rotational speed. Both predicted and measured results confirm this situation. However, when the dynamic model is run, vibrations levels at frequencies close to the second bending natural frequencies are overestimated, possibly due to smearing effect. Also, the damping of the system is changing with rotational speed, but the change of damping with rotational speed is not investigated in this study. This can be also a possible reason for this over predictions.

The effect of unbalance is also visible in both numerical and experimental investigations. The defected bearing case is not investigated in detail during this study, as it is hard to find a bearing with an "ideal defect" in reality. However, the method for modelling the defects in ADAMS environment resulted in acceptable approximations. The numerical model is capable of showing the bearing defect frequencies. Also the level of correlation between the predictions and the experimental decreased at higher frequencies

7.2. Suggestions for future work

The dynamic behaviour of rotor-ball bearings are modelled and analyzed during this study. However the model developed here is valid for 0-400 Hz frequency range. When the rotor is running at higher rotational speeds, the vibrations at higher frequrncies can also be dominant. Also, for the defected cases the ball bearings generate vibrations at natural frequencies of defected components. In order to observe these vibrations at high frequencies, the components of the ball bearing can be modelled as flexible. Although the computing times will definitly increase, that model can give satisfactory answers at high frequencies. Also, in order to reduce computing time model reduction techniques can be applied.

For further analyses, housings, belt and pulley can be included into model with better models. The non-linear beahviour of the belt can be modelled in a more accurate manner. Also the AC motor can be modelled as a vibration source, and its effect can also be seen in the results.

The test rig can be improved further. A special device that is used to assemble the ball-bearing to the shaft can be used in order to improve the repeatability of the measurements and the reliabilty of the test structure. Also ball bearings with known defects can be manufactured and vibrations due to geometrical informations can be investigated.

The ball bearing model developed here can be tested further using different rotating machines or diferent test rigs.

8. REFERENCES

[1] **Tandon, N., Choudhury, A.,** 1997. "An Analytical Model For the Prediction of the Vibration Response of Rolling Elements Due to Localized Defect", Journal of Sound and Vibration, Volume 205(3), pp. 275-292

[2] **Sassi, S., Badri, B., and Thomas, M.,**2007. "A Numerical Model to Predict Damaged Bearing Vibrations", Journal of Vibration and Control, Volume 13, pp. 1603-1630

[3] **Tandon, N., Choudhury, A.,** 1998. "A Theoretical Model To Predict Vibration Response of Rolling Elements Due to Distributed Defects Under Radial Load", Journal of Vibration and Acoustics, Volume 120, pp. 214-220

[4] **Tiwari, M., Gupta, K.,** 2000. "Effect of Radial Internal Clearance of a Ball Bearing On The Dynamics Of A Balanced Horizontal Rotor", Journal of Sound and Vibration, Volume 238(5), pp. 723-756

[5] **Tamura, H., Y. Tsuda,** 1985. "On The Static Running Accuracy of Ball Bearings", Bulletin of the JSME, Volume 28, pp.1240-1246

[6] **Tiwari, M., Gupta, K., Tiwari, K.Gupta,** 2000. "Dynamic Response of An Unbalanced Rotor Supported on Ball Bearings", Journal of Sound and Vibration, Volume 238(5), pp. 757-779

[7] **Aktürk, N., Uneeb, M., and Gohar, R.,** 1997. "The effects of number of balls and preload on vibrations associated with ball bearings", Journal of Tribology, Volume 1119, pp. 747-753

[8] **Wensing, J. A.,**1998. "On the Dynamics Of Ball Bearings", Phd Thesis, University of Twente, the Netherlands

[9] **Sopanen, J., Mikkola**, **A.,** 2003. "Dynamic Model of a Deep Groove Ball Bearing Including Localized and Distributed Defects, Part 1: Theory", Proceedings of the Institution of Mechanical Engineers, Journal of Multi-body Dynamics, Volume 217, 4, pp. 201-211

[10] **Sopanen, J., Mikkola**, **A.,** 2003. "Dynamic Model of a Deep Groove Ball Bearing Including Localized and Distributed Defects, Part 2: Implementation and Results", Proceedings of the Institution of Mechanical Engineers, Journal of Multi-body Dynamics, Volume 217, 4, pp. 201-211

[11] **Büyükördek, C., Ekşioğlu, M.C.,** 2007. **"**Elektrik Motoru Yapısal Tasarımı",Senior Design Project, Istanbul Technical University, Istanbul

[12] **Tandon, N., Choudhury, A.,** 1999. "A Review of Vibration and Acoustic Measurement Methods For the Detection of Defects in Rolling Element Bearings", Tribology International, Volume 32, pp. 469-480

[13] **Courrech**, **J.,** 2000. "Envelope Analysis For Effective Rolling Element Fault Detection- Fact or Fiction?" Brüel & Kjaer Technical Review, Uptime Magazine, Volume 8

[14] **Gade, S., Herlufsen, H., Hansen H.K.,** 1995., “Order Tracking Analysis” Brüel & Kjaer Technical Review, No 2.

[15] **Harris T. A.,** 1993. “*Rolling Bearing Analysis”,* Wiley & Sons, New York.

[16] **Hamrock B.J.,** 1994. *“Fundamentals of Fluid Film Interaction”,* Mc-Graw Hill,, New York.

[17]**Hamrock, B.J., Dawson, D.,** 1976. “Isothermal Elastohydrodynamic Lubrication of Point Contacts, Part 1: Theoretical Formulation”, Journal of Lubrication Tecnology., Volume 98, pp. 223-229..

[18] **Dietl, P., Wensing, J.,** and **van Nijen, G.C.,** 2000 . “Rolling Bearing Damping for Dynamic Analysis of Multi-Body Systems-Experimental and Theoretical Results.”, Proceedings of the Institution of Mechanical Engineers, Journal of Multi-body Dynamics, Volume 214, pp. 33-43.

[19] **Goodwin J. M.**, 1989. “*Dynamics of Rotor-Bearing Systems”*, Unwin Hyman Ltd., London, U.K.,.

[20] **Schwarz B. J., Richardson M. H.** 1999. “Experimental Modal Analysis”, CSI Reliability Week, Orlando, FL, US.

[21] **SKF Online Catalogue** http://www.skf.com/portal/skf/home/products?lang=en&maincatalogue, accesed at 21.04.2009

[22] **Tolerances and Fits, MitCalc software documentary.** http://www.mitcalc.com/doc/tolerances/help/en/tolerancestxt.htm accesed at 02.08.2009

[23] **Ewins, D. J.,** 2000. Modal testing: “Theory, practice and application”, Research Studies Press Ltd., England.

[24] **Ortiz J. L., Bir G. S.,** 2006 “Verification of New MSC.ADAMS Linearization Capability For Wind Turbine Applications” 44th AIAA Aerospace Sciences Meeting and Exhibit, Reno, Nevada, US

[25] **I-DEAS,** 2006. Version 11. Structural Dynamics Research Corporation.ISO 3740-45, 1977. Acoustics-Determination of Sound Power Levels of Noise Sources-Standarts Organization Publications. 1st ed.

[26] **MSC. ADAMS,** Version 2005r2. MSC Corporate Santa Ana, CA – USA.

[27] **ICATS,** Modent Suite, documentation

[28] **MATLAB,** Version 7.6.0.324 (R2008a).Fog, C.,